

The atmosphere in the laboratory: cavity ring-down measurements on scattering and absorption



Maarten Snee

**The atmosphere in the laboratory:
cavity ring-down measurements
on scattering and absorption**

VRIJE UNIVERSITEIT

**The atmosphere in the laboratory:
cavity ring-down measurements
on scattering and absorption**

ACADEMISCH PROEFSCHRIFT

ter verkrijging van de graad van doctor aan
de Vrije Universiteit Amsterdam,
op gezag van de rector magnificus
prof.dr. T. Sminia,
in het openbaar te verdedigen
ten overstaan van de promotiecommissie
van de faculteit der Exacte Wetenschappen
op dinsdag 23 november 2004 om 15.45 uur
in de aula van de universiteit,
De Boelelaan 1105

door

Maarten Christiaan Sneep

geboren te Amstelveen

promotor: prof.dr. W.M.G. Ubachs

*The mind is like a parachute,
it doesn't work if it isn't open.*

Frank Zappa



vrije Universiteit amsterdam



The work described in this thesis was financed by SRON, the space research organisation in the Netherlands under grant (EO-036) in the Earth Observation program, and was carried out at the Laser Centre of the Vrije Universiteit, De Boelelaan 1081, 1081 HV Amsterdam, where a limited number of copies of this thesis is available.

© 1999-2004, Maarten Sneep. Some rights reserved, see the last page for details.
ISBN 90-9018610-7

Contents

1	The earth's atmosphere and absorption spectroscopy	1
1.1	Destruction and recovery of the ozone layer	2
1.2	The natural- and the enhanced greenhouse effect	2
1.3	Satellite observations of the earth and climate change	4
1.4	The atmosphere in the laboratory	7
2	Experimental method: cavity ring-down techniques	9
2.1	The basic principle of the cavity ring-down technique	9
2.2	The ring-down cavity	11
2.3	Advantages and disadvantages of CRDS	14
2.4	Overview of the cavity ring-down setup	17
2.4.1	The ring-down cavity: pressure ramp, mirror-mounts and cooling	19
3	Experimental verification of Rayleigh extinction in various gases	21
3.1	Rayleigh scattering	22
3.2	Classical electrodynamic derivation of Rayleigh scattering	23
3.2.1	The magnitude of the induced dipole	23
3.2.2	The scattering cross section	24
3.3	Scattering distribution for natural light	25
3.4	Non-spherical molecules	26
3.5	Relation to other forms of scattering	28
3.6	The experimental method	31
3.7	Rayleigh scattering in argon, nitrogen and carbon dioxide between $17\,500\text{ cm}^{-1}$ and $21\,400\text{ cm}^{-1}$	33
3.7.1	Refractive indices and King correction factors for Ar, N ₂ and CO ₂	33
3.8	Scattering in CO ₂ , N ₂ , Ar, N ₂ O, CH ₄ , CO, SF ₆ and O ₂ at 532 nm	37
3.8.1	Refractive indices of the remaining gases	37
3.8.2	Oxygen at 532 nm	40
3.9	Conclusions	41
4	Collision-induced absorptions in oxygen	43
4.1	The peculiar properties of the oxygen molecule	44
4.2	Transitions with a double excitation	46
5	Cavity ring-down measurement of the O₂-O₂ collision-induced absorption resonance at 477 nm at sub-atmospheric pressures	49
5.1	Experiment and results	50
5.2	The model-equation for the absorption profile	52
5.3	Conclusion	55

Contents

6	Cavity ring-down measurement of the O₂-O₂ collision-induced absorption resonances at 477 nm and 577 nm at low temperatures and sub-atmospheric pressures	57
6.1	Description of the setup and the experimental procedure	58
6.1.1	Reaching and maintaining low temperatures	59
6.2	Measurements	60
6.3	Analysis of the data	64
6.4	Discussion and comparison with other measurements	66
6.5	Conclusions	69
7	Deep-ultraviolet cavity ring-down spectroscopy	71
8	Cavity ring-down spectroscopy of H₂¹⁸O in the range 16 570 cm⁻¹ to 17 120 cm⁻¹	77
8.1	Experimental details	77
8.2	Line Assignments	80
8.3	Discussion and Conclusion	84
	Bibliography	85
	List of publications	97
	Samenvatting	99
	Summary	103

The earth's atmosphere and absorption spectroscopy

Life on earth is made possible by a thin layer of gases that provides the oxygen to breathe, distributes and cleans the water we drink, keeps us warm and protects us from the harmful radiation of the sun. This layer is the atmosphere, which consists of nitrogen (78%), oxygen (21%), argon (0.9%) and other gases, usually referred to as trace gases.

Various layers can be identified in the atmosphere; an overview is shown in figure 1.1. The lowest layer is the troposphere, extending up to ~8 km at the poles and up to ~15 km in the tropics. The troposphere is highly turbulent and it is the region where the weather takes place. On average the temperature drops by about 6.5 °C/km throughout this layer. The drop in temperature stops abruptly at the tropopause, the boundary to the next layer: the stratosphere. This layer is dry, stable, high in O₃ content and the temperature rises with altitude. The highest concentration of O₃ is found between 18 km and 35 km. The top of the stratosphere is found at about 50 km altitude, where the temperature has reached almost 0 °C. Above this point, called the stratopause, the temperature once more starts to drop. This layer is known as the mesosphere. It continues until the mesopause, where the lowest temperature is reached in the atmosphere, about -86 °C, at an altitude of about 90 km. From then on the temperature rises with altitude, and more layers such as the ionosphere exist beyond this altitude.

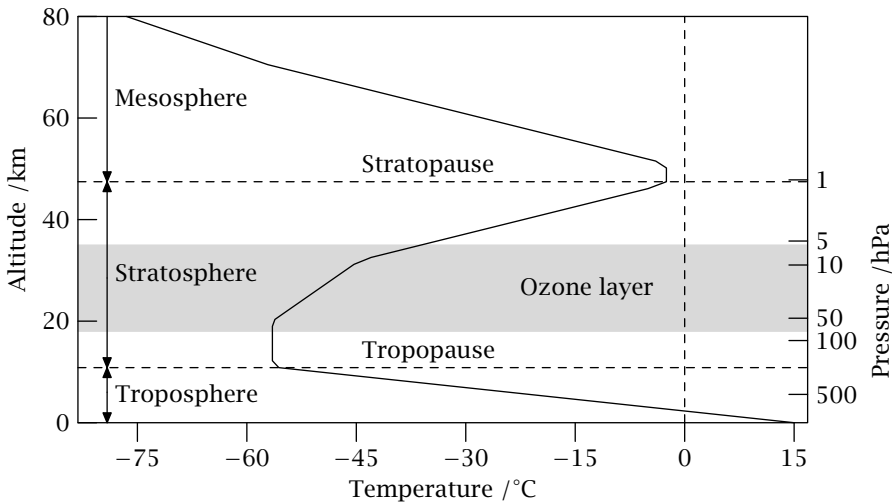


Figure 1.1 The layers in the atmosphere. The drawn line is the temperature profile against the altitude. See text for a full description.

1.1 Destruction and recovery of the ozone layer

The first widely recognised anthropogenic change in the atmosphere is the deterioration of the protective properties of the atmosphere. Pollutants - chlorine containing gases, mostly chlorofluorocarbons or CFC's - take part in a catalytic breakdown of O₃ in the ozone layer at around 20 km altitude. This hole in the ozone layer was so large, that satellite data pointing to its existence had been automatically discarded by the analysis software because of the supposed *impossibly low* values. It was only after Farman *et al.* [1] had published their alarming results from ground-based measurements, that the satellite data was re-examined, and that the depletion was seen in those measurements. Since then the thickness of the ozone layer has been monitored by satellite based instruments, and international political agreement was reached to ban the use of ozone destroying gases. Because of the slow breakdown of these chemicals it is expected that the recovery of the stratospheric ozone layer to the levels of 1980 will take about 100 years - the expected recovery is shown in figure 1.2. Continuous and global measurements on the ozone layer are needed to trace the recovery of the ozone layer and to police the international agreements. This global coverage can only be obtained with the use of satellites.

1.2 The natural- and the enhanced greenhouse effect

The 'trace gases' mentioned above are very important, as without those gases (water vapour, CO₂, CH₄, N₂O, O₃, ...) the average temperature on earth would be 33 °C lower. The main constituents of the atmosphere have hardly any interaction with the infrared radiation emitted from the earth's surface, the trace gases however have strong infrared absorption bands. They absorb infrared radiation emitted by the earth's surface and re-emit part of this radiation in all directions. The rest is converted into kinetic energy, raising the temperature of the atmosphere. At the altitude where the radiation is re-emitted, the temperature is lower than at the surface, -19 °C and 14 °C on average respectively, and therefore less energy is emitted into outer space [3].

Life on earth would be impossible without this greenhouse effect, but increased amounts of these greenhouse gases cause an *extra* rise in the temperature of the troposphere, leading to a disturbance of the balance that has evolved since the creation of the earth. Since the start of the industrial revolution, from about 1750 onward, human activity has changed the composition of the atmosphere. In figure 1.3 the concentration of CO₂ over the last 1000 years is shown. CO₂ is the most abundant of the anthropogenic greenhouse gases, and is released in the burning of fossil fuels for transportation and the production of electricity. The rise of the concentration of the anthropogenic greenhouse gases follows industrial activity closely and is already leading to changes in the climate [3]. Long-term

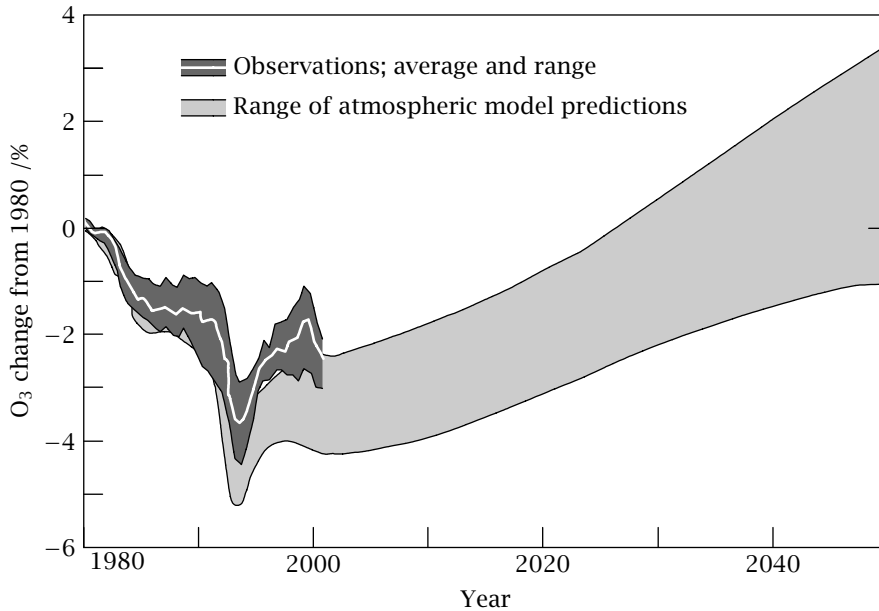


Figure 1.2 *Expected recovery of the stratospheric ozone layer. This data is the global average between 60° N and 60° S. The model studies show a significant recovery of the ozone layer by 2050, perhaps earlier. Note that this decrease and recovery is away from the poles, where the depletion is much more severe. The large fluctuation after 1991 is caused by the volcanic eruption of mount Pinatubo. Obviously such events are not taken into account in the predictions. Data taken from reference 2.*

reconstructions of the temperature and the concentration of CO₂ show a strong positive correlation between the temperature and the CO₂-concentration [5, 6].

Satellite observations of the Arctic have shown that over the last twenty years the temperature has risen by 0.33 °C decade⁻¹ over the sea ice to 1.06 °C decade⁻¹ over North America. Over this period, the melt season has lengthened by 10 to 17 days per decade. Comparison with older, ground-based measurements shows that the rate of warming over the last 20 years was about eight times higher than over the last century, suggesting a rapid acceleration in the warming [7].

The consequences and future direction of this trend are not entirely clear, as there are several feedback loops that may enhance or dampen the extra heating of the earth, especially the role of water vapour is unclear. One such effect that may give rise to a feedback loop was observed after the collapse of the World Trade Center in September 2001. For three days all civil aviation was grounded. During these three days the temperature difference between night and day increased [8]. This is not related to the greenhouse effect, but the extra warming during the night and lower temperatures during the day are believed to be caused by the artificial

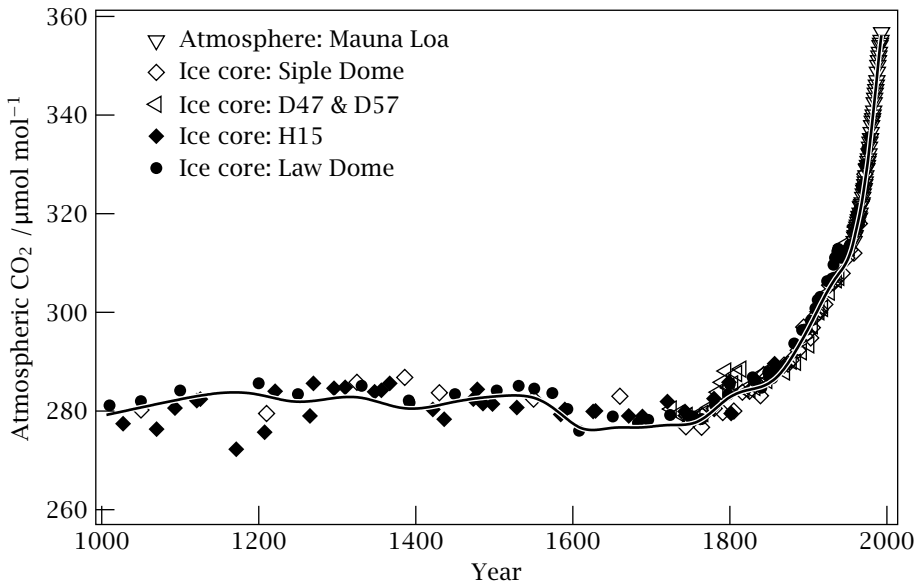


Figure 1.3 Change of the CO₂ content of the atmosphere since 1000 A.D. Older points were taken from bubbles of air trapped in firn or ice core samples. Figure adapted from Sarmiento and Gruber [4].

clouds formed by aircraft condensation trails. Because higher temperatures caused by the enhanced greenhouse effect may cause extra clouds to form, the magnitude of the temperature rise is unclear. The halting of civil aviation has also shown that human activity influences the temperature on earth, even on a short timescale.

1.3 Satellite observations of the earth and climate change

Measuring the composition and temperature of the atmosphere is crucial for understanding the interactions in the global climate system. Land-based measurement stations have their limits, especially with respect to their distribution around the globe. The recordings over roughly 150 years of the temperature, mostly performed by meteorological institutions in western Europe are very important for historical comparison and to determine trends, but they only cover a small portion of the earth, especially since 70% of the earth's surface is covered with water. Another limitation of meteorological stations is that they are ground-based, while the important processes take place between the ground and roughly 80 km. Although weather balloons are launched at regular intervals, their distribution around the globe is uneven and most of them are launched over land from the northern hemisphere.

At most of the meteorological sites spectral recordings of the solar spectrum are made. From these absorption spectra, the concentration of for instance O₃

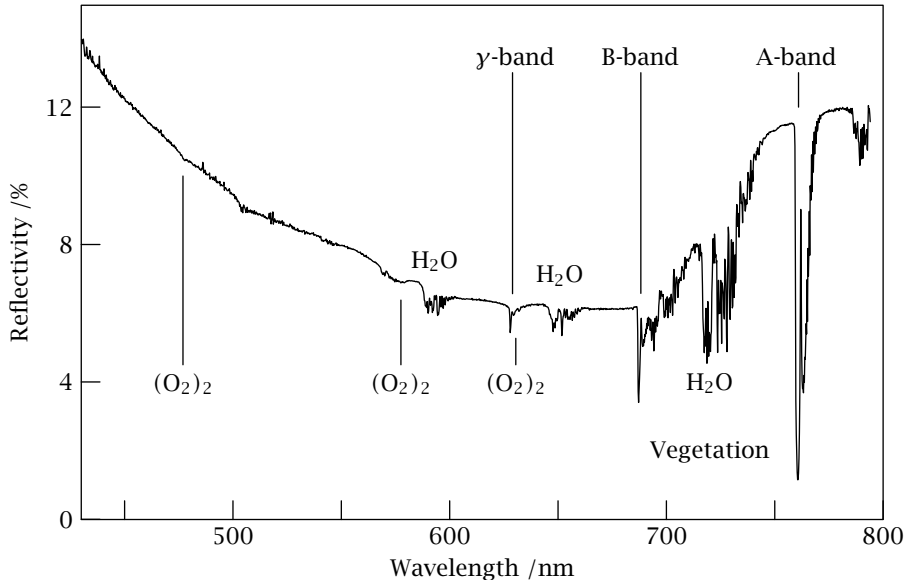


Figure 1.4 Clear sky measurement over the Californian coast by the GOME (Global Ozone Monitoring Experiment) instrument aboard the ERS-2 (second Environmental Research Satellite). The oxygen A-, B-, and γ -bands of the atmospheric oxygen system are clearly visible around 760 nm, 688 nm and 630 nm, respectively. The absorption features near 720 nm, 640 nm and 590 nm are caused by water vapour. Some broadband absorption features of O_2 collision complexes are seen at 630 nm - overlapping with the O_2 γ -band - 577 nm and 477 nm. The remaining features are mostly caused by H_2O absorptions and vegetation, while the background is caused by Rayleigh scattering and the ground surface reflectivity. Data supplied by Lang (private communication and reference 9).

above the site can be determined. These measurements can be extended to cover the globe by looking from the *other* direction, that is from space down to the earth. From spectral recordings of the sunlight reflected by the earth, or light that has otherwise travelled through the atmosphere, the concentration of trace gases can be determined. Part of a typical clear sky satellite measurement is shown in figure 1.4. Since all absorbers act at the same time, and the spectrum is modified by the wavelength dependent surface reflectivity, the analysis of the absorption spectra is a far from trivial operation. An overview of the available techniques and the issues involved can be found in reference 9.

The spectrum shown in figure 1.4 was taken by the GOME instrument, on board of the ERS-2 satellite, launched in 1995. GOME stands for 'Global Ozone Monitoring Experiment', and it features a spectrometer with a resolution of 0.2 nm to 0.4 nm over the spectral range of 240 nm to 790 nm. This spectral range allows

for the detection of ozone, water-vapour, oxygen, NO, NO₂, volcanic SO₂, H₂CO, BrO and OCIO. Note that some of these gases can only be detected under special circumstances, in particular during ozone hole conditions (OCIO) or after volcanic eruptions (SO₂). GOME was not the first instrument to observe the atmosphere from space, before it came several other instruments. GOME however was the first instrument to have a fairly high spectral resolution, about 10 times that of its predecessor, the TOMS series of instruments [10]. As an experiment, the GOME mission was very successful, and the lessons learnt from it were applied to its successors, SCIAMACHY and OMI.

The SCIAMACHY instrument on board the ENVISAT-1 satellite was launched in 2002. This satellite is packed with instruments to monitor the environment, among them a successor to GOME: SCIAMACHY (SCanning Imaging Absorption SpectroMeter for Atmospheric CHartography). The spectral range of the instrument has been increased to include essential parts of the near-infrared, in order to detect methane, carbon dioxide, carbon monoxide and nitrous oxide, in addition to the species detected by GOME. These are all important greenhouse (related) gases. In addition to looking straight down to the earth (nadir configuration), the SCIAMACHY instrument can also look ahead (limb configuration), thus enabling the measurement vertical profiles, in addition to column densities. This produces a three-dimensional dataset of the concentration of various gases.

The OMI instrument on board the EOS-Aura satellite was launched in July 2004. It is a successor to GOME, as far as the observation of ozone densities is concerned. The OMI (ozone monitoring instrument) uses the lessons from GOME to measure the ozone layer as accurately as possible. The spectral range is smaller than that of SCIAMACHY, 270 nm to 500 nm. Despite its name, it will detect some other gases as well: NO₂, SO₂ and BrO [11].

Although the spectral resolution has taken giant leaps since the first space based instruments, the spatial resolution is still relatively low - although it has improved from about 40 km × 320 km in GOME to 40 km × 40 km in OMI under normal conditions [11, 12]. One problem with this spatial resolution is that clouds may cover part of the pixel, altering the optical properties of the atmosphere and disturbing the further analysis. Clouds reduce the probability that photons reach the atmosphere below the clouds and are eventually scattered back to the space-based instrument. This reduces the average atmospheric path length of photons that are detected when clouds are present, and also reduces the probability of absorption by ozone or another molecule. To correct for the change in path length, the detected absorption strength of an absorber with a *known* concentration is used as a ruler to determine the effective path-length through the atmosphere. For GOME and SCIAMACHY the absorption in the oxygen A-band at 760 nm is used for this purpose. For OMI this absorption falls outside the spectral response of the instrument, and a different absorption needs to be found to determine the cloud coverage. Oxygen has no usable monomer absorptions below 500 nm, but around 477 nm a collision-induced absorption feature exists that can be used, although the pressure dependance of this collision-induced absorption complicates the analysis [13].

1.4 *The atmosphere in the laboratory*

In order to analyse the spectra measured by space based instruments, several data sets need to be combined. One of the most important pieces of information – apart from the satellite based measurements themselves – is knowledge of the absorption spectra of the species present in the atmosphere. The quality of these reference measurements is of direct influence on the retrieved concentrations in the atmosphere as both the line-positions and the absorption cross sections have to be known for quantitative analysis. In the laboratory the species can be studied separately, yielding absorption cross sections, that are needed in the analysis of satellite data.

The absorbers present in the atmosphere can cause some trouble when one wants to measure them in the laboratory; either the absorber is rare (BrO, SO₂, OClO, ...), and a strong resonance needs to be found and characterised. Conventional absorption techniques can be used in this case. On the other hand, the absorbing species may be present in high quantities (H₂O, O₂), and then weak lines need to be found, otherwise the atmosphere would be opaque for that wavelength. Sensitive detection techniques are needed for these measurements, and our laboratory uses cavity ring-down spectroscopy to measure these small absorption cross sections. Some of the more interesting species (O₃, OH, ...) may be very reactive, and therefore difficult to handle in an experimental setup.

The measurements presented in this thesis fall mostly in the second group: measurements on weak absorptions and light scattering phenomena in abundant species. In chapter 3 measurements on Rayleigh scattering are presented, an important, but weak background in absorption spectra. In satellite measurements however, the contribution of Rayleigh scattering is very important, as one of the prime mechanisms that allows sunlight to reach the instrument is back scattered radiation. In chapters 4, 5 and 6 measurements on the collision-induced absorption feature near 477 nm in oxygen are presented. The measurements in chapter 7 extend the cavity ring-down technique to wavelengths shorter than 200 nm, exploring the lower Schumann–Runge bands in oxygen and continuum absorptions in oxygen and carbon dioxide. Because of the very narrow-band laser used in these experiments – about 100 MHz FWHM at 200 nm – the collision enhanced absorption of the Herzberg continuum could be much better separated from the Schumann–Runge resonances than in previous experiments. These measurements are, to the best of our knowledge, the current the short-wavelength record for cavity ring-down spectroscopy, at wavelengths down to 197 nm. The final chapter shows measurements on H₂¹⁸O. Even though it is not the most abundant isotopomer of water, it still is an important absorber in the earth's atmosphere. Knowledge of the absorption spectrum of the stable isotopes will help to improve the theoretical understanding of the potential energy surface of the molecule, and enhance the accuracy of calculated spectra, not only for H₂¹⁸O, but also for the other isotopes.

The spectral resolution that is obtained in the laboratory is much higher than the resolution of space based instruments, typically by more than two orders of magnitude with the setup used in the experiments described here. One would think that for the analysis of the satellite measurements, low resolution measurements

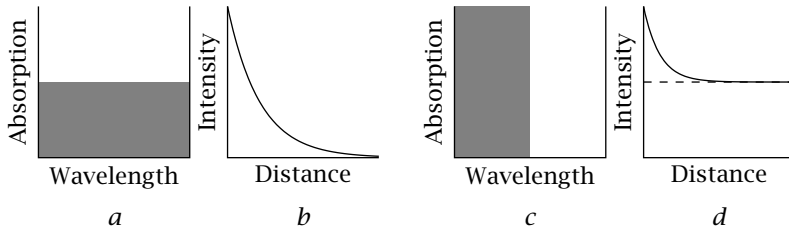


Figure 1.5 Radiative transfer modelling and sub-pixel spectral resolution. *a* — An average absorption results in an extinction shown in figure 1.5b. *b* — The intensity of the light with wavelengths falling within the pixel of figure 1.5a after travelling through the absorber over a certain distance. *c* — An absorption spectrum with the same average absorption, but here the spectrum has structure within the pixel. *d* — The intensity of the light with wavelengths falling within the pixel of figure 1.5c after travelling through the absorber over a certain distance. Note that the final value for the intensity is no longer zero.

would suffice. This is not the case, as the absorption spectra of some species, in particular of water vapour, are so dense that multiple lines fall onto a single pixel of the space-based spectrometer. In order to determine the concentration of water vapour, and other highly structured species, the absorption spectrum must be known at high resolution, as the loss of light when the absorption is modelled by the average over the pixel is very different from the more realistic structured spectrum, where some of the light may pass unhindered [14]. An average absorption, when combined with Lambert-Beer's law of extinction, will cause total absorption over a long distance. On the other hand, an absorption that covers half a pixel, but has twice the cross section over that range, so that the average over the pixel is the same, will absorb only half the intensity over a long distance. This is schematically depicted in figure 1.5.

It is the purpose of this study to determine in the laboratory, with advanced laser spectroscopic techniques, molecular parameters in terms of spectra and absorption strengths, of relevance for the so-called retrieval of column densities and height profiles of molecular species in the earth's atmosphere in various satellite missions, both in the present (GOME, SCIAMACHY, OMI) and in the future.

Experimental method: cavity ring-down techniques

Optical cavities have been used of spectroscopy in various forms, most commonly as an analysis method to determine the wavelength of the resonant light. Kastler [15] already suggests to use a Fabry–Perot etalon to enhance the absorption sensitivity, and the use of intra-cavity laser absorption spectroscopy dates back to the early days of the tunable laser [16]. The idea to use the rate of decay of a high finesse cavity for optical measurements was initially applied to the measurement of mirror reflectivities [17]. O’Keefe and Deacon [18] made the connection between the decay rate of a cavity and the extinction of light due to absorption by a molecule, and therewith invented cavity ring-down spectroscopy (CRDS). The setup they used employed a pulsed, tunable laser, and is now known as a “generic pulsed CRDS setup”. Since the publication of the article by O’Keefe and Deacon [18], the method of cavity ring-down spectroscopy has been applied to different absorptions ranging from ~ 200 nm to $10 \mu\text{m}$ and many variants of excitation and detection schemes have been used. Various methods and applications of cavity ring-down spectroscopy are described in a number of reviews [19–21].

2.1 The basic principle of the cavity ring-down technique

The principle of cavity ring-down spectroscopy is based upon a measurement of the rate of decay of an optical resonator with a high quality factor, indicating a long lifetime of the photons in the cavity [22]. The principle is schematically illustrated in figure 2.1. A laser pulse of short duration, typically ~ 5 ns, is coupled into a stable but non-confocal cavity, consisting of two highly reflecting ($\mathcal{R} > 99.9\%$) curved mirrors. At each mirror a small part ($1 - \mathcal{R}$) of the circulating power will be coupled out, while the remaining part is reflected back in the cavity. The first pulse leaking out of the cavity will have an intensity $I_0 = (1 - \mathcal{R})^2 I_{\text{in}}$. The k^{th} pulse with intensity

$$\begin{aligned} I_k &= I_0 \mathcal{R}^{2(k-1)} \\ &= I_0 \exp(2(k-1) \ln \mathcal{R}) \end{aligned} \tag{2.1}$$

will leak out $2d(k-1)n/c$ seconds after the laser pulse, where c is the speed of light, n the index of refraction and d is the length of the cavity. Since we are dealing with gas-phase environments at low pressure, the index of refraction is neglected. The explanation starts with a cavity without absorber, as illustrated in figure 2.1a.

A 5 ns pulse has a length of 1.5 m. Practical ring-down cavities have a round-trip length $2d$ or less than that, and therefore pulses will overlap inside the cavity.

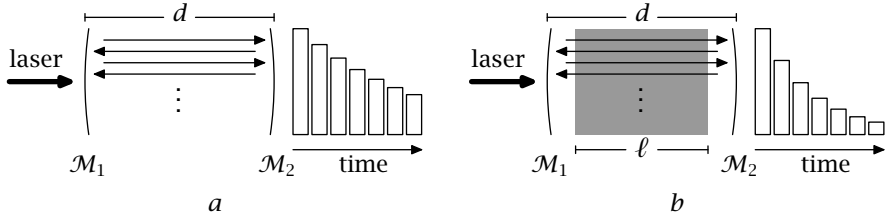


Figure 2.1 The principle of cavity ring-down absorption measurements. *a* — Light decaying in an empty cavity, the decay rate is determined by the reflectivity of the mirrors. *b* — The cell is filled with an absorber, the decay rate is now determined by the mirrors and the absorption in the gas.

Furthermore the detection system usually has a response time that causes the discrete pulses to blend into a continuous signal as a function of time t ,

$$I_t = I_0 \exp\left(-\frac{c}{d} |\ln \mathcal{R}| t\right). \quad (2.2)$$

The decay rate of an empty cavity $\beta_{\bar{\nu}}^0$, or the decay time $\tau_{\bar{\nu}}^0 = 1/\beta_{\bar{\nu}}^0$, is the background signal of a cavity ring-down experiment. $\beta_{\bar{\nu}}^0$ is determined by the length of the cavity and the mirror reflectivity, which depends on the frequency $\bar{\nu}$ of the light

$$\beta_{\bar{\nu}}^0 = \frac{c}{d} |\ln \mathcal{R}_{\bar{\nu}}|. \quad (2.3)$$

Additional losses, usually caused by absorption of light and by Rayleigh scattering on molecules in the cavity, result in a faster decay. Since *any* gas will cause extinction through Rayleigh scattering, we call the total extinction $\kappa_{\bar{\nu}}$, the loss through absorption $\alpha_{\bar{\nu}}$ and the loss through scattering $\alpha_{\bar{\nu}}^{\text{scatt}}$. We have $\kappa_{\bar{\nu}} = \alpha_{\bar{\nu}} + \alpha_{\bar{\nu}}^{\text{scatt}}$. $\kappa_{\bar{\nu}}$ is normally written as an extinction over distance z , but this can easily be rewritten as an extinction over time, again neglecting the refractive index

$$\begin{aligned} I_z &= I_0 \exp(-\kappa_{\bar{\nu}} z) = I_0 \exp(-N \sigma_{\bar{\nu}}^{\text{tot}} z) \\ &\equiv I_0 \exp(-\kappa_{\bar{\nu}} c t) = I_0 \exp(-N \sigma_{\bar{\nu}}^{\text{tot}} c t). \end{aligned} \quad (2.4)$$

When the additional losses satisfy Beer's law, the decay remains exponential over time and the two contributions can be combined, yielding:

$$I_t = I_0 \exp\left(-\frac{c}{d} (|\ln \mathcal{R}_{\bar{\nu}}| + N \sigma_{\bar{\nu}} \ell) t\right), \quad (2.5)$$

where ℓ is the length within the cavity that is filled with the absorbing species, see figure 2.1*b*, and $\kappa_{\bar{\nu}}$ the frequency dependent extinction coefficient.

The rate at which the ring-down signal decays with ($\beta_{\bar{\nu}}$) or without ($\beta_{\bar{\nu}}^0$) the presence of additional absorbers, is given by:

$$\beta_{\bar{\nu}} = \frac{c}{d} (|\ln \mathcal{R}_{\bar{\nu}}| + N \sigma_{\bar{\nu}} \ell); \quad \beta_{\bar{\nu}}^0 = \frac{c}{d} |\ln \mathcal{R}_{\bar{\nu}}|. \quad (2.6)$$

From $\beta_{\bar{\nu}}$ and $\beta_{\bar{\nu}}^0$, we find an expression for the extinction induced by the medium, where we assume that the absorber fills the complete cavity, so $\ell = d$, yielding a simple equation for the extinction in terms of cavity decay rates:

$$N\sigma_{\bar{\nu}} = \frac{\beta_{\bar{\nu}} - \beta_{\bar{\nu}}^0}{c}. \quad (2.7)$$

A few remarks are in order before we continue. No two mirrors are exactly equal, if only because of the cleaning procedure. What we have called $\mathcal{R}_{\bar{\nu}}$ in the preceding text, is in fact the geometric mean of the reflectivities of the two mirrors \mathcal{M}_1 and \mathcal{M}_2 : $\mathcal{R}_{\bar{\nu}} = \sqrt{\mathcal{R}_1 \mathcal{R}_2}$. Furthermore, the reflectivity depends on the frequency. This was implied above, but a small explanation is useful. Dielectric mirrors used for cavity ring-down reach their reflectivity with a multi layer interference filter. This means that the reflectivity must be frequency dependent. Experience shows that mirrors can be used up to 10% from their peak wavelength, and that the reflectivity varies slowly in that range. One usually measures a spectrum and determines the $\beta_{\bar{\nu}}^0$ from the decay rate between the resonances. This has the advantage that the broadband Rayleigh scattering is automatically subtracted, and with the density N in the cell one finds the cross section for absorption $\sigma_{\bar{\nu}}^{\text{abs}}$.

2.2 The ring-down cavity

There is one aspect of optical cavities that was deliberately ignored in the previous discussion on the principle of cavity ring-down spectroscopy. In general, optical cavities have a transmission spectrum that is not flat, there are resonances. A typical ring-down cavity is a stable, linear, resonator, with two identical mirrors. To form a stable cavity - meaning that the light remains close to the centre of the cavity when it enters along its axis, the geometry of the cavity must fulfil the stability criterion [23]:

$$0 < \left(1 - \frac{d}{R_c}\right)^2 < 1. \quad (2.8)$$

with d the length of the cavity and R_c the radius of curvature of the mirrors. From equation (2.8) it follows that stable cavities must have a length $0 < d < 2R_c$. This stability criterion follows from consideration of geometric optics. Light is a wave phenomenon, and solution of the wave equation inside the cavity leads to stable solutions at specific wavelengths. For a cavity in the confocal configuration - $d = R_c$ - the resonance frequencies are [22]:

$$\nu_r = \frac{c}{2d} \left[q + \frac{1}{2}(m + n + 1) \right], \quad (2.9)$$

where q is longitudinal mode number - the number of half-wavelengths that fit in the length of the cavity, and m, n are the transverse mode numbers. In the confocal configuration, the transmission spectrum of cavity is degenerate: the mode with $q = q_1$ and $m + n = 2p$ has the same frequency as the mode with $m = n = 0$ and $q = q_1 + p$. The spacing of the resonance frequencies for a confocal cavity is

$\Delta\nu = c/4d$. If one moves away from the confocal configuration, the degeneracy is removed. The resonance frequencies for non-confocal configuration turn out to be [22]:

$$\nu_r = \frac{c}{2d} \left[q + (m + n + 1) \left(\frac{1}{2} + \frac{2}{\pi} \arctan \frac{d - R_c}{d + R_c} \right) \right]. \quad (2.10)$$

With the lifting of the degeneracy, resonances of higher order transverse modes appear at more frequencies between the fundamental modes. The effect this has on a cavity ring-down experiment was demonstrated by Meijer *et al.* [24]. Under normal circumstances the transmission of a cavity is wavelength dependent, however, with a pulsed laser that has a FWHM at the Fourier limit of 100 MHz – and in practise is much broader, at about 1.5 GHz – multiple resonances of the cavity are excited, independent of the position of the laser. As far as cavity ring-down is concerned, the cavity may be considered to consist of two independent mirrors, and mode-structure can be neglected, up to a certain extent.

A valid question remains how many transverse modes are needed to create a ‘white’ transmission spectrum. Taking into consideration the finite size of the cavity mirrors, and the increase of the spot size with increasing transverse mode number, there must be an upper limit to the transverse mode number that can be supported in the cavity, without increasing the loss rate dramatically. Kogelnik and Li [23] present some calculations of diffraction losses for the first two transverse modes TEM₀₀ and TEM₀₁, but no estimate is given for higher orders. An estimate can be made by considering a cavity with very large mirrors, calculate the mode-patterns on the mirrors and calculate the fraction outside a certain radius for the single pass loss-rate. From equation (2.10) the mode-spacing can be determined, and if all modes up to and including TEM₈₈ are included, sufficient ‘whiteness’ is expected, that is the resonances have a spacing of about 10 MHz – making the transmission spectrum completely flat for pulsed light with a bandwidth of ~1 GHz. These numbers are calculated for a cavity as used in the experiments described here, with $d \approx 0.8R_c$ and $R_c = 1$ m.

Using the equations given by Kogelnik and Li [23], the energy distribution on the mirrors can be calculated. From their article the energy distribution on the mirrors is obtained in two different symmetries:

$$U_{\text{rect}}(x, y) = H_m \left(\sqrt{2} \frac{x}{w} \right) H_n \left(\sqrt{2} \frac{y}{w} \right) \times \\ \times \frac{w_0}{w} \exp \left\{ -i(kz - \Phi_{\text{rect}}) - (x^2 + y^2) \left[\frac{1}{w^2} + \frac{ik}{2R} \right] \right\} \quad (2.11)$$

$$U_{\text{cyl}}(r, \varphi) = \left(\sqrt{2} \frac{r}{w} \right)^l L_p^l \left(2 \frac{r^2}{w^2} \right) \times \\ \times \frac{w_0}{w} \exp \left\{ -i(kz - \Phi_{\text{cyl}}) - r^2 \left[\frac{1}{w^2} + \frac{ik}{2R} + il\varphi \right] \right\} \quad (2.12)$$

where R is the local radius of curvature of the light-field, w the spot-size or beam radius, w_0 the beam waist, Φ a phase shift and d the length of the cavity as before. Some special functions are used: the Hermite polynomials H_n and the generalised Laguerre polynomials L_p^l [25]. On the mirrors the radius of curvature of the light-

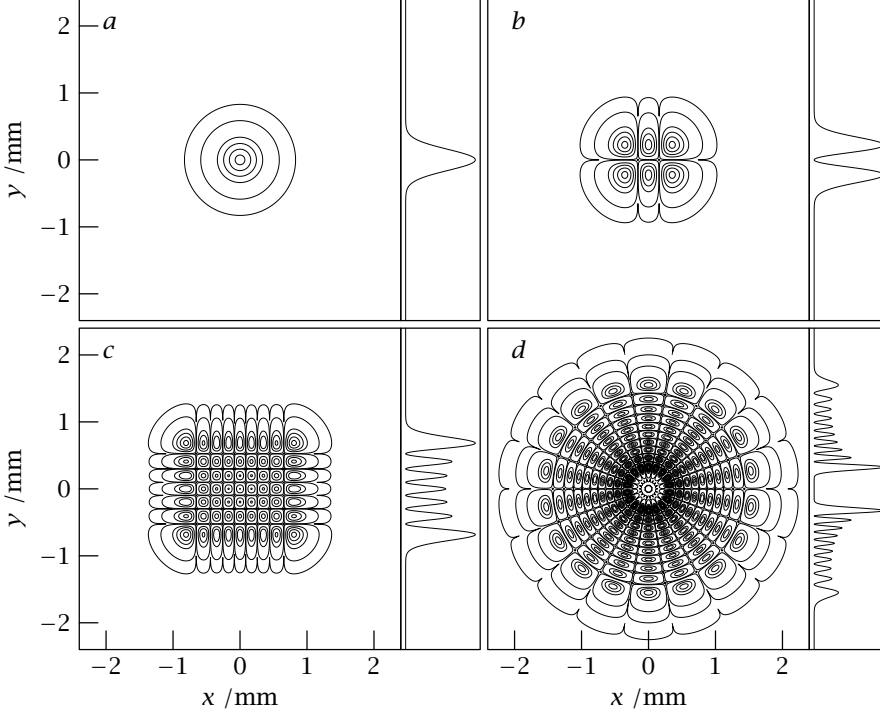


Figure 2.2 Calculated contour plots of the mode patterns as they appear on the mirrors. All patterns calculated for an 88 cm cavity with mirrors that have a radius of curvature of 1 m and 630 nm light. The small additional graphs are cross sections of the intensity distribution through $x = 0$. *a* — TEM_{00} mode *b* — TEM_{21} mode *c* — TEM_{86} mode *d* — TEM_{99} mode in cylindrical symmetry.

field must match that of the mirrors: $R(d/2) = R_c$. The geometry used in the calculations has its origin at the centre of the cavity, the z coordinate along the axis of the cavity and x and y - or r and φ - perpendicular to the z -axis. The functions used in equations (2.11) and (2.12) are:

$$w_0^2 = \lambda \frac{\sqrt{d(2R-d)}}{2\pi}; \quad w^2(z) = w_0^2 \left[1 + \left(\frac{\lambda z}{\pi w_0^2} \right)^2 \right]; \quad R(z) = z \left[1 + \left(\frac{\pi w_0^2}{\lambda z} \right)^2 \right];$$

$$\Phi_{\text{rect}} = (m + n + 1) \arctan \left(\frac{\lambda z}{\pi w_0^2} \right); \quad \Phi_{\text{cyl}} = (2p + l + 1) \arctan \left(\frac{\lambda z}{\pi w_0^2} \right).$$

The intensity on the mirrors is given by $I(x, y) = U(x, y) U^*(x, y)$. In figure 2.2 some calculated contour plots of the energy distribution of selected higher order modes are shown. From these figures, it would seem that even high order modes fall within the radius of the small mirrors. The fraction of the energy that falls

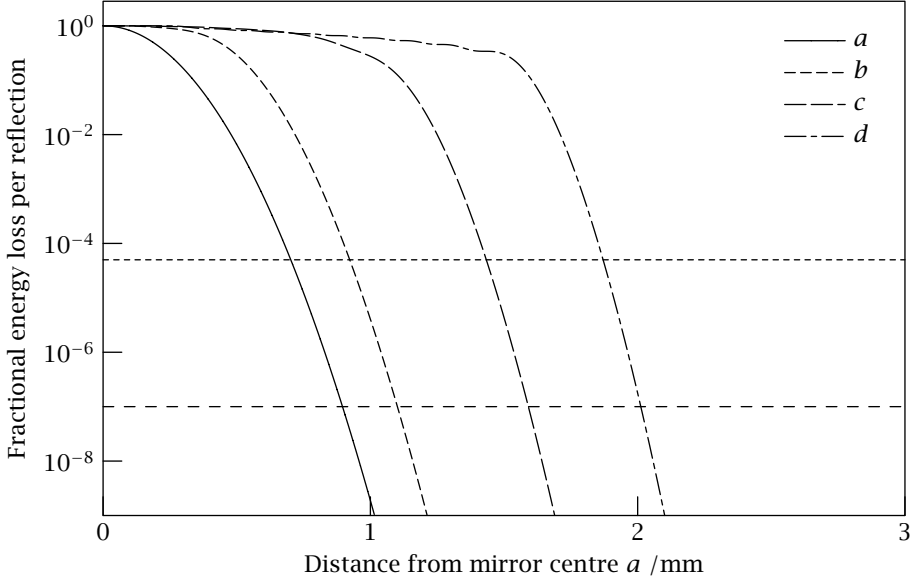


Figure 2.3 Radial energy distribution of EM radiation on the mirrors. The horizontal line at 5×10^{-5} represents the loss on good quality mirrors, large enough to limit diffraction losses to a minimum. The horizontal line at 10^{-7} represents the detection limit of our system. The same modes were shown in figure 2.2.

outside a radius r is given by:

$$E_r = 1 - \frac{\int_0^r r' \int_0^{2\pi} I(r', \varphi') d\varphi' dr'}{\int_0^\infty r' \int_0^{2\pi} I(r', \varphi') d\varphi' dr'} = \frac{\int_r^\infty r' \int_0^{2\pi} I(r', \varphi') d\varphi' dr'}{\int_0^\infty r' \int_0^{2\pi} I(r', \varphi') d\varphi' dr'}. \quad (2.13)$$

For the same modes shown in the contour-plots of figure 2.2, this energy within the radius r was also calculated. The resulting traces are shown in figure 2.3, including the losses on a good quality mirror-set and the weakest absorption ever seen in our laboratory [26].

2.3 Advantages and disadvantages of CRDS

An important advantage of cavity ring-down spectroscopy is the fact that the intensity of the light does *not* appear in equation (2.7); all information is contained in the time-evolution of the ring-down signal. The high sensitivity of cavity ring-down spectroscopy is associated with this independence of the fluctuations of the light source. Another advantage is the fact that mirrors can now be made at such high reflectivity, up to $\mathcal{R} = 99.999\%$, that very long effective path lengths can be created, up to 100 km with a cavity length of only 80 cm. This leads to a very high sensitivity, absorptions as weak as $2 \times 10^{-9} \text{ cm}^{-1}$ can be detected in this generic

cavity ring-down setup [26]. This very high sensitivity can be reached in very small cell volumes, making this technique particularly suitable for measurements on isotope enriched samples, as is demonstrated in e.g. [26–28] and chapter 8.

A crucial issue is that the rate of decay of the cavity should be exponential. Only under that assumption the exponential decay associated with Beer’s law for absorption can be added to the decay of the empty cavity – see equation (2.5) – thus resulting in mono-exponential decay in a cavity filled with gas. If for some reason the resulting decay function is non-exponential no value of $\beta_{\bar{\nu}}$ can be derived in the fitting procedure. Note that it is mathematically prohibited to design a fitting procedure to an arbitrary sum of exponentials. Multi-exponential decay can be caused by several mechanisms, the most common being laser-bandwidth induced effects. If the bandwidth of the exciting laser is non-negligible with respect to the width (Doppler or collisional) of the spectral line, then the various frequency components within the bandwidth profile are subject to different rates of absorption, as shown in figure 2.4; hence these frequency components produce a sum of exponentials, which results in a non-exponential decay of the monitored signal:

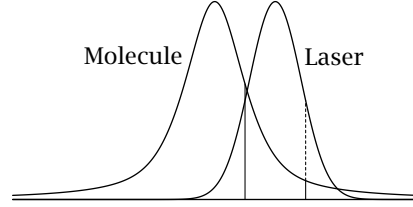


Figure 2.4 Multi-exponential decay.

$$I_t = \int_{\bar{\nu}} I_{\bar{\nu}} \exp(-\beta_{\bar{\nu}} t) d\bar{\nu} \quad (2.14)$$

This effect is in fact the well-known “slit-function” problem of all spectroscopy, but its treatment, in the case of CRDS, is more complicated than usual because of its non-linear nature. Although the problem has been noted in literature [29–32], it still hampers the use of CRDS for the determination of absolute cross sections of narrow line features. If both the laser profile and the absorption profile have a Gaussian shape, it can be shown that the *integrated* intensity $\int_{\bar{\nu}} \sigma_{\bar{\nu}} d\bar{\nu}$ is unaffected by this bandwidth effect. Note that the peak absorption is still underestimated, and it can also be shown that this result is extremely sensitive to the laser line-shape; this invariance is not of much practical use.

Another relevant issue for the analysis of ring-down transients is the proper treatment of the decay transients in fitting routines. As was elaborated by Naus *et al.* [33] a weighted non-linear least-squares fit to the data on the transient give the best determination of the decay life time, and in particular produces a reliable estimate of the uncertainty. The model function in this procedure includes an offset, as the zero level cannot be found accurately enough from the zero-light part of the decay transient; the offset found in the fit is usually smaller than the white noise on this part of the transient:

$$I_t = I_0 \exp(-\beta_{\bar{\nu}} t) + I_{\text{offset}} \quad (2.15)$$

As for the optical resonator it is important that it is aligned such that its mode structure does not result in wavelength-dependent effects. There is two methods

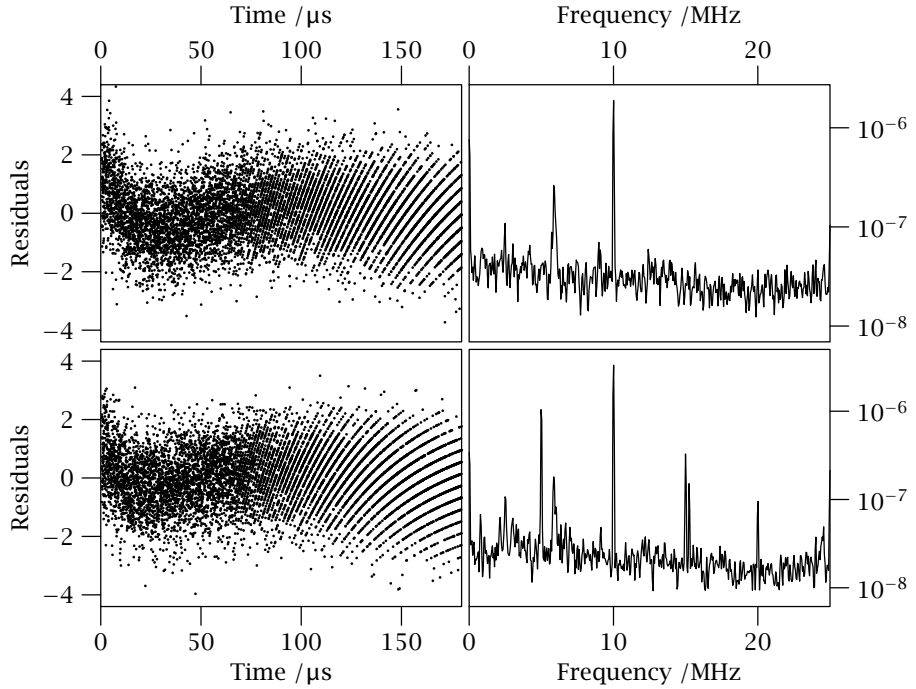


Figure 2.5 The residuals of two ring-down measurements are shown. Each measurement is the average of four laser shots. On the left the residuals are shown, on the right the Fourier transform, to detect fast oscillations.

for achieving this. In one method, developed by Van Zee *et al.* [31], the cavity is aligned in confocal position to transmit a single mode adapted to the laser frequency. Although the method yields accurate results it is not well-suited to be used in absorption measurements, where fairly large wavelength ranges are to be scanned. In the alternative method the cavity is aligned far from confocal ($d \approx 0.85r_c$, d the distance between the mirrors and r_c the radius of curvature), such that a large number of longitudinal and transversal cavity modes is supported, making the cavity a white light transmitter. It is noted that in this condition only a very small fraction ($[1 - \mathcal{R}]^2$) of the initial laser pulse reaches the detector. The optical resonator then acts as a white-light filter and the configuration can be used for wavelength-scanning pulsed CRDS [24].

The relation between mode-structure and transmission, and a method to improve alignment towards single-exponential decay in a non-confocal resonator were discussed in reference [33]. In this article, the option to use a Fourier transform of the residuals to detect mode beating in the cavity was mentioned. This additional analysis of the decay transient has been added to the measurement application, as previous hardware was not powerful enough to handle the extra load. Two typical residual traces and their Fourier transform are shown in figure 2.5. On the left

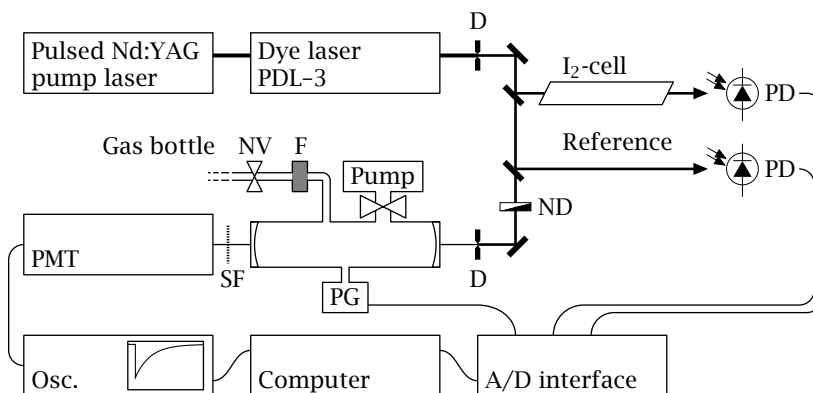


Figure 2.6 Schematic overview of the experimental setup.

D iris diaphragm ND neutral density filter [] highly reflective mirrors
 SF spectral filter NV needle valve F aerosol filter
 PD photodiode PMT photo multiplier tube PG pressure gauge

the actual residuals are shown, with the effects of digitisation clearly visible after $\sim 100 \mu\text{s}$. On the right the Fourier transform of the residuals is shown. Peaks in this spectrum show fast oscillations in the residuals, corresponding to mode-beating in the ring-down signal. These oscillations may not be apparent in the display of the residuals themselves.

2.4 Overview of the cavity ring-down setup

The basic instrument is a ‘generic pulsed cavity ring-down spectroscopy setup’. It may be helpful to refer to figure 2.6 in the following discussion. The light source is a Quanta-Ray PDL-3 pulsed dye laser, pumped by the second or third harmonic of a pulsed Nd:YAG laser. The PDL-3 has a bandwidth of about 1.5 GHz, or 0.05 cm^{-1} . Its spectral profile is by no means Gaussian – analysis with a spectrum analyser shows four to five distinct modes in the spectrum. This leads to a systematic underestimate of the measured absorption cross section, *unless* the width of the absorption feature is much broader than the width of the laser, as is the case in Rayleigh scattering and the $(\text{O}_2)_2$ collision-induced absorption resonances, measured in chapters 3 and 4–6, respectively.

The laser light is guided through a set of iris diaphragms and attenuated with a variable neutral density filter, to make sure the detector does not reach the point of saturation. Some laser dyes are so efficient, in particular the Rhodamine dyes, that the reflection of a plane glass window is used to reduce the intensity. Some of the laser light is split off using a plane glass window for use in the calibration. For continuous frequency scanned spectra – the H_2^{18}O spectra presented in chapter 8 – calibration is performed by comparing a simultaneously recorded I_2 spectrum

with a spectral atlas of I_2 [34]. The I_2 reference spectrum is recorded by a direct absorption spectroscopy technique, the incoming intensity and the transmitted intensity are measured with an integrated, gated photo diode setup and the resulting intensity is recorded by the computer. For the other measurements - Rayleigh scattering in chapter 3 and the $(O_2)_2$ measurements in chapters 5 and 6 - a different calibration technique was employed, based on an Echelle grating. These latter measurements measured the absorption cross section during a pressure-ramp, and as such the laser wavelength was kept at a fixed position during a single measurement.

The cell is evacuated with a rotary pump connected to the cell through a liquid nitrogen cold-trap, to keep the cell free from oil. The gas samples on which the absorption measurements are performed, are filtered by a sintered steel filter. The gas flow is controlled by a needle valve. Capacitance manometers are used to measure the pressure. Three different types were used: two Edwards 600 AB (0.00 Torr - 100.0 Torr) and (0.00 Torr - 1000 Torr) with an absolute accuracy of 0.15% of the reading. The third capacitance manometer is a Pfeiffer CMR 273 temperature controlled capacitance manometer (up to 10.0 mbar) with an absolute accuracy of 0.15% of the measured value as well. All these sensors produce a signal in the 0.0V to 10.0V range, and are read by the same analogue to digital converter unit that reads out the reference spectra.

The ring-down transients are detected with a photo multiplier tube, set at a relatively low voltage, in order to avoid saturation - the PMT is used to measure a continuous signal, not as a photon counting device. The highly reflective mirrors are transparent for other wavelengths and to stop stray light from reaching the PMT, a spectral filter is used to block light for which the mirror sets are transparent. The output of the PMT is recorded by a digitising oscilloscope - a LeCroy WaveRunner LT 342, with a maximum sample rate of 500 MS/s and a maximum sample length of 250 000 points. After recording several ring-down events, the transients are transferred to the computer for further analysis, following the algorithm described in reference [33]. This algorithm uses a two-step fit. In the first step an unweighted fit of the model function (2.15) to the data is performed to obtain an initial estimate of the fit parameters; during this fit the I_{offset} is kept at zero. From the fit results the statistical error in each data-point is estimated, assuming a Gaussian contribution from the electronics and a Poissonian contribution from the photon shot noise. Full analysis of the unweighted residuals has shown that these are the important sources of noise on the ring-down signal [33]. Using the estimated errors, a weighted fit of the model function (2.15) to the data is performed. To verify the correct analysis of the ring-down transient, or rather the correct alignment of the cavity, the weighted residuals are displayed on screen, as shown in figure 2.5. The variance of the weighted residuals is one, and the average is zero for a perfectly aligned cavity. These parameters are also calculated in the fitting routine, and recorded with the spectrum to verify its quality during later analysis.

There are two different methods of recording several ring-down events; one is to perform direct averaging in the oscilloscope and store the results in a trace with a higher vertical resolution, and transfer the averaged data-trace. This method is used in the alignment mode of the software, and it reduces the noise on the trace, but

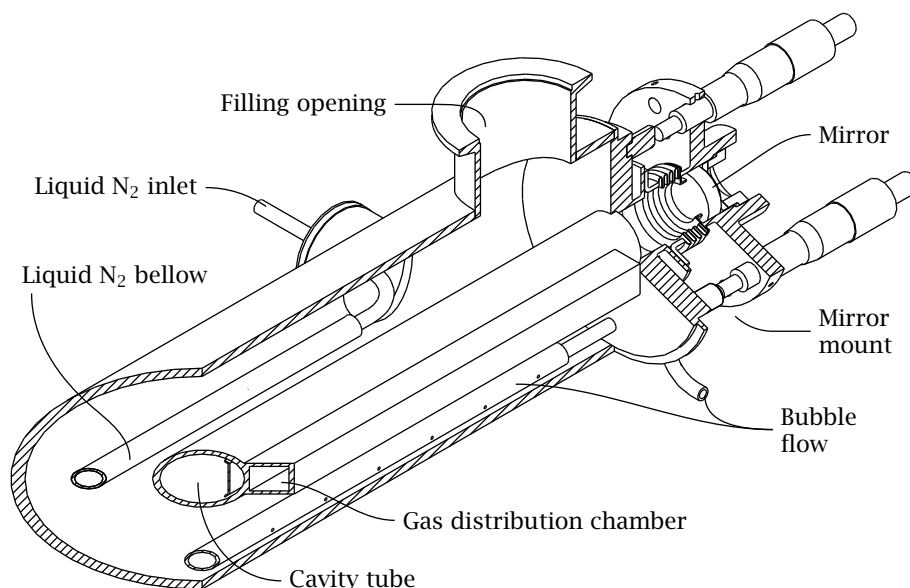


Figure 2.7 A drawing of the cell used for the pressure ramp method used in the measurements for chapters 3, 5 and 6. Not shown in this picture are the gas inlet and filter.

when there are variations on the decay time – for whatever reason – this averaging is not allowed. During a scan a different method of recording and transferring of the data is used; each individual ring-down event at a fixed laser position during a scan is stored sequentially in the memory of the oscilloscope and then transferred to the computer in batches. This is done with four to five events, each with a length of 10 000 points. Since the individual events are now available to the computer, each event can be analysed individually and the results averaged, or they can be averaged before the fitting procedure, as before. The software has an option to write the raw data to disk, and both modes of analysis can be performed off-line after the scan has finished. For the measurements in this thesis, the averaging takes place on the transients before analysis, and all points where the statistical parameters show that the fit was not good are discarded. This should take care of the considerations as to why this mode of analysis is in principle not allowed.

2.4.1 The ring-down cavity: pressure ramp, mirror-mounts and cooling

The measurements of chapters 3, 5 and 6 were performed with the pressure ramp method: an evacuated cell is filled over a period of about 15 minutes. During this time the loss-rate in the cell is recorded along with the pressure in the cell. The slope of the resulting graph – see figure 3.6 on page 32 – produces the absorption cross section. To obtain a homogeneous filling of the cavity during the pressure-ramp, and to avoid turbulence, a special cavity was constructed, shown in figure 2.7.

The mirrors on both ends form also the gas-tight seal of the cavity. To allow for the necessary flexibility for alignment while still providing a vacuum-tight seal, the mirror mounts are connected to the cavity with a set of bellows. The orientation of the mirror is controlled with three micro-meter screws.

The gas is led to the centre of the cavity through a sintered steel filter (not shown in figure 2.7). The gas reaches the gas distribution chamber and through a series of holes it is distributed into the cavity. This chamber ensures that the gas is brought into the cavity over its whole length, and that the distribution is homogeneous.

For the low temperature measurements, the space around the cavity tube is filled with acetone or ethanol. The whole system is then cooled down by a flow of liquid nitrogen through the bellow that runs parallel to the cavity tube. To ensure a good mixing and a homogeneous temperature, nitrogen gas is blown through the coolant from the tube at the bottom of the cell. The stainless steel filter mentioned above is also placed within this fluid, to cool the filter down to the temperature of the measurements. Because of its size and construction, this sintered steel filter provides a large surface area and intense contact with the gas flowing through it, ensuring that the gas will enter the ring-down cavity at the desired temperature.

Experimental verification of Rayleigh extinction in various gases

In 1899, Lord Rayleigh solved a problem that had occupied scientists throughout the centuries passed. He explained why the sky is blue and why the sunset is red, in his classic paper 'On the Transmission of Light through an Atmosphere containing Small Particles in Suspension, and on the Origin of the Blue of the Sky' [35]. In this article he used the - then newly formulated - theory of electromagnetism, to show that scattering by molecules alone was sufficient to explain the observed brightness of the blue sky. Not only did he explain these atmospheric phenomena, but he also formulated a quantitative expression for the total scattering cross section.

Rayleigh derived a frequency dependent expression for the scattering cross section as a function of the refractive index, the molecular gas density and a factor that accounts for the non-sphericity of molecules. For nitrogen his equation leads to a value of the scattering cross section of $6.8 \times 10^{-27} \text{ cm}^2 \text{ molecule}^{-1}$ at a wavelength of 500 nm. This is a very small cross section, and the extinction arising from Rayleigh scattering is difficult to detect and quantitatively verify in the laboratory - to the best of our knowledge, our laboratory was the first to measure the Rayleigh scattering cross section directly from extinction [36].

Refractive indices can be measured using interferometric techniques, and for many gases dispersion formula's are known. For most gases, including 'air' - represented by a standardised mixture, the refractive index was measured in the 1960's and 1970's. These refractive indices are used to derive the Rayleigh scattering cross sections at an accuracy considered to be sufficient for atmospheric radiative transfer calculations. However, the information on the correction factor for non-spherical molecules is sparse and the dispersion of this factor is often ignored. For this reason experimental verification of the Rayleigh extinction by other means is warranted.

In the present work the technique of cavity ring-down spectroscopy is used to measure the Rayleigh scattering cross section in various gases. These measurements are an extension of the measurements performed earlier between 15 500 and 18 000 cm^{-1} in Ar, N₂ and SF₆ [36]. Here the frequency range between 20 400 and 21 400 cm^{-1} for N₂ and Ar is added, to further test the predicted wavelength dependence - $\sigma \propto 1/\lambda^4$ - of the Rayleigh scattering cross section. The scattering cross section of the important atmospheric constituent CO₂ is measured over a larger frequency range (17 500-18 200 and 20 400-21 400 cm^{-1}). This gas is interesting from an astrophysical point of view, as the atmospheres of Mars and Venus consist mainly of CO₂. Also the correction factor for the non-sphericity is particularly large for CO₂. Finally, measurements of the scattering cross sections at 532 nm - the second harmonic of a Nd:YAG laser, a wavelength frequently used in LIDAR (Light

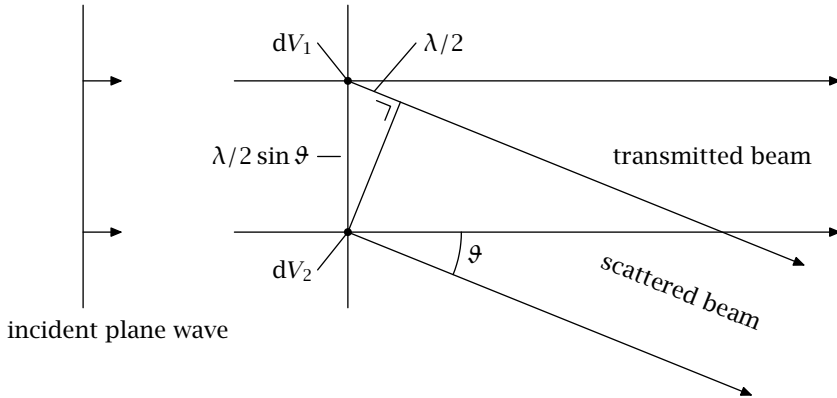


Figure 3.1 Light scattering cannot occur in completely homogeneous matter.

detection and ranging) applications - in CO₂, N₂, Ar, N₂O, CH₄, CO, SF₆ and O₂ are performed as well.

3.1 Rayleigh scattering

Light scattering is a consequence of inhomogeneities in matter. If a completely homogeneous piece of matter is illuminated by a plane wave, see figure 3.1, and it is assumed that the volume dV_1 scatters light in the direction ϑ , then for all directions $\vartheta \neq 0$ light scattered by a volume dV_2 will interfere destructively with the light field from dV_1 . Because the material is completely homogeneous, the argument may be applied to all volumes dV in the material; it follows that only scattering in the forward direction can occur. This coherent forward scattering causes a phase delay and is the origin of the index of refraction [37].

The first source of inhomogeneities in matter are the atoms or molecules themselves. The electric field from the incident light will induce oscillating electric dipoles in the molecules. These induced dipoles radiate, causing a secondary light field. Because in a gas the positions of the molecules are not correlated, interference between the secondary waves of the various particles cannot occur, and the intensities may be added directly. The radiation by these induced dipoles is known as Rayleigh scattering.

Rayleigh scattering is an approximation that holds when the wavelength of the incident radiation is much larger than the size of the particles. The underlying reason for this is that the electric field of the incident radiation is assumed to be homogeneous over the particle and therefore the dipole approximation may be used. If the particle is larger, higher order multi pole terms need to be included. The classical description of Rayleigh scattering requires the combination of two known elements: the radiation of an oscillating dipole and the magnitude of the induced dipole.

3.2 Classical electrodynamic derivation of Rayleigh scattering

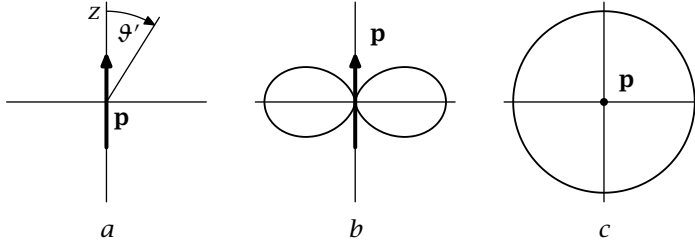


Figure 3.2 *The intensity distribution of dipole radiation. a – The coordinate system. b – The intensity distribution in the plane of the dipole. c – The intensity distribution in the plane perpendicular to the dipole.*

3.2 Classical electrodynamic derivation of Rayleigh scattering

Classic electrodynamic theory describes how an oscillating electric dipole radiates. The intensity distribution of the emitted radiation by a dipole is given by [38]:

$$I_{\text{rad}}(\vartheta') = \left(\frac{\omega^4}{32\varepsilon_0\pi^2c^3} p_{\text{max}}^2 \right) \sin^2 \vartheta' \quad (3.1)$$

with ϑ' the angle between the axis of the dipole and the direction of observation, ω the angular frequency of the radiation, p_{max} the maximum value of the dipole and ε_0 the permittivity of vacuum. Note that the intensity in the direction of the dipole axis is zero – a graphical representation of the intensity distribution is shown in figure 3.2

Integration of the intensity distribution over all directions yields the total power that is radiated by the dipole:

$$P_{\text{rad}} = \left(\frac{\omega^4}{32\varepsilon_0\pi^2c^3} p_{\text{max}}^2 \right) \int_{\varphi=0}^{2\pi} \int_{\vartheta'=0}^{\pi} \sin^3 \vartheta' d\vartheta' d\varphi = \frac{1}{4\pi\varepsilon_0} \frac{\omega^4}{3c^3} p_{\text{max}}^2 \quad (3.2)$$

3.2.1 The magnitude of the induced dipole

The macroscopic polarisation \mathbf{P} induced in a material by a field \mathbf{E} for a linear dielectric material is given by:

$$\mathbf{P} = \varepsilon_0 \chi_e \mathbf{E} \quad (3.3)$$

with \mathbf{E} the macroscopic field and χ_e the electric susceptibility. At the microscopic level, the induced dipole for a single particle in a linear material is given by:

$$\mathbf{p} = \alpha_{\text{SI}} \mathbf{E}_{\text{local}} \quad (3.4)$$

Here the field $\mathbf{E}_{\text{local}}$ is the electric field at the site of the particle – thus including the influence of neighbouring induced dipoles – and the proportionality constant α_{SI} is the classical molecular polarisability, which can be expressed in terms of

χ_e , a quantity known for many substances.¹ In a diluted medium, the effect of neighbouring particles may be ignored and the macroscopic polarisation is given by: $\mathbf{P} = N\mathbf{p} = N\alpha_{\text{SI}}\mathbf{E}$, which leads to $\alpha_{\text{SI}} = \chi_e \epsilon_0 / N$, with N the density in m^{-3} . With the electric permeability $\epsilon = \epsilon_0(1 + \chi_e)$, α_{SI} can be expressed as:

$$\alpha_{\text{SI}} = \frac{\epsilon_0}{N} \left(\frac{\epsilon}{\epsilon_0} - 1 \right) = \frac{\epsilon_0}{N} (n^2 - 1) \quad (3.5)$$

In the last step of equation (3.5), the propagation speed of electromagnetic waves in vacuum ($c_{\text{vac}} = 1/\sqrt{\epsilon_0\mu_0}$), the speed of light in a medium ($c_{\text{med}} = 1/\sqrt{\epsilon\mu}$) and the refractive index $n = c_{\text{vac}}/c_{\text{med}}$ were used. The magnetic susceptibility was ignored – which is reasonable at optical frequencies – hence $\mu = \mu_0$.

Inclusion of the influence of neighbouring particles leads to a correction on equation (3.5). It can be shown that the classical molecular polarisability is given by the Lorentz-Lorenz relation, if the effects of neighbouring particles are taken into account [38]:

$$\alpha_{\text{SI}} = \frac{3\epsilon_0}{N} \left(\frac{n^2 - 1}{n^2 + 2} \right) \quad (3.6)$$

In most gases $n \approx 1$, and the error made by the approximation is small. For example in air the error on α made is by the approximation is about 0.05% [40]. Note that α is the polarisability *per particle*, and that it is independent of the density. The refractive index n in equation (3.6) is the refractive index at density N .

3.2.2 The scattering cross section

The intensity of the incident radiation and its electric field are related by the Poynting vector, with a magnitude $I_{\text{inc}} = \frac{1}{2}c\epsilon_0 E_{\text{max}}^2$. This can be combined with equation (3.6), giving the induced dipole p_{max} . Combining the induced dipole with equation (3.2) yields:

$$P_{\text{sc}} = I_{\text{inc}} \frac{3}{2\pi} \frac{\omega^4}{c^4} \frac{1}{N^2} \left(\frac{n^2 - 1}{n^2 + 2} \right)^2 \quad (3.7)$$

Equation (3.7) is the power scattered by a single atom or molecule when it is placed in a light field with intensity I_{inc} . The surface σ is the area that would receive the same power as is scattered by a particle. This surface is known as the scattering cross section, for which one finds $\sigma = P_{\text{sc}}/I_{\text{inc}}$:

$$\sigma = \frac{3}{2\pi} \frac{\omega^4}{c^4} \frac{1}{N^2} \left(\frac{n^2 - 1}{n^2 + 2} \right)^2 = \frac{24\pi^3}{\lambda^4 N^2} \left(\frac{n^2 - 1}{n^2 + 2} \right)^2, \quad (3.8)$$

where $\omega = 2\pi\nu = 2\pi c/\lambda$ was used. With N in molecule m^{-3} and λ in m, this gives the scattering cross section in $\text{m}^2/\text{molecule}$.

¹ The SI subscript indicates that this quantity is in S.I. units: $[\alpha_{\text{SI}}] = \text{Fm}^2$. In literature the volume polarisability is often used: $\alpha_{\text{vol}} \equiv \alpha_{\text{SI}}/4\pi\epsilon_0$, which has the dimensions of a volume [39].

3.3 Scattering distribution for natural light

In atmospheric physics the cross section is commonly expressed in cm^2 per molecule. With $\omega = 2\pi c\bar{\nu}$ (c in cm s^{-1}) and N in molecule cm^{-3} , the cross section in equation (3.8) becomes:

$$\sigma_{\bar{\nu}} = \frac{24\pi^3\bar{\nu}^4}{N^2} \left(\frac{n_{\bar{\nu}}^2 - 1}{n_{\bar{\nu}}^2 + 2} \right)^2 \quad (3.9)$$

As a reminder that the refractive index also depends on the frequency of the driving light, the subscript $\bar{\nu}$ is added. At first glance it would seem that the cross section depends on the density of the gas. However it should be considered that the refractive index is a collective effect and that the Lorentz-Lorenz relation (3.6) gives the molecular polarisability for a *single* molecule and therefore equation (3.9) is independent of the density. Equation (3.9) can also be written in terms of the molecular volume polarisability:

$$\sigma_{\bar{\nu}} = \frac{128}{3} \pi^5 \alpha_{\text{vol}}^2 \bar{\nu}^4 \quad (3.10)$$

with α_{vol} in cm^3 and $\bar{\nu}$ in cm^{-1} . Equation (3.10) explicitly shows that the scattering cross section is independent of the density.

3.3 Scattering distribution for natural light

Because the individual scatterers are located at random positions, the scattered radiation from each of the molecules is incoherent and the intensities can be added. The direction of the induced dipoles is determined by the electric field of the incident radiation. If the incident radiation is linearly polarised then all induced dipoles will oscillate in the same direction. This means that the angular distribution of the total intensity of the scattered radiation is a sum of the scattered intensities of the individual particles. The distribution of the scattered radiation per particle for linearly polarised incident radiation is given by [41]:

$$I_p(\vartheta') = \left(\frac{9\pi^2\bar{\nu}^4}{N^2} \right) \left(\frac{n^2 - 1}{n^2 + 2} \right)^2 (\sin^2 \vartheta'), \quad (3.11)$$

with ϑ' the angle between the polarisation of the light - and therefore the induced dipoles - and the direction of observation, as indicated in figure 3.2(a).

Natural light is a linear combination of two independent, perpendicularly polarised light waves, $I_n = \frac{1}{2} (I_{\perp} + I_{\parallel})$. Because the electric field of natural light has no preferential orientation, the distribution must be invariant for rotation around the propagation direction. The total distribution of the scattered light for incident unpolarised light is the sum of the scattered intensities from the two perpendicular components. Because *any* plane that contains the propagation direction of the light wave can be chosen to calculate the total distribution, the distributions from figures 3.2(b) and 3.2(c) can be added, as is shown in figure 3.3. After changing to

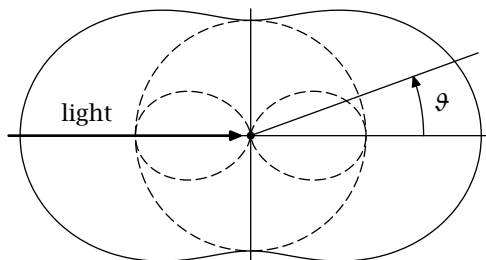


Figure 3.3 The distribution of the scattered radiation for natural light, incident from the left. The dashed lines are the distributions of the two perpendicular polarisations, the drawn line the distribution for natural light. The indicated angle ϑ is the scattering angle.

the angle ϑ , which is the angle between the propagation direction and the direction of observation, the total distribution becomes [41]:

$$I_n(\vartheta) = \left(\frac{9\pi^2 \bar{v}^4}{2N^2} \right) \left(\frac{n^2 - 1}{n^2 + 2} \right)^2 (1 + \cos^2 \vartheta), \quad (3.12)$$

Figure 3.3 illustrates that the contribution to the scattered radiation at 90° comes only from one component of the natural light. Since the electromagnetic radiation from a dipole is polarised, and the light scattered at 90° contains only a contribution from aligned dipoles, the light scattered at these angles must be polarised as well.

3.4 Non-spherical molecules

The calculations performed above are only correct for spherically symmetric particles. Molecules in general have a molecular polarisability that depends on the orientation of the molecule with respect to the electric field. This problem was already recognised by Rayleigh [35].

Between 1918 and 1920 Rayleigh's son measured the incomplete polarisation of light scattered by molecules at 90° [42, 43]. This effect is known as the *depolarisation*, which is equal to the intensity ratio of horizontal and vertical polarisations of the scattered light: $\rho = I_\perp / I_\parallel$. Note that since the distributions for natural- and polarised light are different, the depolarisation ratios ρ_n and ρ_p are also different.

In 1923, King [44] solved the problem of scattering by non-spherical particles, i.e. particles where the polarisability of the particles is non-isotropic. For a non-spherical particle, equation (3.4) becomes a tensor equation:

$$p_i = \sum_j \alpha_{ij} E_j \quad \text{for } i, j = x, y, z. \quad (3.13)$$

A consequence of equation (3.13) is that the induced dipole and the electric field do *not* have to be aligned, causing an incomplete polarisation of the light scattered at right angles. In its most general form the polarisability tensor α_{ij} is a 3×3

tensor, but it can be split into a diagonal component α_{ii} , a symmetric component $\alpha_{ij}^{(s)} = \alpha_{ji}^{(s)}$ and an anti-symmetric component $\alpha_{ij}^{(a)} = -\alpha_{ji}^{(a)}$. The effects caused by the off-diagonal components will be discussed in section 3.5.

The anisotropy of the polarisability affects the scattering cross section and the distribution of the scattered light. The effect is commonly expressed in terms of the depolarisation ratio. This can be a source of confusion [45], since the depolarisation for natural- and polarised light is different. Because of symmetry arguments, the cross section for scattering must be the same for natural- and polarised light. Natural light is a linear combination of two independent, perpendicularly polarised light waves, $I_{\text{nat}} = \frac{1}{2} (I_{\parallel} + I_{\perp})$. The axis orientation is arbitrary, and therefore $\sigma_{\parallel} = \sigma_{\perp} = \sigma_{\text{nat}}$.

Calculating the scattering cross section and the distribution of the scattered light, requires integration over all possible orientations of the molecule. The derivation is tedious but straightforward [41, 44, 46]. The full treatment in these references include the polarisation of the propagating beam. From the distribution found in this treatment, one can deduce the depolarisation ratio in terms of the components of the polarisability tensor along the principal axes of the molecule, α_{ii} .

$$\rho_n = \frac{2\sum_i \alpha_{ii}^2 - 2\sum_{i<j} \alpha_{ii}\alpha_{jj}}{4\sum_i \alpha_{ii}^2 + \sum_{i<j} \alpha_{ii}\alpha_{jj}} \quad \rho_p = \frac{\sum_i \alpha_{ii}^2 - \sum_{i<j} \alpha_{ii}\alpha_{jj}}{3\sum_i \alpha_{ii}^2 + 2\sum_{i<j} \alpha_{ii}\alpha_{jj}} \quad (3.14)$$

From equation (3.14), we find the relations between ρ_n and ρ_p : $\rho_n = 2\rho_p/(1 + \rho_p)$ and $\rho_p = \rho_n/(2 - \rho_n)$. The depolarisation ratios depend on the frequency of the primary light, just as the refractive index depends on frequency, but the functional form may be very different. The refractive index and the polarisability are related by equation (3.6). In this expression the classical polarisability is used, but for non-spherical particles there is no such value, and α in equation (3.6) has to be replaced with $\bar{\alpha} = \frac{1}{3}\sum_i \alpha_{ii}$ [47].

For linear and symmetric top molecules, a simplification can be made. With $\alpha_{\parallel} = \alpha_{11}$ the polarisability along the symmetry axis of the molecule, $\alpha_{\perp} = \alpha_{22} = \alpha_{33}$ the polarisability perpendicular to it, and $\gamma = \alpha_{\parallel} - \alpha_{\perp}$, one finds:

$$\rho_p = \frac{\gamma_{\bar{v}}^2}{15\bar{\alpha}_{\bar{v}}^2 + \frac{4}{3}\gamma_{\bar{v}}^2} \quad (3.15)$$

Integration of the full intensity distribution leads to the scattering cross section. The final result is the same as the original result found by Rayleigh, equation (3.9), with an additional correction factor to correct for the anisotropy. This correction factor was first found by King [44, 46].

$$\sigma_{\bar{v}} = \frac{24\pi^3\bar{v}^4}{N^2} \left(\frac{n_{\bar{v}}^2 - 1}{n_{\bar{v}}^2 + 2} \right)^2 F_k(\bar{v}), \quad (3.16)$$

with $F_k(\bar{v})$ the King correction factor:

$$F_k(\bar{v})(\bar{v}) = \frac{6 + 3\rho_n(\bar{v})}{6 - 7\rho_n(\bar{v})} = \frac{3 + 6\rho_p(\bar{v})}{3 - 4\rho_p(\bar{v})} = 1 + 2 \left(\frac{\gamma_{\bar{v}}}{3\bar{\alpha}_{\bar{v}}} \right)^2 \quad (3.17)$$

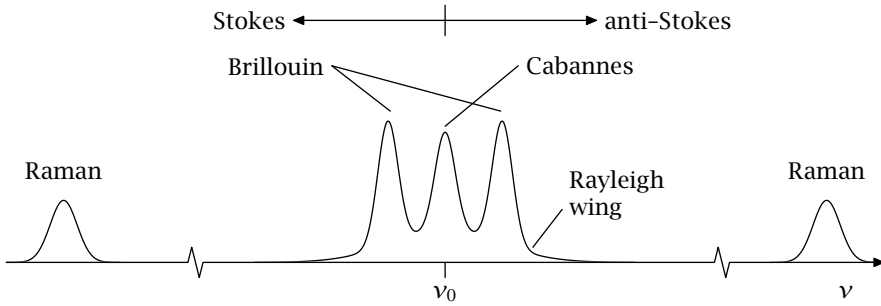


Figure 3.4 Spectrum of the scattered radiation.

Note that $F_k(\bar{\nu}) \geq 1$, implying that the scattering cross section will always be larger for non-spherical particles compared to spherical particles with the same refractive index. With the theoretical result from equation (3.16), one can calculate the extinction coefficient in a gas, if the refractive index at a specified density, the density and the depolarisation ratio are known. For nitrogen ρ_n at a wavelength of 500 nm is equal to 0.0213, leading to a King correction factor at 500 nm of 1.035 [48].

3.5 Relation to other forms of scattering

With the result of equation (3.16), the most important inhomogeneity in matter has been dealt with. The classic derivation by Rayleigh [35] and King [44] was followed. In this derivation, in terms of classical electrodynamics, the motion nor internal quantised excitation of the molecules is considered. The scattering is calculated during an infinitely short period, and in view of Fourier limitations, no information can be obtained about the frequency of the scattered radiation. More sophisticated theories of light scattering [37] reveal that the spectrum is centred around the frequency of the driving light, but molecular motion adds other spectral features, shown in figure 3.4.

The peaks shown here are due to scattering on other inhomogeneities. The central unshifted peak - sometimes referred to as the *Rayleigh centre* peak, but it is better to refer to this peak as the *Cabannes* peak, in order to avoid confusion - is caused by isobaric density fluctuations that are proportional to entropy fluctuations. The density fluctuations cause a local change in the index of refraction, from which light is scattered.

The Brillouin peaks originate from scattering off adiabatic density fluctuations, better known as acoustic waves. In the scattering process, energy is transferred between the acoustic wave and the light field. If the acoustic wave absorbs energy from incident radiation, the scattered radiation is red-shifted. This is known as the *Stokes* component. The component receiving a blue shift, is known as the *anti-Stokes* component. The maximum shift occurs for back-scattering, while forward

scattered light is unshifted. For 1 bar nitrogen at 273 K illuminated by 500 nm light, the maximum shift with respect to the incident radiation is found to be 0.04 cm^{-1} [37]. The approximate ratio between the Cabannes and the sum of the Brillouin peaks was predicted by Landau and Placzek [49]:

$$\frac{I_C}{2I_B} = \frac{c_p - c_v}{c_v} = \tilde{\gamma} - 1, \quad (3.18)$$

with c_p the isobaric heat capacity, c_v the heat capacity at constant volume and $\tilde{\gamma} = c_p/c_v$ the adiabatic index. From the experimental values of $\tilde{\gamma}$, given in table 3.1, it follows that the intensity of the Brillouin peaks is even larger than the Cabannes peak; in liquid water the Cabannes peak is practically absent. However, experimentally the central peak was frequently observed to be more intense than the prediction of Landau-Placzek; this phenomenon was explained in terms of a refinement of the theory with a dispersion relation for the thermodynamic properties [49].

Brillouin scattering relates to the diagonal component of the polarisability tensor and can therefore also occur in atomic gases. The off-diagonal components $\alpha_{ij}^{(s)}$ and $\alpha_{ij}^{(a)}$ of the polarisability tensor are responsible for another class of scattering processes. Both types are known as *depolarised* scattering, as the depolarisation for those types of scattering is much higher than for the Brillouin and Cabannes peaks [37, 51].

One form of depolarised scattering is Raman scattering, which originates from the variation of the polarisability due to the vibration or rotation of the molecule. In a classical picture, changes in the internuclear distance or a change in orientation relative to the electric field of the incident radiation cause a change in the strength of the induced dipole and therefore an amplitude modulation on the secondary wave, leading to sidebands on the spectrum.

In a quantum mechanical model, two different states are coupled by the polarisability tensor through a virtual level, as schematically shown in figure 3.5. The probability for this to occur is related to a *change* in the polarisability. Detailed analysis shows that this coupling is caused by the anti-symmetric part of the polarisability tensor $\alpha_{ij}^{(a)}$ [51]. The difference in energy between the states is subtracted from (Stokes) or added to (anti-Stokes) the scattered radiation. Two different types of Raman scattering exist: rotational- and vibrational Raman scattering, the first leaves the molecule in a different rotational state (with selection rule $\Delta J = \pm 2$) and the second in a different vibrational state (with selection rule

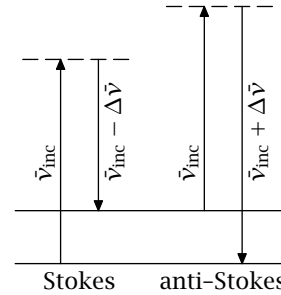


Figure 3.5 Raman transition.

Table 3.1 The adiabatic index for a few gases [50].

Gas	O ₂	N ₂	Air	CH ₄	H ₂	D ₂	Ar	CO ₂	CO
$\tilde{\gamma}$	1.40	1.40	1.40	1.31	1.41	1.73	1.66	1.31	1.40

$\Delta\nu = \pm 1$). Weak overtone vibrational Raman lines ($\Delta\nu = +2$) have been observed [52]. The Boltzmann distribution leads to very low occupation levels of higher vibrational levels in atmospheric gases, even at elevated temperatures [53]; the anti-Stokes vibrational Raman peak is therefore usually very weak, and under atmospheric condition practically not existent. The situation is different for rotational Raman scattering: the lower rotational levels are occupied and the anti-Stokes rotational Raman peaks have the same intensity as the Stokes counterparts. Combinations of a rotational and vibrational transition can occur, leading to a rotational structure around the vibrational Raman peak. In these Raman transitions a change of rotational quantum number occurs, $\Delta J = \pm 2$, giving rise to O- and S-branches. A transition without change in rotational quantum number $\Delta J = 0$ gives the Q-branch of the ro-vibrational Raman scattering. The vibrational Raman peak has a separation of 2330.7 cm^{-1} from the central structure in N_2 . The separation of the rotational Raman structure is obviously much smaller, about 8 cm^{-1} in N_2 [53]. The separation is in both cases much larger than the splitting of Brillouin scattering. The ratio of the scattering cross sections of Raman- and total Rayleigh scattering is small. For example in N_2 the ratio is 2.3% for rotational- and 0.07% for vibrational Raman scattering, both for incident radiation of 500 nm [54].

The off-diagonal, symmetric part of the polarisability tensor, $\alpha_{ij}^{(s)}$, is also responsible for the Rayleigh-wing scattering, related to fluctuations in the orientation of anisotropic molecules. Rayleigh-wing scattering is strongly depolarised and forms a broad band around the central structure, with a width of about 5 cm^{-1} [37].

The polarisability tensor can be calculated from the quantum mechanical structure of the atom or molecule. The transition strengths of all possible optical transitions have to be included in the calculation, including those to the continuum states [47, 55]. From the polarisability tensor, the refractive index can be calculated by means of the Lorentz-Lorenz relation (3.6). Also the depolarisation ratio and Raman scattering cross section can be calculated from the tensor [54, 56]. Quantum chemical computations can be used to calculate these properties from first principles, which has been done for hydrogen and nitrogen [57–60]. From [60] a Rayleigh scattering cross section in nitrogen can be calculated, using only *ab initio* calculations. This theoretical result is found to be $6.2 \times 10^{-27} \text{ cm}^2/\text{molecule}$.

In this work the Rayleigh extinction is measured. This is the sum of all scattering modes discussed above – Cabannes, Brillouin, Raman and Rayleigh-wing scattering – and absorption. Since there are no absorptions in the region investigated in this work, the measured extinction is equal to the total Rayleigh scattering. For the analysis of atmospheric measurements, the Rayleigh scattering cross sections is usually calculated from the refractive index, using equations (3.16) and (3.17). The refractive index is commonly measured with an interferometric technique, such as described in reference [61], while the depolarisation ratio is measured directly through the ratio of the perpendicular and parallel polarisations of the scattered radiation at 90° as described in references [47, 55]. Our method, discussed in the next section, measures the extinction directly, and yields an independent verification of the Rayleigh scattering cross section.

3.6 The experimental method

As mentioned in the introduction of this chapter, the Rayleigh scattering cross section is small. In N_2 at 500 nm a scattering cross section of $6.8 \times 10^{-27} \text{ cm}^2/\text{molecule}$ is found from the measured depolarisation and refractive index [48]. At atmospheric pressure, the loss due to scattering is $170 \times 10^{-9} \text{ cm}^{-1}$. Detecting these losses accurately requires a sensitive measurement technique. In this work cavity ring-down spectroscopy was employed to detect the scattering losses in a compact setup. A high level of sensitivity is accomplished by recording large data sets and performing consecutive averaging procedures. For a general description of the cavity ring-down technique we refer to chapter 2.

Our detection of the Rayleigh extinction depends on the decay rate of the ring-down cavity. Two types of losses occur in the cavity: losses on the mirrors and losses due to scattering and absorption by the gas: $\beta_{\bar{\nu}} = c |\ln \mathcal{R}_{\bar{\nu}}| / d + c \sigma_{\bar{\nu}} N$. To separate scattering losses from the decay rate of the empty cell, the decay rate is constantly monitored during a pressure ramp. While the cell is filled with gas over a period of about 15 minutes, the losses due scattering by the gas increases linearly with the density, while the losses on the mirrors remain constant. Note that the pressure ramp itself does not have to be linear in time, although best results are achieved with a smooth ramp. During the pressure ramp the frequency of the laser is kept at a fixed position and between 1000 and 1200 measurements of the loss rate - with a pulsed laser at a 10 Hz repetition frequency - are performed. Each of these measurements is the average of four decay events. Typical pressure ramps in measurements of three different gases are shown in figure 3.6.

The Rayleigh scattering cross section follows from a linear fit of the loss rate versus the density in the cell. The slope of the plots shown in figure 3.6 is equal to $\sigma_{\bar{\nu}}$. The reflectivity of the mirrors determine the vertical offset and the signal-to-noise ratio on the measurement.

The laser that was used to excite the ring-down cavity was a pulsed dye laser with a bandwidth of 0.05 cm^{-1} and a pulse duration of 5 ns. A grating spectrometer in Echelle configuration with a neon spectral reference lamp was used for frequency calibration. For the measurements at $18\,788.4 \text{ cm}^{-1}$, the second harmonic of the unseeded Nd:YAG pump-laser was used directly. The reflectivity of the mirrors and the dyes used are listed in table 3.2. Although several mirror sets were used, all mirrors had the same radius of curvature of 100 cm. The same cell was used to build all cavities, and the distance between the mirrors was 82 cm.

The flow of gas was controlled with a needle valve and the gas was purged through a sintered stainless steel filter with $0.5 \mu\text{m}$ pores to remove dust and aerosols. The cell has buffer chambers welded onto its side, to distribute the gas quickly and evenly throughout the cell, as was shown in figure 2.7 on page 19. Smooth and slow pressurisation of the cell is important to avoid turbulence. The needle valve is set in a way that a single pressurisation scan of an evacuated cell up to 1 bar takes about 15 minutes. The pressure was measured by a capacitance manometer (Edwards 600 AB; 2 hPa accuracy) and recorded simultaneously with

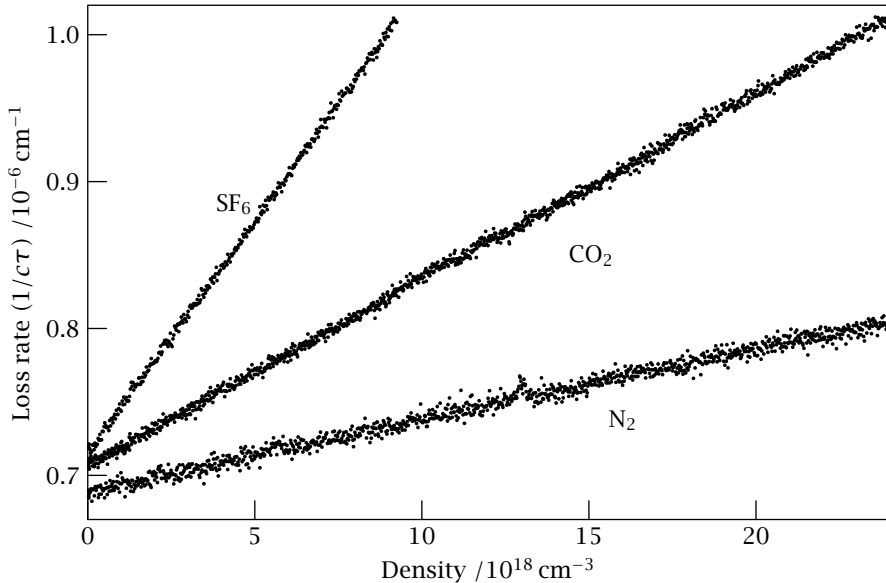


Figure 3.6 Extinction as a function of the density in the cell for CO_2 , SF_6 and N_2 at $18\,788.4\text{ cm}^{-1}$. The difference in offset for the empty cell is caused by a change in cleanliness of the mirrors, the water content of the dielectric layer and the particular alignment condition of the cavity.

Table 3.2 Experimental circumstances for the Rayleigh scattering experiments.

Wavenumber range / cm^{-1}	Mirror reflectivity \mathcal{R}_v	Laser and dye
15 500 - 17 900 ^a	99.98 - 99.997%	various dyes
17 500 - 18 100 ^b	> 99.99%	Rhodamine 6G
18 788.4	> 99.99%	2 nd harmonic Nd:YAG
20 400 - 21 400	99.98 - 99.995%	Coumarine 480

^a Ar and N_2 , measurements by Naus and Ubachs [36] ^b CO_2

the decay rates. All measurements were performed at room temperature, at about 20°C . A more accurate temperature of the cell is needed to calculate the density from the pressure. For this reason the temperature was measured as well, using a National Semiconductor LM50B sensor. The ideal gas law was used to calculate the density from the measured pressure and temperature, assumed to cause a negligible error at the densities and pressures used here.

A small but systematic underestimate of the scattering cross section is caused by forward and backward scattering. Light that is scattered back does not necessarily leave the cavity, but can continue to contribute to the ring-down signal. The acceptance angle for this to occur is small, and the error is estimated to be less than

3.7 Rayleigh scattering in argon, nitrogen and carbon dioxide

0.01%, taking into account the scattering distribution and the stability criterion of the cavity. Figure 3.7 shows the geometric configuration.

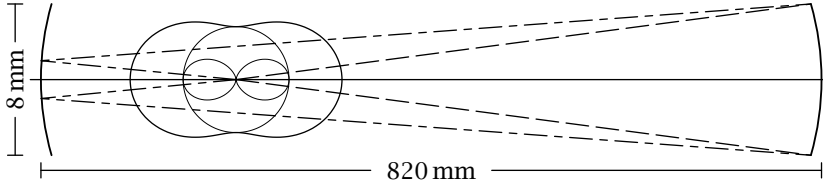


Figure 3.7 A fraction of the scattered light will fulfil the stability criteria of the cavity and continue to circulate. Drawing not to scale.

3.7 Rayleigh scattering in argon, nitrogen and carbon dioxide between $17\,500\text{ cm}^{-1}$ and $21\,400\text{ cm}^{-1}$

The extinction due to Rayleigh scattering was measured over a wide frequency range in argon, nitrogen and carbon dioxide. As mentioned before, these measurements are combined with earlier results by Naus and Ubachs [36]. Thirteen new frequencies for argon, twenty three for nitrogen and twenty two for carbon dioxide were added in the blue, as well as a further twenty five in the yellow region for carbon dioxide. The measurements performed with the second harmonic of the Nd:YAG pump laser are discussed in section 3.8. The Rayleigh scattering cross sections, as determined from the decay rates are plotted in figures 3.8 and 3.9 as a function of frequency.

3.7.1 Refractive indices for Ar, N₂ and CO₂

The measured Rayleigh scattering cross sections are compared to cross section calculated with equations (3.16) and (3.17) from measured refractive indices and depolarisation ratios. The refractive indices given here are scaled to the density at 15 °C and 1013 hPa, or $25.47 \times 10^{18}\text{ cm}^{-3}$.

Argon Peck and Fisher [62] measured the refractive index in argon. The dispersion relation they give is valid for the range $5000\text{ cm}^{-1} < \tilde{\nu} < 33\,000\text{ cm}^{-1}$.

$$(n - 1) \times 10^8 = 6432.135 + \frac{286.060\,21 \times 10^{12}}{14.4 \times 10^9 - (\tilde{\nu}/\text{cm}^{-1})^2} \quad (3.19)$$

Because argon is assumed to be spherical, the depolarisation is taken to be zero.

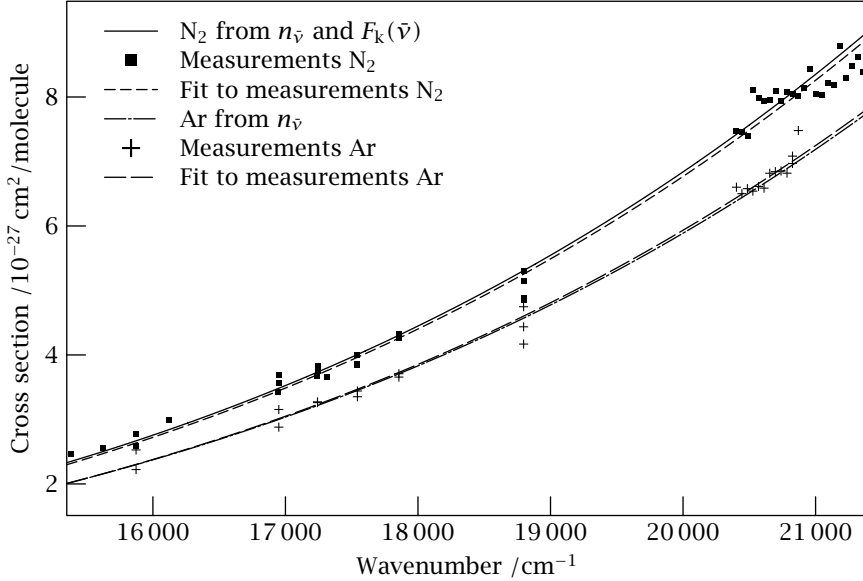


Figure 3.8 Wavelength dependent Rayleigh scattering cross sections in Ar and N₂ between 15 400 cm⁻¹ and 21 400 cm⁻¹. The curves are calculated from the refractive index [48, 62] and, in the case of N₂, the depolarisation [48]. Fits of equation (3.25) to the measured data are also shown.

Nitrogen The refractive index of N₂ in the wavelength range 468 nm ≤ λ_{vac} ≤ 2059 nm was measured by Peck and Khanna [64]. The dispersion relation they found for the range 4860 cm⁻¹ < $\bar{\nu}$ < 21 360 cm⁻¹, when scaled to 15 °C and 1013 hPa, is given by:

$$(n - 1) \times 10^8 = 6498.2 + \frac{307.433\,05 \times 10^{12}}{14.4 \times 10^9 - (\bar{\nu}/\text{cm}^{-1})^2} \quad (3.20)$$

Bates [48] gives a dispersion relation for the range 21 360 cm⁻¹ < $\bar{\nu}$ < 39 370 cm⁻¹, as an interpolation between the previously mentioned measurements and measurements by Abjean *et al.* [65] in the ultraviolet.

$$(n - 1) \times 10^8 = 5677.465 + \frac{318.818\,74 \times 10^{12}}{14.4 \times 10^9 - (\bar{\nu}/\text{cm}^{-1})^2} \quad (3.21)$$

Nitrogen is a molecule, and therefore it has a non-zero depolarisation. Bates [48] gives a dispersion relation for the King correction factor $F_k(\bar{\nu})$, based on measurements by Alms *et al.* [47] and Bridge and Buckingham [55] and calculations by Oddershede and Svendsen [60].

$$F_k(\bar{\nu}) = 1.034 + 3.17 \times 10^{-12} (\bar{\nu}/\text{cm}^{-1})^2 \quad (3.22)$$

Carbon dioxide Bideau-Mehu *et al.* [63] have measured the refractive index of CO₂ using an interferometric technique. Their article contains a small typographical

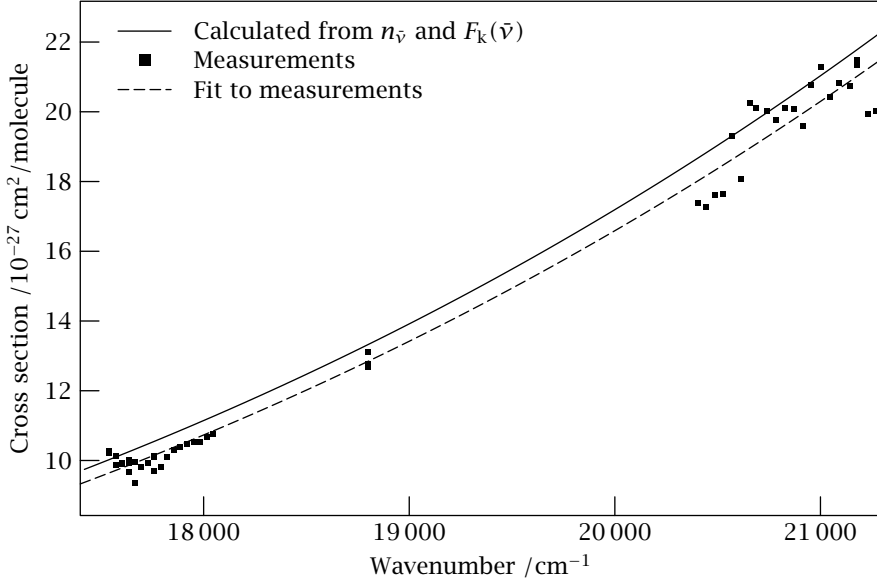


Figure 3.9 Wavelength dependent Rayleigh scattering cross sections in CO_2 between $17\,400\text{ cm}^{-1}$ and $21\,400\text{ cm}^{-1}$. The drawn curve is calculated from a measured dispersion relation of the refractive index [63] and the King correction factor, equation (3.24). Fits of equation (3.25) to the measured data are also shown.

error, and the corrected formula, scaled to 15°C and 1013 hPa , is given below.

$$\begin{aligned}
 (n - 1) = 1.1427 \times 10^6 & \left(\frac{5799.25}{(128\,908.9)^2 - (\tilde{\nu}/\text{cm}^{-1})^2} \right. \\
 & + \frac{120.05}{(89\,223.8)^2 - (\tilde{\nu}/\text{cm}^{-1})^2} + \frac{5.3334}{(75\,037.5)^2 - (\tilde{\nu}/\text{cm}^{-1})^2} \\
 & \left. + \frac{4.3244}{(67\,837.7)^2 - (\tilde{\nu}/\text{cm}^{-1})^2} + \frac{0.121\,8145 \times 10^{-4}}{(2418.136)^2 - (\tilde{\nu}/\text{cm}^{-1})^2} \right) \quad (3.23)
 \end{aligned}$$

Because of the linear configuration of the CO_2 molecule, a large depolarisation is expected. Alms *et al.* [47] have performed measurements of the depolarisation, and with the aid of equation (3.17) the King correction factors were calculated. The parameters of the model function used by Bates [48] for N_2 was then fitted to obtain a dispersion relation for the King correction factor in CO_2 .

$$F_k(\tilde{\nu}) = (1.1364 \pm 0.0005) + (25.3 \pm 1.5) \times 10^{-12} (\tilde{\nu}/\text{cm}^{-1})^2 \quad (3.24)$$

The differences between equation (3.24) and the measured King correction factors are less than 0.5%. Since the measurements from Alms *et al.* [47] cover a wider frequency range than our spectrum, no extrapolation was needed, and the same accuracy is assumed for the whole frequency range. A plot of the fit can be found in figure 3.11.

Table 3.3 Values for the parameters in equation (3.25). Values in parentheses are 1 σ errors in the last digits.

Gas	$\bar{\sigma}_{\text{refr. index}}$ /10 ⁻⁴⁵ cm ² molecule ⁻¹	$\bar{\sigma}_{\text{exp}}$	$\delta_{\text{refr. index}}$	δ_{exp}	Δ_{avg}
Ar	14.68(3)	14.21(8)	0.0930(2)	0.0968(5)	0.4%
N ₂	16.31(4)	18.83(9)	0.0974(3)	0.0817(5)	-0.7%
CO ₂	28.49(9)	27.42(14)	0.1343(3)	0.1343(5)	-3.9%

The larger frequency range in the present work with respect to the range covered by Naus and Ubachs [36] allows for better verification of the frequency dependence of the scattering cross section. As mentioned before the Rayleigh scattering cross section is not exactly proportional to $\bar{\nu}^4$, due to both the dispersion of the refractive index and the King correction factor. Several authors have suggested a variety of fitting equations to account for this difference. From Teillet [66] the following equation to describe frequency dependence of the Rayleigh scattering is taken:

$$\sigma_{\bar{\nu}} = \bar{\sigma} (\bar{\nu}/\text{cm}^{-1})^{(4+\delta)} \quad (3.25)$$

where δ accounts for the dispersion in both the refractive index and the King correction factor. The disadvantage of equation (3.25) is that the contributing factors are not clearly separated, but it can be fitted to the measured cross sections and allows for comparison to the cross sections that are calculated from the refractive indices and depolarisation ratios. The theoretical values were found using a fit on a large number of points computed using equation (3.16) in the range 10 000 cm⁻¹ to 25 000 cm⁻¹. An unfortunate property of equation (3.25) is that the correlation between the two parameters is very strong, leading to unacceptable error margins on the fitted parameters. To find the experimental values in table 3.3, one parameter was held fixed to the theoretical value, while the other was optimised to yield the least squares difference. After two iterations of fitting one variable and holding the other and then interchanging the free and fixed variables, the values no longer changed.

The last column in table 3.3 is the relative mean difference between the measured cross sections and those derived from the refractive index:

$$\Delta_{\text{avg}} = \frac{1}{n} \sum_{i=1}^n \frac{\sigma^{\text{exp}}(\bar{\nu}_i) - \sigma^{\text{refr}}(\bar{\nu}_i)}{\sigma^{\text{exp}}(\bar{\nu}_i)} \quad (3.26)$$

with $\sigma^{\text{exp}}(\bar{\nu}_i)$ our experimental Rayleigh scattering cross section at wavenumber $\bar{\nu}_i$ and $\sigma^{\text{refr}}(\bar{\nu}_i)$ the Rayleigh scattering cross section calculated from equations (3.16) and (3.17) with the appropriate reference data at the same position.

From table 3.3 and figures 3.8 and 3.9 it is clear that the agreement between the measured scattering cross sections in Ar and N₂ and the scattering cross sections calculated from the refractive index and the depolarisation ratio is better than 1%. The agreement for carbon dioxide is less good, at about 4%. A likely source for the deviation is the lack of knowledge about the depolarisation. For carbon dioxide,

3.8 Scattering in CO₂, N₂, Ar, N₂O, CH₄, CO, SF₆ and O₂ at 532 nm

Table 3.4 Scattering cross sections at 18 788.4 cm⁻¹. Figures in parentheses give the 1 σ uncertainty.

Gas	Measured $\sigma_{\tilde{\nu}}$ /10 ⁻²⁷ cm ²		Calculated $\sigma_{\tilde{\nu}}$ /10 ⁻²⁷ cm ²		(n - 1) ^a /10 ⁻⁶	F _k ($\tilde{\nu}$) ^b	Purity of the gas	# ^c
Ar	4.45	(30)	4.56		268	1	99.999%	3
N ₂	5.10	(24)	5.30		284	1.035	99.9%	3
CO	6.19	(40)	6.82		325	1.016	99.997%	3
CO ₂	12.40	(80)	13.29		427	1.145	99.7%	4
CH ₄	12.47	(23)	14.69		481	1.000	99.5%	3
N ₂ O	15.90	(08)	18.19		483	1.225	99.7%	2
SF ₆	32.30	(50)	34.1		733	1.000	99.8%	2

^a At 15 °C and 101 325 Pa. References are given in the text. ^b References are given in the text. ^c Number of pressure ramps

the King correction factor is in the order of 1.15, much larger than the ~1.035 in nitrogen.

3.8 Scattering in CO₂, N₂, Ar, N₂O, CH₄, CO, SF₆ and O₂ at 532 nm

The output of the second harmonic of an unseeded Nd:YAG laser, with a bandwidth of 1 cm⁻¹, was used to measure scattering cross sections at about 532 nm. The measured frequency of this laser was 18 788.4 ± 0.4 cm⁻¹. Three typical pressure ramps were already shown in figure 3.6 on page 32, the results for CO₂, N₂, Ar, N₂O, CH₄, CO and SF₆ are listed in table 3.4, O₂ will be discussed separately in section 3.8.2.

3.8.1 Refractive indices of the remaining gases

The dispersion relations for the King correction factor and the refractive index for argon, nitrogen and carbon dioxide have been discussed in section 3.7.1. For the other gases equations for the refractive index and the depolarisation were found in literature, or fitted to data taken from literature. Each of the gases will be discussed below. Included in figures 3.10 and 3.11 is a graphical representation of the fits used to obtain the dispersion relations. The refractive index depends on the density, and the values given here are scaled to 15 °C and 1013 hPa, or a density of 25.47 × 10¹⁸ cm⁻³.

Carbon monoxide The value of the refractive index of carbon monoxide in the wavelength range 168 nm ≤ λ_{vac} ≤ 288 nm was measured by Smith *et al.* [61]. A

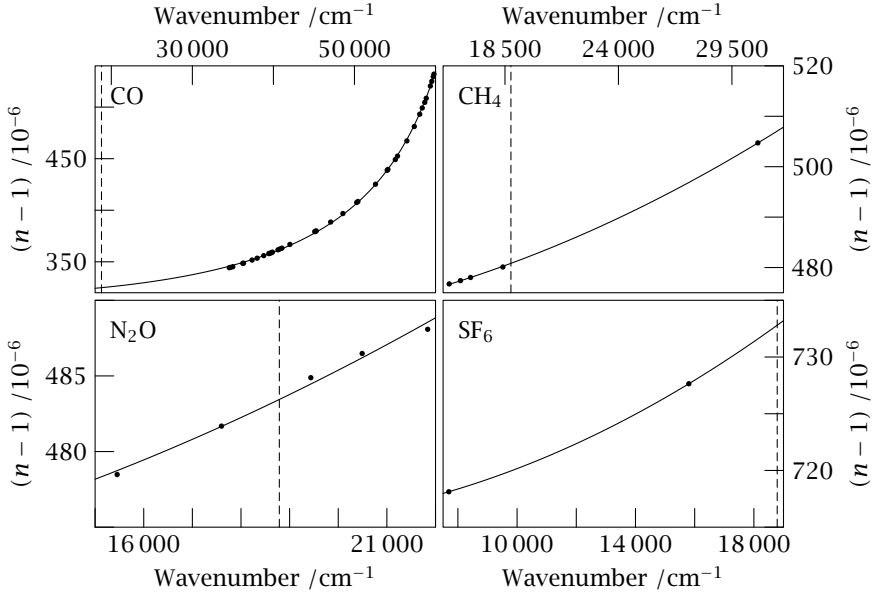


Figure 3.10 Fits of the refractive index against measured data. The dashed vertical lines indicate the frequency of the second harmonic of a Nd:YAG laser. Details are given in the text. references: CO from [61]; CH₄ from [67]; N₂O from [47]; SF₆ from [68].

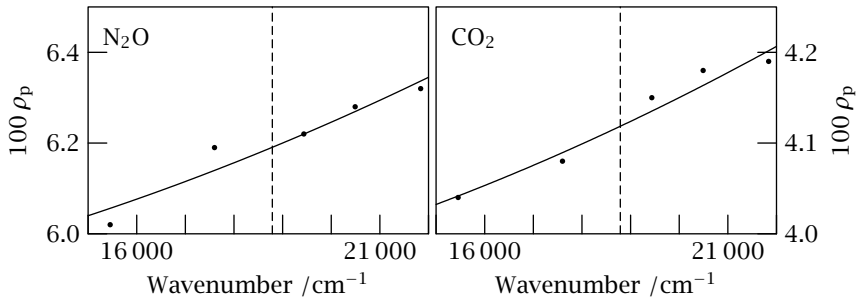


Figure 3.11 The fits of the depolarisation ratio ρ_n against measured data. The dashed vertical lines indicate the frequency of the second harmonic of a Nd:YAG laser. All measurements were taken from Alms et al. [47]. Details are given in the text.

functional form similar to the dispersion relation for nitrogen and argon was fitted to these 38 measurements:

$$(n-1) \times 10^8 = (22\,851 \pm 200) + \frac{(0.456 \pm 0.01) \times 10^{12}}{(71\,427 \pm 200)^2 - (\tilde{\nu}/\text{cm}^{-1})^2} \quad (3.27)$$

Note that the extrapolation to 532 nm is rather far outside the range of the measurements, and that the authors did not fit a dispersion relation to their data. Within the range of the measurements, the accuracy of $n - 1$ is estimated to be $\sim 2\%$.

Because carbon monoxide is a diatomic molecule, its depolarisation is not zero. A single measurement of the depolarisations ratio was found at $\lambda = 632.8$ nm yielding $\rho_p = 0.0048$ [55]. *Ab initio* calculations have shown that the dispersion in the depolarisation ratio can be neglected [60], and therefore the value at the He-Ne laser wavelength was used for the calculations in table 3.4.

Methane Measurements of the polarisability by Hohm [67] were used to fit a dispersion relation for the refractive index. Since the number of data points was much smaller than in the case of carbon monoxide, a simpler function was chosen:

$$(n - 1) \times 10^8 = (46\,662 \pm 13) + (4.02 \pm 0.03) \times 10^{-6} (\bar{\nu}/\text{cm}^{-1})^2 \quad (3.28)$$

The accuracy of this equation is estimated to be better than 4% in the range of the source data. For our 532 nm measurements, an interpolation is needed, with the same 4% assumed accuracy.

Measurements of the polarisability anisotropy were not found, but Bridge and Buckingham [55] performed measurements on CCl₄ and found a depolarisation ρ_p of less than 0.2×10^{-3} , leading to a King correction factor with a negligible difference from unity. The same symmetry is present in CH₄ and in CCl₄ and therefore it is assumed that methane has the same depolarisation.

Nitrous oxide This gas was chosen because of its known high depolarisation ratio. Measurements of the polarisability by Alms *et al.* [47], yielded both the refractive index and the depolarisation ratio.

$$\rho_p = (0.0577 \pm 0.0007) + (11.8 \pm 2) \times 10^{-12} (\bar{\nu}/\text{cm}^{-1})^2 \quad (3.29)$$

$$(n - 1) \times 10^8 = (46\,890 \pm 85) + (4.12 \pm 0.2) \times 10^{-6} (\bar{\nu}/\text{cm}^{-1})^2 \quad (3.30)$$

Sulphur hexafluoride This is the gas with the largest known polarisability. Unfortunately, exactly how large it is only known at two optical frequencies and in the static limit. The two optical frequencies - 633 nm and 1300 nm - from Vukovic *et al.* [68] were used to extract the two constants for the dispersion relation:

$$(n - 1) \times 10^8 = 71\,517 + 4.996 \times 10^{-6} (\bar{\nu}/\text{cm}^{-1})^2 \quad (3.31)$$

Because of the lack of measurements, the quality of this formula is highly uncertain, and its extrapolated value is for qualitative comparison only.

Bridge and Buckingham [55] performed measurements on the depolarisation in SF₆ and found a value for ρ_p of less than 0.2×10^{-3} , leading to a King correction factor with a negligible difference from unity.

Table 3.5 Constants used for the calculation of the refractive index of oxygen with equation (3.32). Taken from reference [48].

Wavelength range	A	B/10 ¹²
$\lambda_{\text{vac}} > 546 \text{ nm}$	21 351.1	21.856 70
$546 \text{ nm} > \lambda_{\text{vac}} > 288 \text{ nm}$	20 564.8	24.808 99
$288 \text{ nm} > \lambda_{\text{vac}} > 221 \text{ nm}$	22 120.4	20.318 76
$221 \text{ nm} > \lambda_{\text{vac}} > 198 \text{ nm}$	23 796.7	16.898 84

3.8.2 Oxygen at 532 nm

One molecule is missing from table 3.4: oxygen. This molecule has several collision-induced absorption features, in which two O₂ molecules absorb a single photon during a collision and both come out of the collision in an excited state. The second harmonic of a Nd:YAG laser coincides with the combined a ¹Δ_g(ν' = 0) + a ¹Δ_g(ν' = 2) - X³Σ_g⁻ + X³Σ_g⁻ transition. A more detailed discussion of the pressure dependent absorption features in oxygen can be found in chapter 4.

Refractive index and King factor for oxygen Bates [48] combines the measurements of several groups into a dispersion relation for oxygen. We give the complete set covering the range down to 198 nm here, as they are needed in chapters 5 and 6:

$$(n - 1) \times 10^8 = A + B / (4.09 \times 10^9 - (\bar{\nu} / \text{cm}^{-1})^2), \quad (3.32)$$

with A and B given in table 3.5.

From Bates [48], we also get an expression for the wavelength dependent King correction factor, based again on a combination of sources, both measurements and *ab initio* calculations.

$$F_k(\bar{\nu}) = 1.096 + 1.385 \times 10^{-11} (\bar{\nu} / \text{cm}^{-1})^2 + 1.448 \times 10^{-20} (\bar{\nu} / \text{cm}^{-1})^4 \quad (3.33)$$

For collision-induced absorptions, the density dependent losses in the cavity not only have a linear component from the Rayleigh scattering, but also components that depend on higher powers of the density. Since only two molecules participate in this absorption feature, the highest power expected here is two, as given in equation (5.2):

$$\beta_{\bar{\nu}}(N) = \beta_{\bar{\nu}}^0 + c \sigma_{\bar{\nu}}^R N + c \alpha^{\text{CIA}} N^2 \quad (5.2)$$

In figure 3.12 the quadratic dependence on the density is clearly visible. The drawn line in the same graph is the prediction of a pressure ramp if the quadratic collision-induced absorption were not present.

The Rayleigh scattering cross section fitted from nine measurements like the one presented in figure 3.12 is $(4.51 \pm 0.33) \times 10^{-27} \text{ cm}^2$. From the dispersion relations of the refractive index and the King correction factor, as given in equation (3.32), a scattering cross section of $2.84 \times 10^{-27} \text{ cm}^2$ can be calculated. The disagreement is probably caused by an incapability to fully separate the linear- and quadratic contributions.

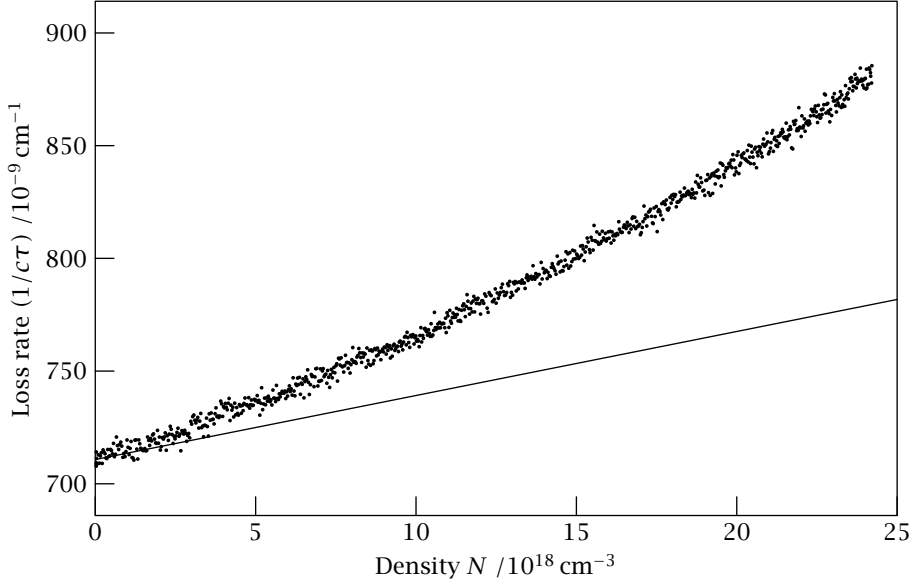


Figure 3.12 Pressure ramp in oxygen. The non-linear behaviour is clearly visible. For comparison, the calculated pressure ramp for oxygen is drawn as well - the straight line, with the slope calculated from refractive index and King correction factor taken from Bates [48].

The quadratic component, the collision-induced absorption cross section α^{CIA} , is fitted to the value $(1.06 \pm 0.11) \times 10^{-46} \text{ cm}^5 \text{ molecule}^{-2}$. Greenblatt *et al.* [69] and Newnham and Ballard [70] have performed measurements of the same absorption and they found a peak-height of the absorption feature of $(1.0 \pm 0.03) \times 10^{-46} \text{ cm}^5 \text{ molecule}^{-2}$ and $(1.23 \pm 0.38) \times 10^{-46} \text{ cm}^5 \text{ molecule}^{-2}$, respectively. The position of the transition indicated in both articles is 532.2 nm or $18\,790 \text{ cm}^{-1}$. The second harmonic of a Nd:YAG laser differs from this by only 2 cm^{-1} , negligible in comparison to the $\sim 10 \text{ nm}$ width (FWHM) of the absorption feature.

3.9 Conclusions

We have measured the Rayleigh scattering cross section in Ar, N₂ and CO₂ over an extended wavelength range. We find an agreement with values calculated from the refractive index and the King correction factor to within 1%, except for CO₂, where the error is about 4%.

The measurements of the Rayleigh scattering cross sections in CO₂, N₂, Ar, N₂O, CH₄, CO and SF₆ at the wavelength of the second harmonic of an Nd:YAG laser can be useful for LIDAR experiments. These measurements show larger deviations with values calculated from the refractive index and the depolarisation ratio.

Experimental verification of Rayleigh extinction

This is in part because the measured refractive indices and depolarisation ratios are incomplete. In O_2 the second harmonic of the Nd:YAG laser coincides with a collision-induced resonance, and the measured strength of this transition agrees with values found in literature.

Collision-induced absorptions in oxygen

A large portion of this thesis deals with oxygen, and some peculiar absorption features of this molecule. One of these features was already mentioned when discussing the scattering measurements in oxygen at 532 nm in section 3.8.2. Here a short introduction into the relevant features of oxygen is given before presenting detailed measurements of these absorptions in oxygen in chapters 5, 6 and 7.

In an absorption spectrum of a gas measured at low density, only the resonances of single molecules are visible. At higher densities, collisions can change the structure of the molecules, and new absorptions may begin to appear. This occurs in many species and combinations of molecules and atoms. Because there are at least two particles involved in such interactions, these absorptions scale with the second and higher powers of the density, depending on the number of particles involved.

The nature of the interaction between the neighbouring particles can vary and some possibilities are shown in figure 4.1. Dispersion forces can displace the electron clouds relative to their nuclei. The displacement depends on the species and the orientation of the molecules, in an asymmetric configuration a dipole will appear, giving rise to additional absorption features. At shorter range the electron clouds repel each other, and a dipole of opposite sign appears, as is shown in figure 4.1*a*. Another means of interaction is shown in figure 4.1*b*. In general a molecule is surrounded by an electric field which can be described by a classical multipole expansion. The resulting electric field can induce a dipole in a nearby molecule. This quadrupole moment is particularly large in N_2 : $4.93 \times 10^{-40} \text{ C m}^2$; the magnitude of the quadrupole moment in O_2 is about a quarter of that, $1.3 \times 10^{-40} \text{ C m}^2$ [71-73]. The last type of interaction - shown in figure 4.1*c* - cannot occur in diatomic molecules. In many polyatomic molecules, large internal dipoles exist that are cancelled by the symmetry of the molecule. A collision can break this symmetry and cause a dipole to appear.

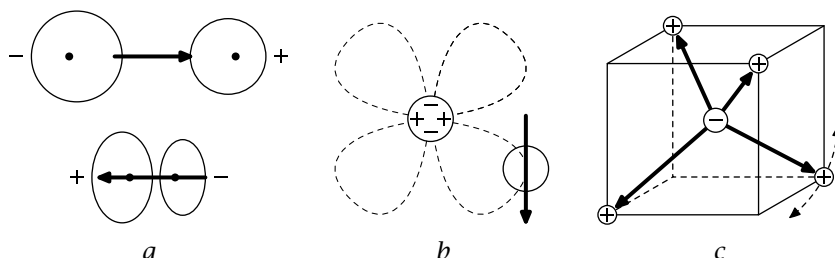


Figure 4.1 Interaction induced dipoles. See text for details, figures taken from reference 74.

In diatomic molecules the inversion symmetry is broken during collisions, as during the collision a four-atom molecule is momentarily formed, where an inversion symmetry does not exist. Transitions where the inversion symmetry - ‘gerade’ or ‘ungerade’ - does not change are forbidden, but this selection rule is easily broken in a collision.

4.1 The peculiar properties of the oxygen molecule

The binding properties of two O(³P) ground state atoms lead to several low-lying electronic states: the X³Σ_g⁻ ground state and the excited states a¹Δ_g and b¹Σ_g⁺, shown in figure 4.2. Transitions between these states are well studied, the b¹Σ_g⁺ ← X³Σ_g⁻ transition is known as the atmospheric system, whereas the a¹Δ_g ← X³Σ_g⁻ transition is known as the infrared system. The first resonances in the atmospheric system, the b¹Σ_g⁺ ← X³Σ_g⁻(0, 0) A-band near 760 nm, and the b¹Σ_g⁺ ← X³Σ_g⁻(1, 0) B-band near 688 nm are well known and clearly visible in the absorption spectrum of the earth’s atmosphere, as is shown in figure 1.4. Besides these three low-lying states, there are several other states that converge to the O(³P) + O(³P) dissociation limit. Three of these states, the A³Σ_u⁺, the c¹Σ_u⁻ and the A’³Δ_u states have a clearly defined potential well, and transitions from the electronic ground state to these states have been observed in the ultraviolet, in the Herzberg I, II and III systems. Besides these states, there are a series of Π states that seem to be repulsive, but are in fact weakly bound at fairly large internuclear separation.

Oxygen is peculiar in that *all* fifteen possible transitions between these six lower states are, in the electric dipole approximation, *forbidden* by quantum selection rules, some of which are connected to the inversion symmetry of the homonuclear molecule. Because the transitions are forbidden, they are weak, and only nine have actually been observed [80]. Minaev and Ågren have shown that some of the selection rules are very sensitive to collisions, and that some transitions may be enhanced by a factor 10⁵ by collisions [81].

Apart from these states, oxygen has states to which transitions from the electronic ground state *are* allowed. The B³Σ_u⁻ state, correlating with the O(³P) + O(¹D) dissociation limit is the lowest state to which such transitions exist. Because the transitions are allowed, the resonances of these Schumann–Runge bands are strong. Their strength is not immediately apparent in the (0, 0) and (1, 0) bands because of the very small Franck–Condon overlap for these bands. According to the HITRAN database [82], the B³Σ_u⁻ ← X³Σ_g⁻(0, 0) transition of the Schumann–Runge band has a band integrated intensity of 230 × 10⁻²⁴ cm⁻¹/(molecule · cm⁻²) - corresponding to a band oscillator strength of *f* = 2.60 × 10⁻¹⁰ [83]. For the oxygen A-band, the b¹Σ_g⁺ ← X³Σ_g⁻(0, 0) transition, an integrated band intensity of 224 × 10⁻²⁴ cm⁻¹/(molecule · cm⁻²) is found - corresponding to *f* = 2.54 × 10⁻¹⁰, all values at 296 K. Both transitions have almost the same strength, but the causes behind their relative strengths are very different. The Schumann–Runge (0, 0) transition has a very small Franck–Condon overlap, as can be qualitatively seen in figure 4.2. Cheung *et al.* [84] have calculated the Franck–Condon factor for this

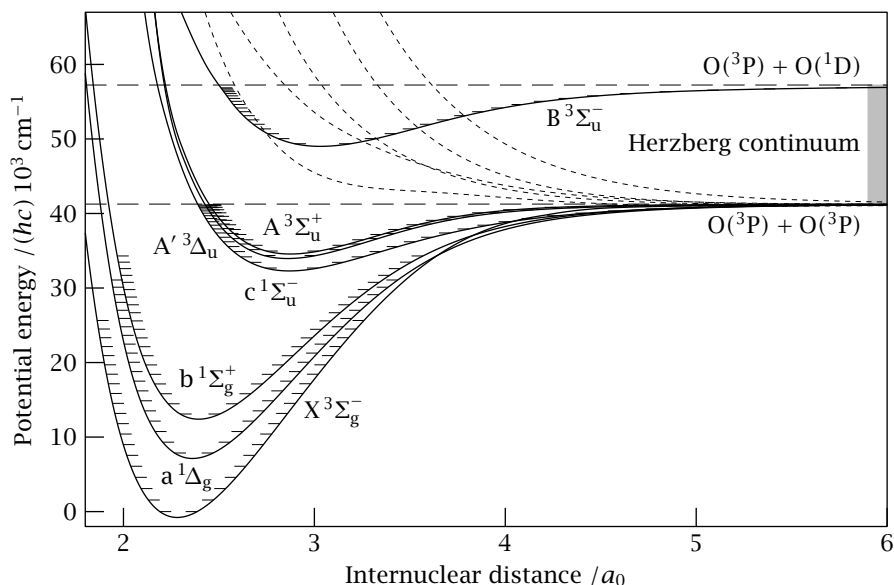


Figure 4.2 A potential diagram of oxygen. The dotted lines are dissociating or very weakly bound Π states. $X^3\Sigma_g^-$ from reference 75, $a^1\Delta_g$ and $b^1\Sigma_g^+$ from reference 76, $B^3\Sigma_u^-$ from reference 77, the other curves calculated by van Vroonhoven [78]. Data and vibrational levels kindly supplied by van Vroonhoven (private communication and reference 79).

transition, and found 3.0×10^{-9} . The oxygen A-band is weak because it is a highly forbidden transition: gerade \rightarrow gerade, $\Sigma^+ \leftrightarrow \Sigma^-$ and singlet \leftrightarrow triplet. The Franck-Condon overlap for this transition is 0.931 [85], and the difference between the two transitions becomes clear: the oxygen A-band is a forbidden transition that makes it a factor $\sim 10^9$ weaker than a fully allowed transition.

Another peculiarity of the oxygen molecule is its triplet ground state. In this configuration, two electrons are unpaired, resulting in spin $S = 1$ for the molecule, and as a consequence spin-spin interactions play an important role in the intermolecular potential for pairs of oxygen molecules; quadrupole interactions shown in figure 4.1(b) hardly play a role in the intermolecular potential [72]. These unpaired electrons cause the oxygen ground state to be very reactive - in some definitions a ground state oxygen molecule is a radical. Spin-spin interactions play an important role in the interaction of oxygen molecules, but this alone is not enough to explain the sensitivity of the oxygen absorption spectrum to collisions. The presence of the low-lying electronically excited states provide a destination for the molecules to be excited to, and because the transitions are forbidden, there is no background caused by the monomer which would normally overpower such a collision-induced absorption.

This is particularly apparent in the Herzberg continuum, see figure 4.2. Trans-

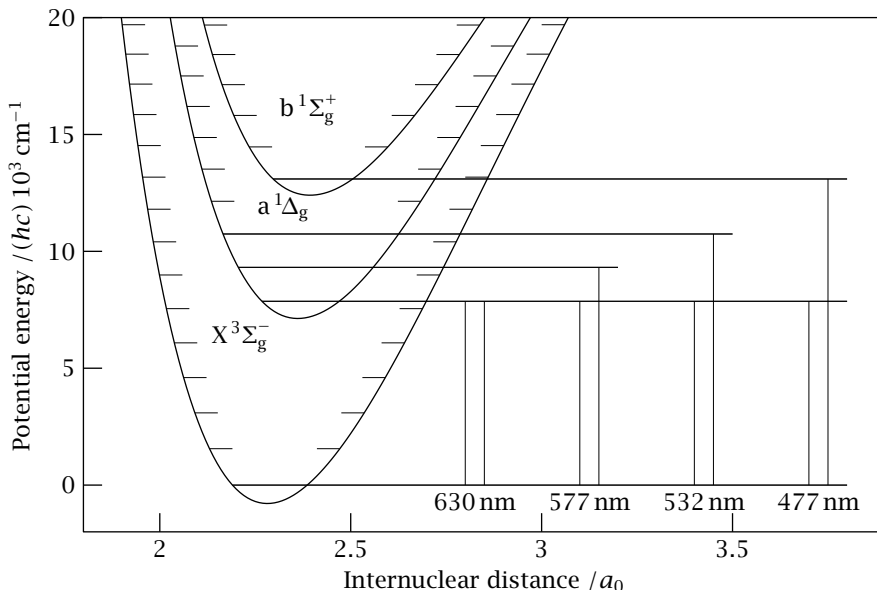


Figure 4.3 Magnification of the lower levels of the $X^3\Sigma_g^-$, $a^1\Delta_g$ and $b^1\Sigma_g^+$ states in oxygen. The combined transitions are indicated, together with the central wavelength for the resonance. This figure uses the same sources as figure 4.2.

itions from the ground state to the Herzberg I, II and III systems - the $A^3\Sigma_u^+$, $c^1\Sigma_u^-$ and $A'^3\Delta_u$ states respectively - are also symmetry forbidden, and so are the transitions to the continuum above the $O(^3P) + O(^3P)$ dissociation limit, that are still coupled to these states. Previous pressure dependent measurements have shown that the extinction coefficient in this continuum is strongly enhanced by collisions [86]. Blake and McCoy [87] have shown that the transition that is enhanced by collisions is the Herzberg III system ($A'^3\Delta_u \leftarrow X^3\Sigma_g^-$). This continuum extends to the region of the Schumann-Runge bands ($B^3\Sigma_u^- \leftarrow X^3\Sigma_g^-$), but measuring the pressure dependent absorption cross section between the lines of the Schumann-Runge bands requires some care. The pressure broadened wings of a Voigt profile also cause N^2 dependent extinction cross section, and therefore care should be taken to avoid the resonance lines. In chapter 7 some measurements on the pressure dependent cross section underlying the Schumann-Runge bands are presented, taken with a light source that has a much narrower bandwidth than the source used in earlier experiments [88], thus making it easier to avoid the resonances.

4.2 Transitions with a double excitation

The collision-induced absorption at 532 nm, shown in figure 3.12, belongs to a second class of collision-induced absorption resonances in oxygen, and is possibly

even more peculiar. This class is formed by absorbing collision pairs, in which a photon is absorbed by the instantaneous complex of two molecules - *not necessarily a bound state*. After absorbing a photon the molecules fly away in an excited state, each one taking part of the absorbed photon energy. The absorption in the Herzberg continuum can be induced by other molecules, such as N₂ or Ar [86], but this second class of collision-induced absorptions can *only* occur in a collision between two O₂ molecules.

These absorption processes are quadratic in the density and there are no underlying features of the monomer molecule. The only linear extinction feature related to oxygen in this wavelength range is the Rayleigh scattering by the molecules, which is essentially linear in the pressure. Calculations on the intermolecular potential of O₄ have shown that there is a binding potential with a well depth of 154 cm⁻¹ [89]. Features of this bound O₄ molecule, or rather a Van der Waals complex, have been observed in a slit-jet expansion [90], but at room temperature these states do not occur.

Throughout the visible and the ultra violet spectral region there are resonances where both molecules are excited. Several experiments in liquid oxygen and in oxygen at high pressure have shown the location of these resonances [69, 91]. In figure 4.3 some of the collision-induced resonances in the visible are indicated in the potential energy diagram. The resonances near 630 nm (15 880 cm⁻¹) and 570 nm (17 308 cm⁻¹) were measured by Naus and Ubachs [92], and measurements of the latter at low temperature are presented in chapter 6, together with further measurement on the transition near 477 nm (20 930 cm⁻¹), which was measured at room temperature before performing measurements at low temperature [93]. Furthermore, a single point on the broad curve of the resonance near 532 nm (18 788 cm⁻¹) is shown in figure 3.12, but no further measurements were performed on this weak transition.

Epifanov and Vigasin [73] used an approach based in statistical mechanics to describe the collisions. In this approach, the phase space is divided into bound molecular pairs, metastable bound pairs and free-free collision pairs. The definition of free-free collision pairs, metastable bound pairs and truly bound pairs is based on the Hamiltonian of the molecular pair, which can be written as

$$\mathcal{H}(q, p) = U + L + E = \Phi + E, \quad (4.1)$$

with $U = U(r, \Omega)$ the multidimensional interaction potential energy surface, L the energy of the rotation around the principal axis of inertia - perpendicular to the intermolecular separation r and E the remaining kinetic energy of the pair - everything is relative to the centre of mass of the pair. The effective potential energy is given by $\Phi(r, \Omega)$, for which a Lennard-Jones potential between each of the atoms in the two molecules plus an additional quadrupole-quadrupole interaction is used. Due to the rotational component L , a potential barrier can occur at intermediate intermolecular separation, leading to molecular pairs that are metastably bound - that is the pair is bound while its potential energy is higher than the potential energy at infinite separation. The calculation of the partition sum and the hard separation of the three regimes is detailed in references [73, 74, 94] beyond the scope of this

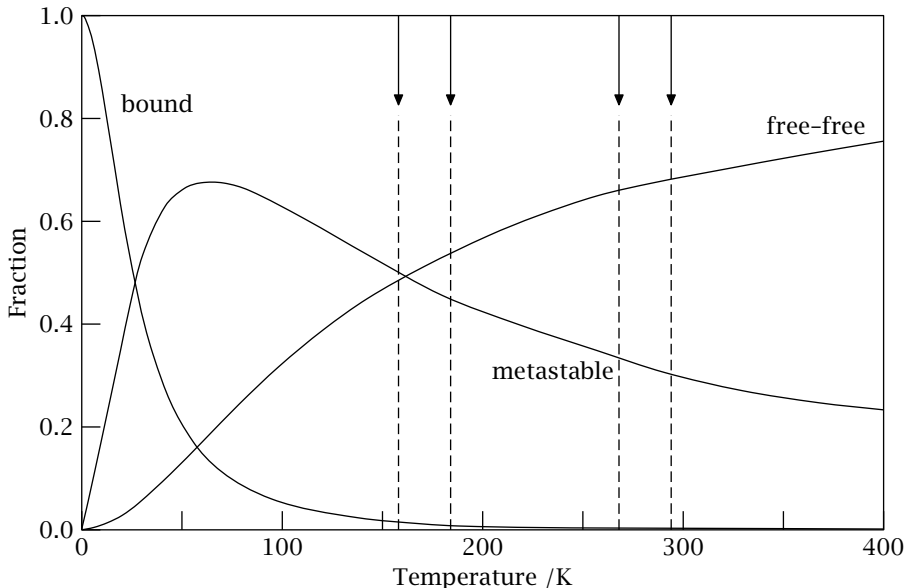


Figure 4.4 Partitioning of the normalised collision-induced absorption intensity in the phase space of oxygen pairs. The dashed lines indicate the four temperatures at which the various measurements in chapters 5 and 6 were taken. Figure kindly provided by Vigasin [74].

thesis, and the result of their calculations is shown in figure 4.4. The results show a temperature dependence of the ratio of bound, metastable and free-free molecular pairs, and a change in the absorption due to collision pairs is likely, following the change of this ratio. The main difference between the three states is the duration of the interaction; the bound dimers support many vibrational states, and have a complicated spectrum with narrow features [90]. The free-free interaction is very short, and the absorption spectrum resulting from this interaction is very broad, in oxygen typically $\sim 200 \text{ cm}^{-1}$, corresponding to an interaction time of $\sim 170 \text{ fs}$. The metastably bound dimers are somewhere in between, leading to the ripple structures observed in previous investigations [95–97].

Some measurements on the temperature dependent absorption cross section of the $(\text{O}_2)_2$ resonances near 630 nm and 580 nm at low pressure were performed by Morville *et al.* [98]. Older measurements at high pressure have also shown a significant change in the line-shape and the absorption cross section of the collision-induced absorption resonances in oxygen [69, 70, 95–97, 99]. These earlier results are the inspirations for our measurements at low temperatures of the resonance near 477 nm.

Cavity ring-down measurement of the O₂-O₂ collision-induced absorption resonance at 477 nm at sub-atmospheric pressures

The O₂-dimer complexes are interesting in molecular physics as well as from an atmospheric perspective. Already in the early studies on liquid oxygen by Ellis and Kneser [100] it was understood that the observed broad resonances were related to simultaneous excitation of two O₂ molecules into a vibronically excited state, as a result of absorption of a single photon. Also the correct assignment in terms of quantum numbers was established as early as 1933 [100], i.e. not long after the advent of molecular quantum mechanics. The resonance at 477 nm, investigated in this study, can be assigned as a simultaneous excitation of two ground state oxygen molecules, one into the a¹Δ_g(ν = 0) state and one into the b¹Σ_g⁺(ν = 0) state.

In the literature on the O₂-O₂ features there has been some dispute on whether the absorption is due to true dimers, i.e. bound Van der Waals complexes, or to pairs of unbound O₂ molecules during a collisional fly-by. Ripple structure, observed by Long and Ewing [101] at low temperatures indicated that bound complexes play a role in the absorption. *Ab initio* calculations predict a well depth of some 150 cm⁻¹ [72], supporting a large number of bound states. Molecular beam scattering studies by Aquilanti *et al.* [102] have unequivocally proven the existence of bound dimers in the ground state. The slit-jet cavity ring-down studies by Campargue *et al.* [103] revealed extremely narrow absorption features of (O₂)₂ in the 630 and 580 nm bands. This proves that Van der Waals complexes, consisting of two a¹Δ_g(ν = 0) excited oxygen molecules, are long-lived on the time-scale of the experiment and are resistant to predissociation. It may be expected that this situation also holds for the a¹Δ_g(ν = 0) + b¹Σ_g⁺(ν = 0) complex and that narrow transitions play a role. However, at room temperature the partition function is dominated by the dissociative continuum of the complex and the phenomenon of collision-induced or free-free absorption will dominate the 477 nm resonance feature of oxygen.

The features associated with O₂-O₂ collisional complexes have attracted much interest in atmospheric physics. Pfeilsticker *et al.* [104] and Solomon *et al.* [105] have evaluated the role of O₄ as an absorber of solar radiation, and concluded that the globally averaged all-sky absorption by collision complexes of oxygen is likely to be between 0.9 and 1.3 W m⁻² (including the N₂-O₂ complex at 1.26 μm). Moreover, in view of its quadratic dependence on pressure, the (O₂)₂ features can be used in remote sensing applications, e.g. in the determination of cloud top heights from satellite data [106]. Recently in situ atmospheric measurements were performed on the UV/vis O₂-O₂ bands yielding the result that absorption profiles are independent of pressure and temperature in the range of relevance

for the atmosphere [99]. Moreover the values for the cross section are consistent with those obtained from high pressure (55 bar) measurements by Greenblatt *et al.* [69]. From the in situ data a value for the formation enthalpy of the bound O₂-O₂ dimers could be deduced. The red (630 nm) and yellow (580 nm) bands are the strongest and would in principle be most useful for remote sensing purposes, if it were not for the fact that these features are overlaid by other absorption features: the O₂ γ -band in the red and a water vapour absorption band in the yellow, which is itself used for satellite data retrieval [107]. The blue feature at 477 nm is easily traceable in atmospheric observation since inferring absorptions from other gasses, e.g. O₃, NO₂ and H₂O are either weak (NO₂ and H₂O) or more identifiable through neighbouring bands. For this reason accurate measurement by an alternative technique is warranted.

Since the early studies in the 1930's in the liquid [100] and gaseous phase [91] a number of laboratory investigations have been performed to determine the absorption strengths of the collision-induced O₂-O₂ features [69, 70, 96, 101, 108]. But in view of the weakness of the bands pressures above or at atmospheric pressure were used to spectrally record the features. In this chapter we report on the use of cavity ring-down (CRD) laser spectroscopic technique applied to the blue (O₂)₂ system at sub-atmospheric pressures as a follow-up to studies on the red and yellow features [92].

5.1 Experiment and results

The experimental setup and methods reflect those used in a previous study [92] except for a change of wavelength. The setup is also described in chapter 1. The interval from 467 nm to 490 nm was covered by running a Quanta-Ray PDL-3 pulsed dye laser system (bandwidth 0.05 cm⁻¹) on Coumarine-480 dye, which was pumped by the 355 nm output of a pulsed Nd:YAG laser. A stable, non-confocal resonator of length 82 cm is formed by mirrors of reflectivity $\geq 99.994\%$ over the investigated frequency range and radius of curvature of 100 cm.

The O₂-O₂ resonance was recorded in discrete steps, whereby for each position the frequency was measured with an Echelle-grating spectrograph, yielding an accuracy of 0.2 cm⁻¹. While keeping the frequency fixed at a certain value, pulsed CRD-transients were measured continuously at a repetition rate of 10 Hz, and oxygen gas was slowly flushed into the CRD-cell. The inlet-flow was controlled by a needle valve, set to cover a time period of 15–20 minutes for full pressurisation up to 1000 hPa. A filter with 0.5 μ m pores was used to extract aerosols from the oxygen gas. Oxygen with a purity of 99.5% was used without further purification. Two typical pressurisation traces are shown in figure 5.1.

The traces consist of about 1100 data points, with each point recorded at a certain pressure, which was measured on-line by a capacitance baratron with an uncertainty of 2 hPa. The pressure and the simultaneously measured temperature were used to calculate the density of the gas, using the ideal gas law, assumed to introduce only a negligible error at these pressures and temperatures. Each data

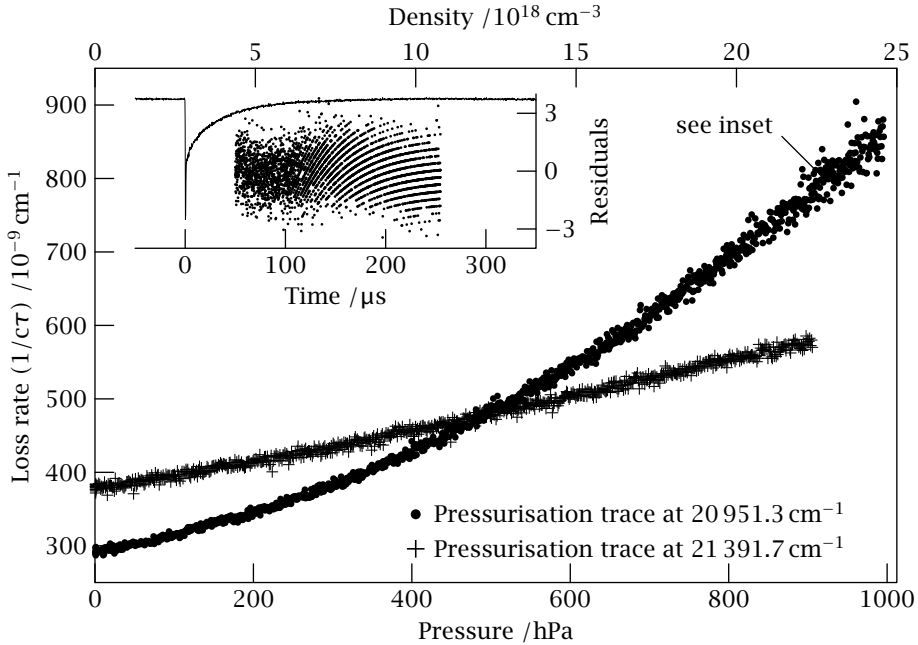


Figure 5.1 Two typical pressurisation traces. The offset β_V^0 on the vertical axis shows the difference in reflectivity between the two wavelengths. The inset shows a ring-down transient (negative peak) and the residuals of the single exponential fit ('fingerprint' pattern). The trace was taken from the pressurisation trace at 20951.3 cm^{-1} , near the end of the trace, the location is indicated with a label. The residuals show clear signs of digitisation noise, especially near the end. The fitting algorithm stops the fitting procedure in that case. This leads to increased noise-levels near the end of the pressurisation trace. Note that the vertical scale of the inset is for the residuals, the ring-down transient itself has no scale.

point in figure 5.1 is a result of a fit to a ring-down transient which is detected by a photomultiplier, digitised by an 8-bits oscilloscope (LeCroy WaveRunner LT 342, used at a sample speed of 20 MS/s) and finally transferred to a computer for further analysis. The loss rate per unit time ($\beta_V(N)$) depends on the density N . This loss rate follows from a non-linear least-squares fit to the recorded transients, using a single exponential function and a determination of the base-line.

As was demonstrated by Naus *et al.* [33] the ring-down transients from a generic pulsed CRD-experiment can be straightforwardly interpreted as an absorption strength or cross section under the condition that the transients are mono-exponential. Then the loss-rate equals:

$$\beta_V(N) = \beta_V^0 + \tilde{\alpha}_{V,\text{tot}}(N) c \quad (5.1)$$

where c is the speed of light and β_V^0 the frequency-dependent loss rate due to the limited and frequency dependent reflectivity of the mirrors. In this work the

procedure was followed to optimise the alignment of the ring-down cavity to produce mono-exponential decays by on-line monitoring of a variance parameter defined in Naus *et al.* [33]. The fitting procedure to yield $\beta_{\bar{\nu}}(N)$ from the observed transients was done in a two-step fashion. In a first step a non-weighted fit was performed, while in a second step, a weighted fit-procedure was followed, using the weights derived in the first round of fitting. As discussed in reference [33] in this way the information content of the CRD-transients is optimally used and a true statistical uncertainty to the result can be given. In the wavelength domain from 467 nm to 490 nm 53 pressurisation curves were measured, two of which are displayed in figure 5.1. These curves can be parametrised by three parameters

$$\beta_{\bar{\nu}}(N) = \beta_{\bar{\nu}}^0 + c \sigma_{\bar{\nu}}^R N + c \alpha^{\text{CIA}} N^2 \quad (5.2)$$

The linear component $\sigma_{\bar{\nu}}^R$ in equation (5.2) is the Rayleigh scattering cross-section. This value can be computed from the refractive index and the depolarisation ratio, as discussed in chapter 3. The refractive indices and King correction factor were taken from Bates [48]. We kept $\sigma_{\bar{\nu}}^R$ fixed to the computed value of the Rayleigh scattering cross-section in our least-squares fit of the remaining two parameters $\beta_{\bar{\nu}}^0$ and α^{CIA} to the measured pressure-ramp. The $\beta_{\bar{\nu}}^0$ parameter gives information about the reflectivity of the mirrors. The α^{CIA} parameter, representing the quadratic pressure dependence is plotted in figure 5.2 for the 467 nm to 490 nm interval. The function used to create the fit shown in the same figure, is discussed in section 5.2.

During the analysis of our data we verified that the $\sigma_{\bar{\nu}}^R$ parameter, if calculated from the fit, had the expected value. The values we found were very close, but the correlation between $\sigma_{\bar{\nu}}^R$ and α^{CIA} was relatively high. We therefore used a fit with a calculated and fixed value of $\sigma_{\bar{\nu}}^R$, which gave us a better estimate of the O₂-O₂ contribution.

5.2 The model-equation for the absorption profile

The O₂-O₂ absorption is complex and involves two multi-dimensional potential energy surfaces. There is no simple expression that describes the profile; all possible contributions from bound and free states on the ground and excited state potential surfaces have to be included, weighted by their proper Boltzmann population factors and kinetic energies. A simplified, empirical picture that turns out to describe the O₂-O₂ collision-induced transition fairly well, was suggested by Watanabe and Welsh [109] and later used by several others [96, 97, 110]. We will follow this treatment.

Individual collision-induced transitions exhibit a Boltzmann relation between the intensities in the high- and low-frequency wings. One could consider this as if the kinetic energy of the molecules that take part in the absorption can compensate a shortage of energy in the photon to make the double transition. This may be represented by:

$$\frac{\mathcal{A}(\bar{\nu}_c - \Delta\bar{\nu})}{\mathcal{A}(\bar{\nu}_c + \Delta\bar{\nu})} = \exp\left(-\frac{hc\Delta\bar{\nu}}{k_B T}\right), \quad (5.3)$$

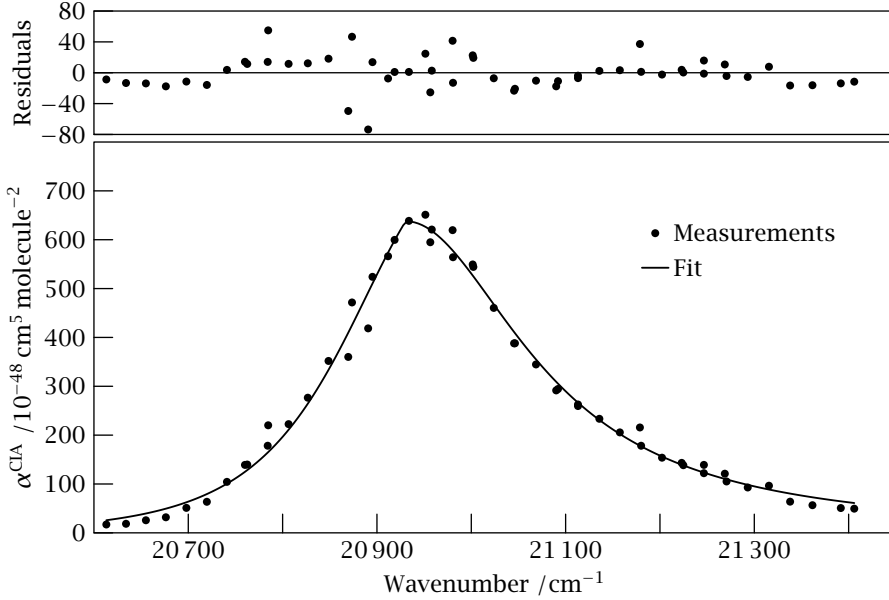


Figure 5.2 The absorption profile. The bottom panel shows the measured points (dots) and the fit to these points (drawn line). The function used for the fit is discussed in section 5.2. The top panel shows the difference between the fit and the measured points. The unit and multiplication factor on both vertical axes are the same.

with \mathcal{A} the intensity of the absorption, $\bar{\nu}_c$ the central position of the absorption, $\Delta\bar{\nu} = \bar{\nu} - \bar{\nu}_c$, T the temperature of the gas, and h , c and k_B are Planck's constant, the speed of light and Boltzmann's constant respectively.

Equation (5.3) gives the ratio between the high- and low-frequency wings, but it does not specify the shape of the line itself. The basic profile is a Lorentzian profile, where the lower energy side is modified to reflect the fraction of molecules which have an energy high enough to contribute to the absorption. This leads to:

$$\mathcal{A} = \frac{a (\Gamma/2)^2}{(\Delta\bar{\nu})^2 + (\Gamma/2)^2} \times \begin{cases} 1 & \text{if } \Delta\bar{\nu} > 0 \\ \exp\left(\frac{hc\Delta\bar{\nu}}{k_B T}\right) & \text{if } \Delta\bar{\nu} \leq 0 \end{cases} \quad (5.4)$$

where a and Γ are parameters for the amplitude and the width of the absorption, respectively.

The model equation as given by equation (5.4) is fitted to the intensities α^{CIA} , found in the first fit of the loss-rate during a pressure ramp to equation (5.2). The results of this final fit are shown in table 5.1. To find the integrated cross-section, the model equation is integrated, using the parameters found in the fit. The final width parameter one would designate as the FWHM width is of course different, since the cut-off by the exponent is not included in Γ . The cut-off by the Boltzmann factor also causes our results to be shifted slightly towards lower

Table 5.1 Parameters found using equation (5.4) as the model function and a least-squares fit. The indicated errors are 1 σ values. A graphical representation of the data and the fit-result can be seen in figure 5.2.

Parameter	Measured value
$\tilde{\nu}_c$	$20\,930.5 \pm 1.6 \text{ cm}^{-1}$
λ_c	$477.77 \pm 0.07 \text{ nm}$
FWHM	$241 \pm 7 \text{ cm}^{-1}$
FWHM	$5.50 \pm 0.01 \text{ nm}$
Γ	$309 \pm 7 \text{ cm}^{-1}$
a	$(6.38 \pm 0.16) \times 10^{-46} \text{ cm}^5 \text{ molecule}^{-2}$
$\int \mathcal{A} d\tilde{\nu}$	$(2.18 \pm 0.04) \times 10^{-43} \text{ cm}^4 \text{ molecule}^{-2}$

Table 5.2 A comparison between literature values and our results.

Reference	$\int_{\text{Band}} \mathcal{A} d\tilde{\nu}$ / $10^{-43} \text{ cm}^4 \text{ molecule}^{-2}$	Peak Height / $10^{-46} \text{ cm}^5 \text{ molecule}^{-2}$
Tabisz [97]	2.09	7.3
Blickensderfer [95]	2.4	7.1
McKellar [96]	2.20	6.4
Greenblatt [69]	— ^a	6.3 ± 0.6
Newnham [70]	2.483 ± 0.048	8.34 ± 0.83
This work [93]	2.18 ± 0.04	6.38 ± 0.16

Reference	Width / cm^{-1}	Density or pressure
Tabisz [97]	200	100 – 300 amagat ^b
Blickensderfer [95]	300 ± 40	2 – 4 amagat ^b
McKellar [96]	— ^a	4.4 amagat ^b
Greenblatt [69]	270	1 – 55 bar
Newnham [70]	— ^a	1000 hPa
This work [93]	241 ± 7	0–1000 hPa

^a Not indicated. ^b Dimensionless density, relative to the density at 273.15 K and 101 325 Pa.

frequencies, with respect to previous studies. This is a direct consequence of the treatment of the absorption profile as asymmetric. A comparison with previous studies is included in table 5.2. The results of McKellar *et al.* [96], initially in terms of a cross-section divided by the frequency of the transition, were recalculated in the presently used units for comparison. When comparing all results collected in table 5.2 there appears a consistency with a gradual trend toward higher accuracy in the obtained band parameters, with the exception however of the values reported by Newnham and Ballard [70], that deviate substantially, particularly in view of the stated error margins.

5.3 Conclusion

Cavity ring-down spectroscopy has been used to determine the band parameters of the $a^1\Delta_g(v=0) + b^1\Sigma_g^+(v=0) \leftarrow X^3\Sigma_g^-(v=0) + X^3\Sigma_g^-(v=0)$ absorption feature in a pressure range from 0 to 1000 hPa. In the analysis it was verified that the collision-induced absorption of oxygen is a quadratic function of pressure, and Rayleigh extinction was taken into account. For the final results the Rayleigh cross-section was set to the computed value, but earlier analysis showed that the linear component in the loss-rate - see equation (5.2) - compares favourably to the value calculated from the refractive index. Care has been taken to align the ring-down cavity correctly, so that the decay transient can be interpreted as a single exponential decay, yielding correct cross-sections.

The presently derived parameters describing the blue $(O_2)_2$ feature are consistent with the body of previously obtained values, while the accuracy is better. The data may be of use for data retrieval by satellite instruments spectrally covering the blue range, such as in the case of the Ozone Monitoring Instrument (OMI), which is currently under development.

Acknowledgements

The present work was supported by the Space Research Organization Netherlands (SRON) with a grant (EO-036) in the Earth Observation program. The authors wish to thank I. Aben (SRON), P.F. Levelt (KNMI, OMI-project), G. Tabisz (Univ. Manitoba), A. McKellar (NRC Ottawa) and L. Frommhold (Univ. Texas) for fruitful discussions.

Cavity ring-down measurement of the O₂-O₂ collision-induced absorption resonances at 477 nm and 577 nm at low temperatures and sub-atmospheric pressures

The oxygen molecule has a series of collision-induced absorption resonances, as described in chapter 4. These resonances involve molecular pairs that jointly absorb a single photon, and *both* make a transition to an electronically excited state. These resonances were discovered in the study of liquid oxygen in 1933 by Ellis and Kneser [100], and even then - just a few years after the advent of molecular quantum mechanics - the resonances were understood as bi-molecular absorptions and the assignment in terms of quantum numbers could be performed. The resonance at 477 nm is assigned as an excitation of two oxygen ground-state molecules, one into the a¹Δ_g (ν = 0) state, and one into the b¹Σ_g⁺ (ν = 0) state. Measurements on this resonance were presented already in chapter 5 and it is also the main focus of this chapter. The production of 477 nm light requires the use of short-lived blue dyes, and therefore another resonance near 577 nm was chosen for testing the measurement procedure at low temperatures. This resonance can be assigned to the transition a¹Δ_g (ν = 0) + a¹Δ_g (ν = 1) ← X³Σ_g⁻ + X³Σ_g⁻. The room-temperature measurements of this resonance were performed before by Naus and Ubachs [92].

Whether the two molecules form a bound Van der Waals complex, or are essentially unbound and absorb the photon during a collisional fly-by, has been a matter of discussion in the literature. Measurements at low temperatures by Long and Ewing [101] show some ripple structure - indicating that bound (O₂)₂ states play a role in the absorption resonance. *Ab initio* calculations show that the O₂-dimer has a potential well with a depth of 150 cm⁻¹ [72], supporting many vibrational states. Measurements by Biennier *et al.* [90] in a slit-jet expansion have shown many narrow resonances in the oxygen dimer. However, these measurements were done at *very* low temperatures, much lower than our experiments. We do not expect to observe ripple structure in our spectra, not even as low as 159 K.

The (O₂)₂ resonance at 477 nm is of particular interest for the OMI instrument. Space based instruments look down on the atmosphere, and from spectral measurements performed by these instruments the concentration of specific molecules in the atmosphere can be derived, if the absorption spectra of these molecules are known. Since the spatial resolution of these satellites is limited, clouds can obscure part of the field of view, and thus change the optical properties and the average path over which the light travels through the atmosphere. These clouds can be detected by using a known and constant absorber, most commonly the atmospheric bands of oxygen (b¹Σ_g⁺ ← X³Σ_g⁻). However these absorptions are in the red and near infra-red, whereas the OMI instrument has a spectral range of 270-500 nm,

sufficient for detecting ozone, but cloud detection using the atmospheric oxygen bands becomes impossible. Acarreta and De Haan [13] have investigated a cloud detection algorithm using the O₂-O₂ resonance at 477 nm. An error in the band integrated collision-induced absorption cross section of this resonance of 10%, leads on average to an error in the estimate of the cloud pressure of 100 hPa. This in turn leads to a 1 % error in the ozone densities, although observations where the pixel is fully covered by high clouds may have larger errors due to the uncertainty in the O₂-O₂ absorption resonance. Since the scatter in the literature values on the band integrated collision-induced absorption cross section is already 15%, the uncertainty in the determined ozone column densities from OMI for cloudy measurements is dominated by the uncertainty in the O₂-O₂ resonance; the cloud-free uncertainty is 1.2%, mostly due to instrument noise. The present investigation was performed to provide the integrated cross section and shape function of the O₂-O₂ resonance at 477 nm as a function of the temperature for analysis of OMI spectra, and ultimately to improve the accuracy in the retrieval of ozone column densities.

6.1 Description of the setup and the experimental procedure

The measurements presented here are a continuation of the previous measurements at room temperature presented in chapter 5. Using the pressure-ramp technique, described previously, collision-induced absorption cross sections are measured at lowered temperatures. In this pressure-ramp method, the cell is evacuated and then slowly filled with oxygen, while the loss-rate in the cavity and the pressure in the cell are continuously recorded. The loss in the cavity contains three terms: an offset representing the frequency dependent reflectivity of the mirrors, a linear contribution is associated with Rayleigh scattering, and a quadratic contribution representing the bi-molecular or collision-induced absorption:

$$\beta_{\bar{\nu}}(N)/c = \beta_{\bar{\nu}}^0/c + \sigma_{\bar{\nu}}^R N + \alpha_{\bar{\nu}}^{\text{CIA}} N^2, \quad (6.1)$$

with c the speed of light, $\sigma_{\bar{\nu}}^R$ the Rayleigh scattering cross section and $\alpha_{\bar{\nu}}^{\text{CIA}}$ the collision-induced absorption cross section.

The mirrors used for these experiments are from Research Electro Optics, with a diameter of 25.4 mm diameter, and a reflectivity of $\mathcal{R} \approx 99.99\%$, leading to a decay time of $\sim 30 \mu\text{s}$ in the $d = 80 \text{ cm}$ cavity. Beforehand there were some concerns as to what would happen with the reflectivity of the mirrors when bringing the temperature down. Since the reflective layer of the mirrors are made from a multi-layer dielectric coating, using interference to produce the very high reflectivity, a change in temperature might cause a change in the thickness of the layers, causing a change in the reflectivity. These concerns were invalidated in the experiment, as no dramatic change in $\beta_{\bar{\nu}}^0$, and hence the reflectivity between room temperature and the lowest temperature was observed. There was some change in alignment, but the correct alignment was quickly recovered once the temperature had stabilised.

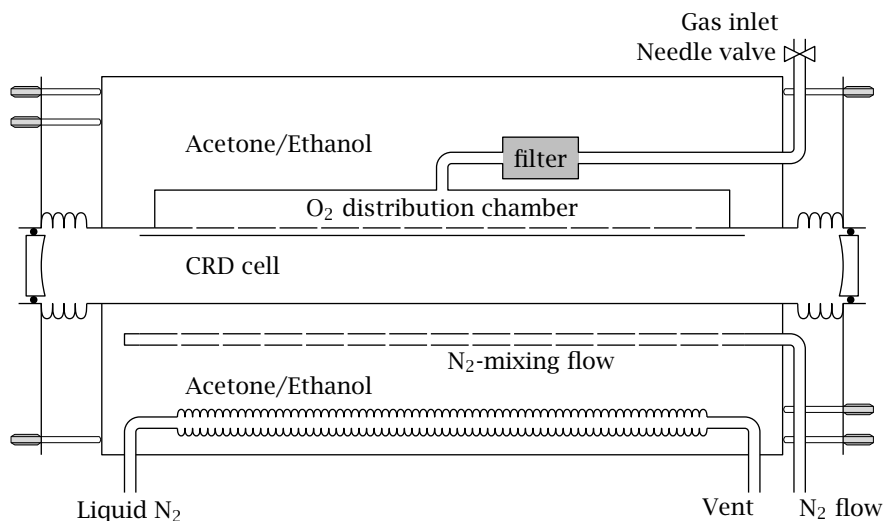


Figure 6.1 Schematic overview of the cooled CRD cell. The nitrogen-mixing flow through the coolant starts below the CRD cell, the pressure meter and vacuum-pump (not in the figure) are attached to the top of the cell to minimise the heat load. The micrometer screws and bellows between the mirrors and the rest of the cell allow for alignment. Dry N_2 is blown against the outside of the mirrors to keep them free from ice (not shown in the figure).

6.1.1 Reaching and maintaining low temperatures

The following description is illustrated in figure 6.1, while a detailed drawing of the cell and the mirror-mount can be found in figure 2.7 on page 19. The low temperatures are obtained by submerging the CRD cell in a low-temperature bath, consisting of a liquid and its ice. Two chemicals were used for this: acetone – which has a freezing point of -94.8°C , or 178.4 K and ethanol – which freezes at -114.1°C , or 159 K [111].

After the cell is aligned and evacuated, the outer volume is filled with the coolant, to a level well above the actual ring-down cell. A polystyrene vessel is connected to the tube leading to the bellow, and this vessel is filled with liquid nitrogen. Gravity pulls the liquid nitrogen through the bellow, cooling down the surrounding coolant, and eventually the entire setup will be cooled down. For these coolants, the density will increase when the temperature is lowered, and since the bellow is located at the same height as the ring-down cell, the cold coolant will sink to the bottom of the outer volume. To ensure a homogeneous temperature throughout the cell, and to bring the coldest coolant into contact with the ring-down cell, nitrogen gas is blown through a tube with a series of holes located at the bottom of the outer volume. To reduce the heat-load of this gas-flow, the nitrogen gas is cooled down by leading it through another container with liquid nitrogen. The bubbles will mix the liquid and bring the temperature of the whole cell down to the freezing point of the coolant.

Reaching the freezing point of acetone and ethanol takes between four and five hours, and after this time the temperature can be maintained by keeping a steady flow of liquid nitrogen through the bellow. Note that at this low temperature, the coolant is frozen solid around the bellow, and liquid nitrogen will reach the vent. To limit the flow, a tube is attached to the vent to create some resistance for the flow.

As with the measurements at room temperature, the collision-induced absorption cross section is determined with the pressure-ramp method. To fill the cell with oxygen at a predetermined low temperature, the gas is purged through a sintered stainless steel filter with 7 μm pores, located inside the outer tube and submerged in the coolant. This filter provides a large contact surface area, and after purging the temperature of the gas is assumed to be the same as that of the fluid. Because this thermalisation filter is inaccessible from the outside, a second filter with 0.5 μm pores is used outside the cell to filter aerosols from the oxygen and prevent contamination of the thermalisation filter. Apart from this filter, the oxygen with a specified purity of 99.999%, is used without further treatment. The rate of flow is controlled by a needle valve. The temperature of the coolant is measured by a thermocouple - type K, (Ni + 10% Cr) against (Ni + 2% Al + 2% Mn + 1% Si) [111] - with the tip placed close to the oxygen thermalisation filter.

The pressure sensor is placed on top of the cell, in an effort to reduce the heat load on the system. The capacitance baratron for the range 0 hPa to 1333 hPa with an uncertainty of 2 hPa is temperature compensated, not temperature controlled. The temperature of a controlled baratron is stabilised at 45 °C, and this would have led to an unacceptably high heat load on the ring-down cell. To compute the density from the measured temperature and pressure the Van der Waals equation of state is used, with parameters taken from the CRC handbook of chemistry and physics [111].

The measurements at 268 K were performed with a different cooling technique; here a chiller filled with anti-freeze was used to bring down the temperature. The filler opening and the bubble-flow pipes were used as the connection points for the hoses, and the chilled liquid was pumped around by the chiller. The lowest temperature we were able to reach with the chiller was 268 K (-5 °C).

6.2 Measurements

The raw measurements are analysed in several steps and the results as presented here already have undergone a number of preparing steps. In the first step an exponential decay function (2.15) is fitted to the ring-down transients, as shortly discussed before in chapter 2. The decay rate which follows from this fit is used in the next step to measure and store the loss in the cavity as a function of the gas-density in the ring-down cell. Four typical density-ramp traces of the low temperature measurements on the 477 nm resonance are shown in figure 6.2. The strange 'bump' below densities of $15 \times 10^{18} \text{ cm}^{-3}$ is reproducible and unexplained. In the measurements at 184K, the feature is clearly visible in the wings of the

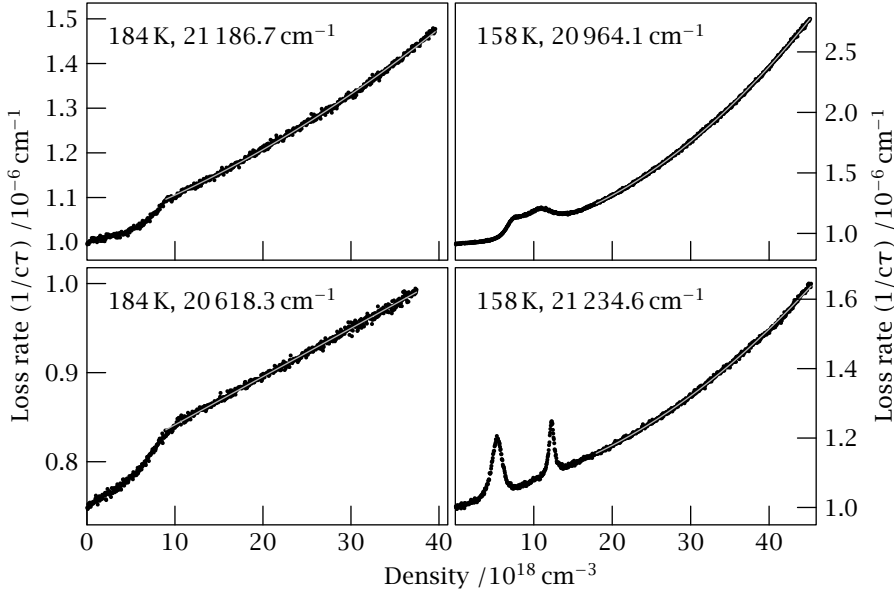


Figure 6.2 Two of the pressure ramps taken at 184 K, and two at 159 K, taken at the indicated positions in the 477 nm resonance. The ‘bumps’ are clearly visible in the coldest measurements, and a clear bend is visible in the other measurements. The grey lines are the fit of a polynomial to the data to extract the collision-induced absorption cross section.

resonance, but it probably is present as well in the measurements near the peak of the resonance. To obtain correct results for the collision-induced absorption cross section, all data below a density of $9 \times 10^{18} \text{ cm}^{-3}$ is ignored in the fitting procedure. The unexpected features in the measurements at 159 K were even more pronounced, and even showed what seem to be resonance peaks. For these measurements all data below $18 \times 10^{18} \text{ cm}^{-3}$ is ignored. The measured decay-rates beyond these densities are well described by a quadratic function.

The density-ramps are fitted over the appropriate range with a second order polynomial, as given by equation (6.1). The linear term in this fit is kept at the value of the Rayleigh scattering cross section σ_V^R , which is calculated from the refractive index and King correction factor, as was described before in chapter 3. The coefficient of the quadratic term is the collision-induced absorption cross section. In figures 6.3 and 6.4 the final results of the measurements on the 477 nm and the 577 nm resonances of $\text{O}_2\text{-O}_2$ collision-induced absorptions are shown. The measurements at 294 K on the 577 nm resonance are taken from Naus and Ubachs [92], while the room-temperature measurements on the 477 nm resonance were already presented in chapter 5.

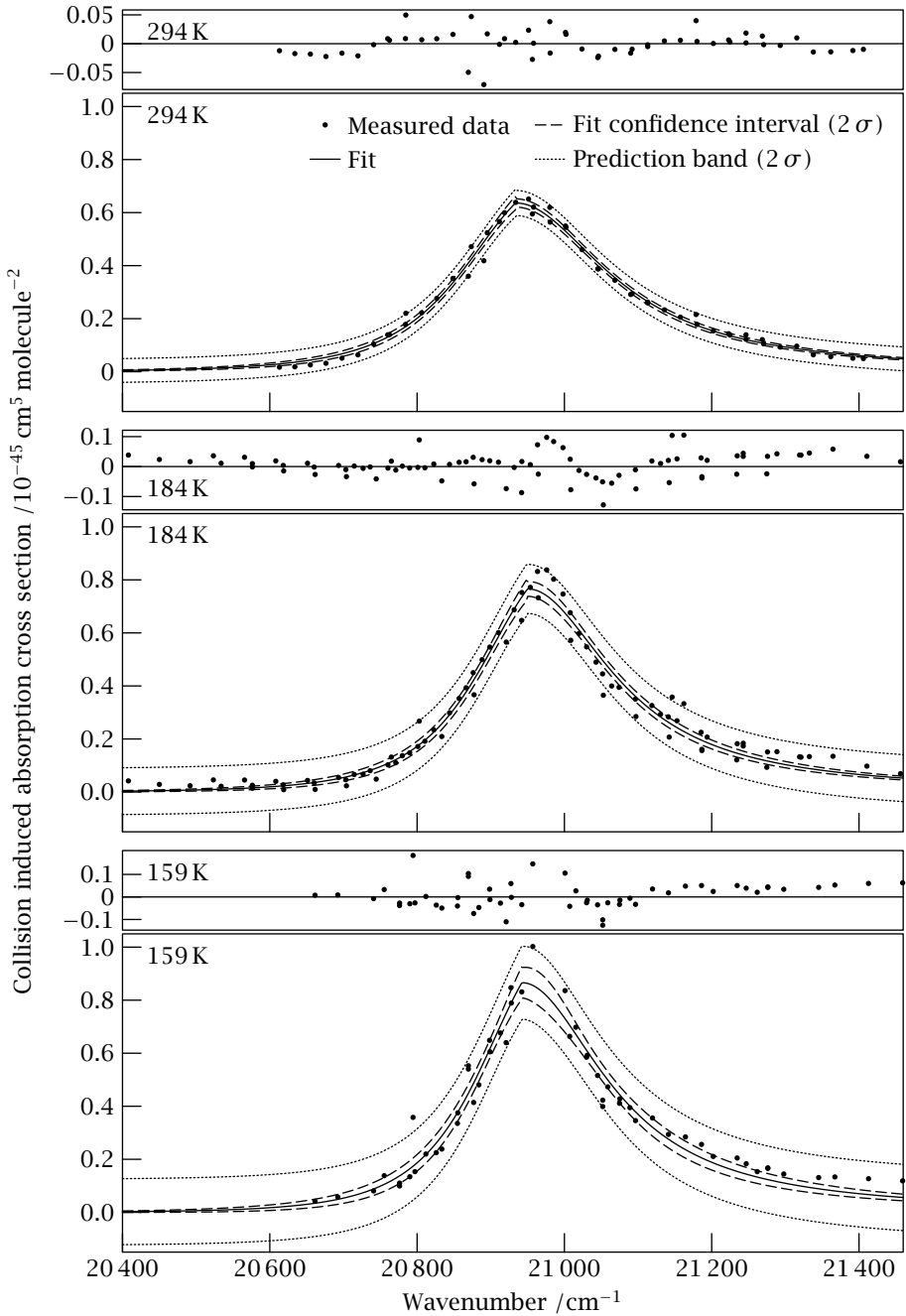


Figure 6.3 The absorption profile of the O₂-O₂ feature near 477 nm at 294 K, 184 K and 159 K. Further details are given in section 6.3.

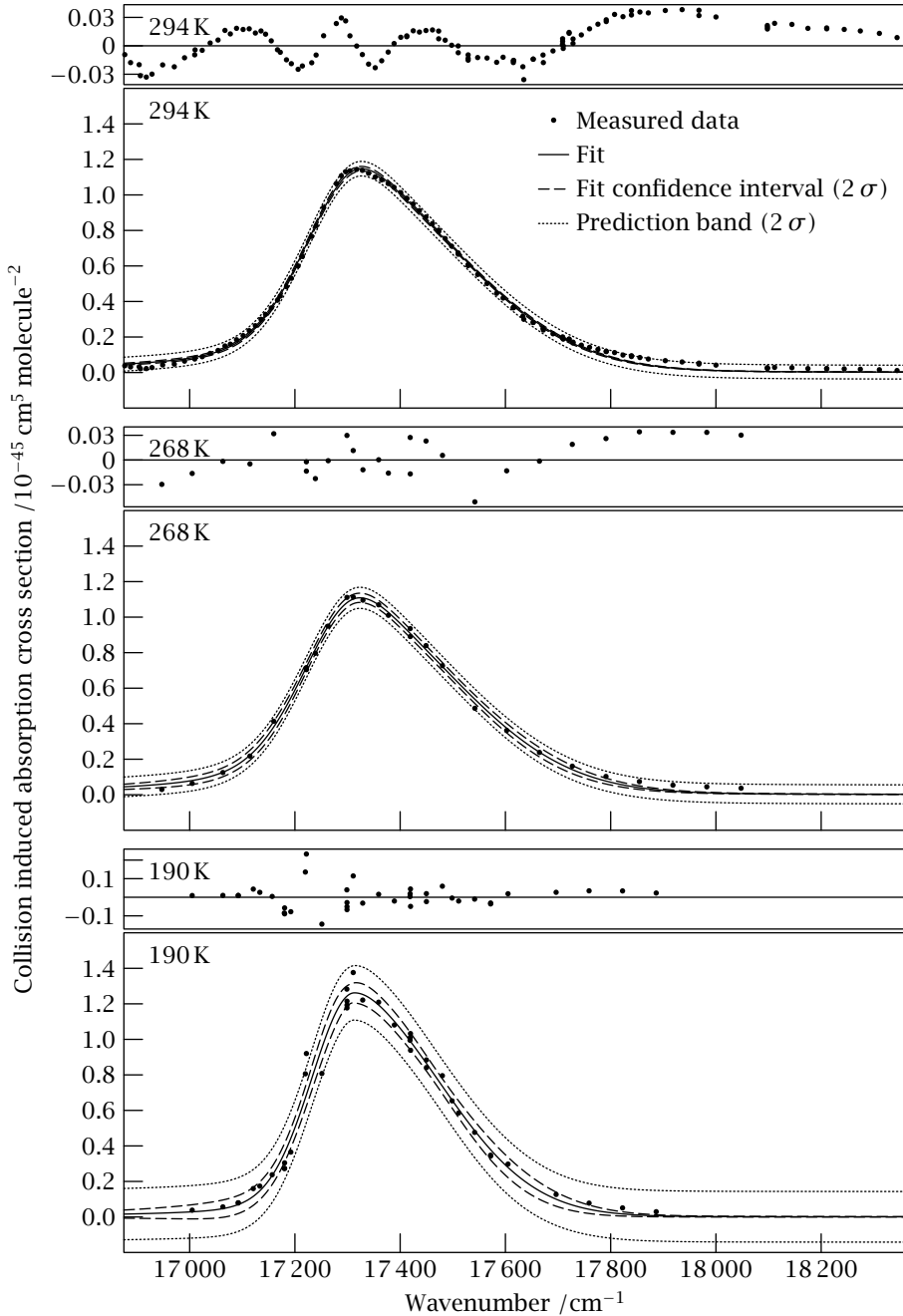


Figure 6.4 The absorption profile of the $\text{O}_2\text{-O}_2$ feature near 577 nm at 294 K, 268 K and 190 K. Further details are given in section 6.3.

6.3 Analysis of the data

In figures 6.3 and 6.4 the fit of a model function to the measured data are shown. The solid lines are the least squares best fit results. The dashed lines in these figures indicate the confidence interval for the fit-result at the 2σ (95.4%) level. This means that if the experiments were repeated, 95.4% of the experiment sets would yield a fit that falls within the indicated interval. The dotted lines indicate the confidence interval for the prediction at the same level, indicating that 95.4% of the measured points should fall within the indicated band. These confidence intervals were found using algorithms described in [112].

As before, we do not have a good theoretical description of the collision-induced absorption profile, and empirical model functions are used to describe the shape function of the resonance feature. The purpose of representing the shape of the resonance in terms of an analytical representation is twofold: The shape function is used to derive an integrated collision-induced absorption cross section $-\int_{-\infty}^{\infty} \alpha_{\tilde{\nu}}^{\text{CIA}} d\tilde{\nu}$, and the shape function can be used in retrieval procedures for the determination of column densities and profiles of species in the earth's atmosphere. The shape function we use to describe the 477 nm resonance was first suggested by Watanabe and Welsh [109], and used by several others [96, 97, 110]. In this empirical model, the high- and low-frequency wings of the transition show a Boltzmann related ratio:

$$\frac{\mathcal{A}(\tilde{\nu}_c - \Delta\tilde{\nu})}{\mathcal{A}(\tilde{\nu}_c + \Delta\tilde{\nu})} = \exp\left(-\frac{hc\Delta\tilde{\nu}}{k_B T_{\text{eff}}}\right), \quad (6.2)$$

with \mathcal{A} the intensity of the absorption, $\tilde{\nu}_c$ the central position of the absorption resonance, $\Delta\tilde{\nu} = \tilde{\nu} - \tilde{\nu}_c$, T_{eff} the effective temperature of the gas and h , c and k_B are Planck's constant, the speed of light and Boltzmann's constant respectively. This model assumes that part of the energy needed to make the transition can come from the kinetic energy of the collision partners. This is admittedly a very simplistic model, that does not take into account collision parameters such as the relative angles at which the two molecules approach each other.

Equation (6.2) does not specify the shape to the profile, just the high- and low-frequency ratios. The shape we have picked for the underlying line is the Lorentz profile, leading to:

$$\mathcal{A}(\tilde{\nu}) = \frac{a(\Gamma/2)^2}{(\Delta\tilde{\nu})^2 + (\Gamma/2)^2} \times \begin{cases} 1 & \text{if } \Delta\tilde{\nu} > 0 \\ \exp\left(\frac{hc\Delta\tilde{\nu}}{k_B T_{\text{eff}}}\right) & \text{if } \Delta\tilde{\nu} \leq 0 \end{cases} \quad (6.3)$$

where a and Γ are parameters for the amplitude and the width of the absorption, respectively. In chapter 5 the temperature in equation (6.3) was taken to be the temperature at which the measurements were performed. Especially at lower temperatures, this leads to unsatisfactory fit results. The effective temperature T_{eff} is now a fit-parameter and it is adjusted to give the best fit to the data. The real temperature of the measurement is *not* found from the fitting procedure.

During the analysis of the data, it became apparent that the model given by (6.3) works well for the description of the 477 nm resonance, but when it is applied

to the 577 nm resonance, large residuals and a very poor fit is found. Following the analysis of Naus and Ubachs [92], a skewed Voigt profile was used to describe the shape of the 577 nm resonance. Note that this profile is even *more* empirical than (6.3). The skewed Voigt profile is approximated by a linear combination of a Gauss and a Lorentz profile:

$$\mathcal{V}(\tilde{\nu}) = (1 - b) \left\{ \frac{a}{1 + \left(4(\tilde{\nu} - \tilde{\nu}_c)^2 / \Gamma^2 \xi^2 \right)} \right\} + b \left\{ a \exp \left[-4 \ln 2 \left(\frac{\tilde{\nu} - \tilde{\nu}_c}{\Gamma \xi} \right)^2 \right] \right\} \quad (6.4)$$

with

$$\xi = \begin{cases} 1 - 2 \arctan(\text{skew factor}) / \pi & \text{if } \tilde{\nu} < \tilde{\nu}_c \\ 1 + 2 \arctan(\text{skew factor}) / \pi & \text{if } \tilde{\nu} \geq \tilde{\nu}_c \end{cases}$$

The parameters found in the fitting procedure are shown in tables 6.1 and 6.2. The two sets use different model functions, and therefore have different parameters in their respective tables. The indicated errors are found from the fitting procedure. An attempt was made to propagate the error estimates found from the fit of the ring-down transients to the model function given in (2.15), but the resulting errors were unrealistically small. The currently indicated errors assume that the errors in all measured points are equal and that the model function is accurate. In that case χ^2 scaling is possible, and the resulting errors are reported. The indicated accuracy on the band integrated absorption cross section is found by applying a Gaussian variation with the indicated standard deviation to the parameters describing the model function and taking the standard deviation of the resulting distribution of integrated cross sections.

Table 6.1 Parameters describing the absorption profile of the O₂-O₂ feature near 477 nm at various temperatures. The parameters were found using equation (6.3) as the model function and a least-squares fit. The indicated errors are 1 σ values. A graphical representation of the data and the fit-result can be seen in figure 6.3.

Temperature /K	294 ^a	184	159
Coolant	None	Acetone	Ethanol
$\tilde{\nu}_c$ /cm ⁻¹	20934 ± 3.5	20950 ± 4.3	20942 ± 6.2
λ_c /nm	477.69 ± 0.08	477.33 ± 0.10	477.50 ± 0.14
FWHM /cm ⁻¹	241 ± 9	220 ± 12	211 ± 21
FWHM /nm	5.5 ± 0.2	5.0 ± 0.3	4.8 ± 0.5
Γ /cm ⁻¹	302 ± 9	276 ± 12	272 ± 21
a /10 ⁻⁴⁸ cm ⁵ molecule ⁻²	636 ± 8	766 ± 14	866 ± 28
T_{eff} /K	335 ± 43	303 ± 50	257 ± 58
$\int \mathcal{A}(\tilde{\nu}) d\tilde{\nu}$ /10 ⁻⁴² cm ⁴ molecule ⁻²	0.221 ± 0.007	0.243 ± 0.012	0.264 ± 0.021

^a Measurements taken from Sneep and Ubachs [93], see chapter 5.

Table 6.2 Parameters describing the absorption profile of the O₂-O₂ feature near 577 nm at various temperatures. The parameters were found using equation (6.4) as the model function and a least-squares fit. The indicated errors are 1 σ values. A graphical representation of the data and the fit-result can be seen in figure 6.4.

Temperature /K	294 ^a	268	190
Coolant	None	Chiller	Acetone
$\bar{\nu}_c$ /cm ⁻¹	17325.8 ± 1.7	17322.8 ± 3.5	17313 ± 7
λ_c /nm	577.17 ± 0.06	577.3 ± 0.1	577.6 ± 0.2
FWHM /cm ⁻¹	346.5 ± 3.0	342.3 ± 7.1	290 ± 10
FWHM /nm	11.5 ± 0.1	11.3 ± 0.2	9.6 ± 0.3
Γ /cm ⁻¹	318 ± 3	317 ± 7	257 ± 10
a /10 ⁻⁴⁵ cm ⁵ molecule ⁻²	1.15 ± 0.01	1.11 ± 0.03	1.26 ± 0.05
skew factor	-0.64 ± 0.02	-0.60 ± 0.05	-0.65 ± 0.11
b	0.782 ± 0.012	0.784 ± 0.034	0.91 ± 0.06
$\int \mathcal{V}(\bar{\nu}) d\bar{\nu}$ /10 ⁻⁴² cm ⁴ molecule ⁻²	0.470 ± 0.006	0.447 ± 0.013	0.406 ± 0.024

^a Measurements taken from Naus and Ubachs [92].

6.4 Discussion and comparison with other measurements

The measurements at low temperature on both the 477 nm and the 577 nm resonance show that the width of the resonance is increases with temperature, while at the same time the peak-height decreases. There are some previous studies on the temperature behaviour of both resonances, but unfortunately not all authors extract the same parameters from their data. What data is available on the 477 nm resonance is shown in figure 6.5. The increase of the width, and the decrease of the peak-height with temperature is consistent with other measurements, although the measurements by Newnham and Ballard [70] on this resonance seem to be out of line with the other available measurements, with their peak absorption at 283 K higher than the other measurements, and a reduction of the peak-height - within their measurements - at a lower temperature.

The behaviour of the band-integrated collision-induced absorption cross section which follows from our measurements - a slow decrease of the band-integrated intensity with temperature - clearly contradicts the results from Newnham and Ballard [70], who observe a significant increase when raising the temperature. Especially their measurement at 223 K falls far below an interpolation of our results. Further measurements at intermediate temperatures are welcome to verify the behaviour between 184 K and 280 K.

More measurements are available on the 577 nm resonance, and in figure 6.6 a comparative overview of some of the available measurements is given. For this resonance the measurements seem to agree; The width of the resonance increases with temperature, the height decreases with temperature and for the range of temperatures we have available the band integrated collision-induced absorption cross section is increasing with rising temperature. It is unfortunate that Morville *et*

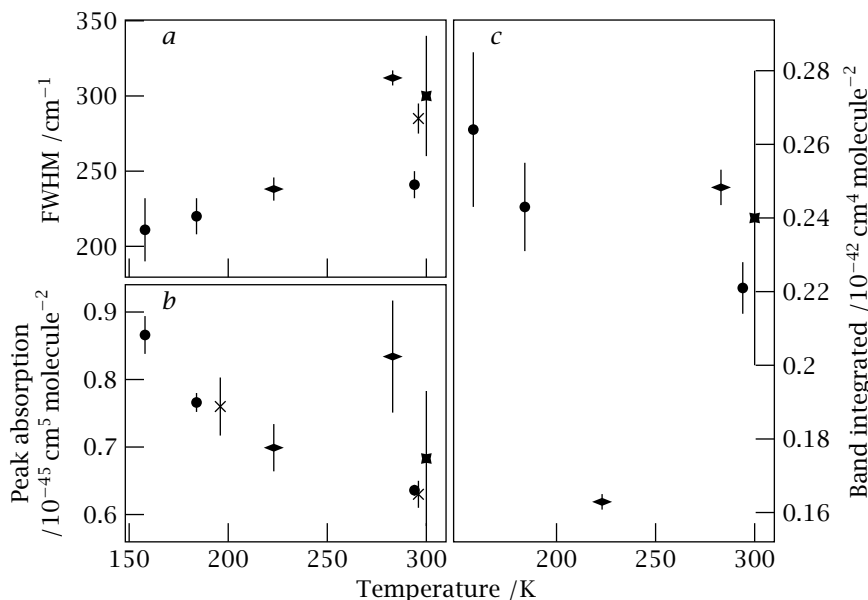


Figure 6.5 Temperature dependence for several parameters of the 477 nm O_2 - O_2 resonance. The width is shown in figure 6.5a, the height in figure 6.5b and the band integrated intensity in figure 6.5c. The vertical bars indicate the 1σ confidence level on each point. Sources: \blacksquare — Blickensderfer and Ewing [95] \times — Greenblatt *et al.* [69] \blacklozenge — Newnham and Ballard [70] \bullet — This work.

al. [98] did not determine the band integrated absorption cross section from their measurements, as a rough estimate from a multiplication of height and width, seems to indicate that at lower temperatures this parameter starts to increase again. There are measurements by Ewing *et al.* [95, 101] at 87.3 K, far below any recent measurements, and for scaling reasons those results were not added to figures 6.5 and 6.6. These measurements indicate that the band integrated absorption cross section increases again at 87.3 K. The trends towards a narrower feature and a higher peak absorption continues, according to these measurements.

Although the behaviour at low temperature of the two resonances studied here is similar, there is one noteworthy difference: the band integrated collision-induced absorption cross section of the 477 nm resonance decreases slowly with increasing temperature, while the 577 nm resonance is increasing over the range of temperatures we have available. Vigasin has demonstrated a simplified model to explain the behaviour of the band integrated collision-induced absorption in the oxygen fundamental as a function of temperature [113]. The relation he finds has a shallow minimum for the oxygen fundamental at around 270 K. Although the nature of this resonance without an electronic transition and the resonances studied here are different, some general remarks regarding the behaviour observed in the 477 nm and 577 nm resonances can be made following the analysis by Vigasin. Depending

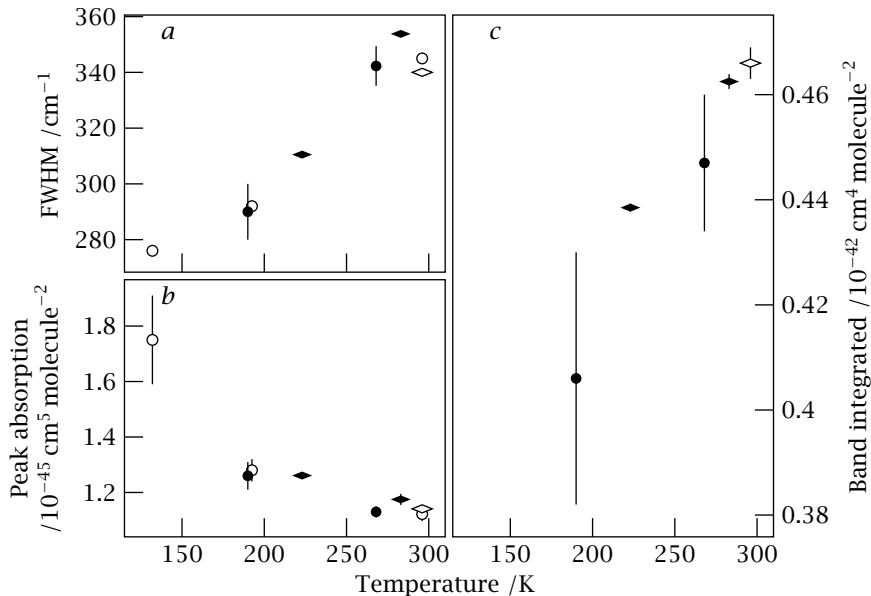


Figure 6.6 Temperature dependence several parameters of the 577 nm O₂-O₂ resonance. The width is shown in figure 6.6a, the height in figure 6.6b and the band integrated intensity in figure 6.6c. The vertical bars indicate the 1 σ confidence level on each point. Sources: \circ — Morville et al. [98] \blacktriangleright — Newnham and Ballard [70] \diamond — Naus and Ubachs [92] \bullet — This work.

on the temperature range, only one section may have been observed; the integrated cross section of the 577 nm resonance may well increase at lower temperatures. At the same time, the measurements on the 477 nm resonance do not exclude a minimum between the room-temperature measurements and the first cold measurement.

These measurements on the 477 nm resonance were inspired by the the needs of OMI. In the GOME spectrum shown in figure 1.4, the O₂-O₂ resonance near 477 nm is clearly visible. For a correct determination of the cloud pressure in the observations the O₂-O₂ cross section is needed at atmospherically relevant temperatures. Since the absorption only takes place in colliding oxygen molecules, the effective absorption quickly diminishes with altitude; air above 5 km hardly contributes to the observed absorption. To cover all of the troposphere, including situation where the ground temperature is much lower, measurements down to 215 K are requested by the OMI group. Everything below this temperature is interesting from a molecular physics point of view.

Measurements at intermediate temperatures in the 220 K to 270 K range are still needed. Currently measurements are performed using a water and anti-freeze mixture. This combination normally protects against freezing down to about -40 °C. Unfortunately this is a mixture and as such it does not have a fixed freezing point,

it has a freezing trajectory instead, and that makes it more difficult to maintain a constant temperature.

6.5 Conclusions

The measurements on the 477 nm resonance show an increase of the width and a decrease of the peak height with increasing temperature. Our measured seem to be consistent with literature values, although the measurements by Newnham and Ballard [70] on the peak height contradict our findings. The behaviour of the band integrated absorption cross section, or even its value at room temperature, is less clear. In our measurements a slight decrease with rising temperatures can be seen, although there are not enough points to deduce a functional relation. The measurements by Newnham and Ballard [70] at 223 K are in direct contradiction to our results, and further research is warranted to fully understand the behaviour at low temperatures.

Our measurements on the 577 nm resonance are in line with results reported in literature: the resonance gets narrower and the peak height grows when the temperature is lowered. For the range 190 K to 300 K, the band integrated collision indicate absorption cross section seems to decrease with decreasing temperature, although further measurements at low temperature are needed to fully characterise the behaviour under these circumstances.

For both resonances investigated here, the peak height increases when the temperature is lowered. This is consistent with most earlier measurements [70, 95, 98, 101], although Newnham and Ballard contradict our findings for the 477 nm resonance. This result also lends support to the division of phase space into tightly bound states, metastable states and free pairs as calculated by Vigasin *et al.* [73, 94]. The consideration behind the division of phase space were discussed before in chapter 4, and the results of these calculations are shown in figure 4.4. The free pairs dominate the collision-induced absorption at room temperature, while at the temperatures reached in the experiments the tightly bound dimers do not play a significant role. The increase in the peak absorption cross section is attributed to the increase of the metastable pair states when the temperature is lowered.

Acknowledgements

In the comparison with older measurements, raw data measured by Newnham *et al.* under ESA Contract 11340/95/NL/CN was used to extract some features of the 577 nm and 477 nm O₂-O₂ resonances that were not present in their paper [70].

Deep-ultraviolet cavity ring-down spectroscopy

Since the discovery of cavity ring-down (CRD) spectroscopy [18], this sensitive optical technique has been applied for direct absorption monitoring in a wide wavelength range, spanning from the infrared range at $10\ \mu\text{m}$ [114], via the entire visible domain, to the UV. This broadness of wavelength range makes the technique applicable for gas phase studies in cells, molecular beam jets, etching plasma reactors, laser photolysis, flames, furnaces and heat pipe ovens, hollow cathode discharges, slit nozzle discharges, and diamond depositing flames. For an overview of such applications we refer to Berden *et al.* [20]. At the UV end of the spectrum CRDS was applied to detect the methyl radical in a hot filament reactor at $\lambda = 216\ \text{nm}$ [115], while detection of ammonia molecules via an absorption feature at $\lambda = 205\ \text{nm}$ [32] marks the cutting edge of CRDS at short wavelengths. The sensitivity in CRDS is known to scale with $(1 - \mathcal{R})$, with \mathcal{R} the reflectivity of the mirrors forming the cavity; lower reflectivities decrease the number of round trips and therewith the time span over which an optical decay transient can be recorded. Production of mirrors that are highly reflective deeper into the UV becomes gradually more difficult. State-of-the-art reflectivities measure $\mathcal{R} \approx 96\text{--}98\%$ at deep-UV wavelengths. Here we report on extending the domain of CRDS beyond the $200\ \text{nm}$ threshold into the deep-ultraviolet, with applications to extinction, Rayleigh scattering, resonant absorption and predissociative decay of small gas phase molecules.

Wavelength tunable laser pulses in the range $197\text{--}204\ \text{nm}$ are produced via a Ti:Sapphire (Ti:S) oscillator cavity, which is pumped by the green output of a seeded Nd:YAG *Q*-switched laser and injection-seeded by the continuous wave (cw) output of a Ti:S laser. The oscillator cavity contains no other elements than the Ti:S crystal; its cavity length is stabilised to the mode of the cw laser via the Hänsch-Couillaud locking scheme. On pumping at $\sim 10\ \text{mJ/pulse}$ it delivers near-infrared pulses at $1\ \text{mJ/pulse}$, at a duration of $15\ \text{ns}$ to $24\ \text{ns}$ and a $10\ \text{Hz}$ repetition rate and in a bandwidth of $\sim 50\ \text{MHz}$. The pulse duration is physically determined by the rate of stimulated emission in Ti:S and is a function of pump power and of the reflectivity of the output coupler, which for these measurements was taken at $\sim 90\%$. Although we demonstrated that it is possible to amplify the output pulses to a level of $30\ \text{mJ/pulse}$ in a bow-tie amplifier, for the present application this option is not employed. The effective fourth harmonic of these pulses are produced via consecutive frequency-mixing processes in three β -barium-borate (BBO) crystals cut at the appropriate angles for type-I phase matching. Finally tunable narrow-band deep-UV pulses of $\sim 0.1\ \mu\text{J}$ to $30\ \mu\text{J}$ of $8\ \text{ns}$ duration and a bandwidth of $100\ \text{MHz}$ are produced that are implemented in the CRDS setup. The bandwidth in the UV was calibrated by resonantly probing Yb atoms in a highly collimated beam by laser induced fluorescence.

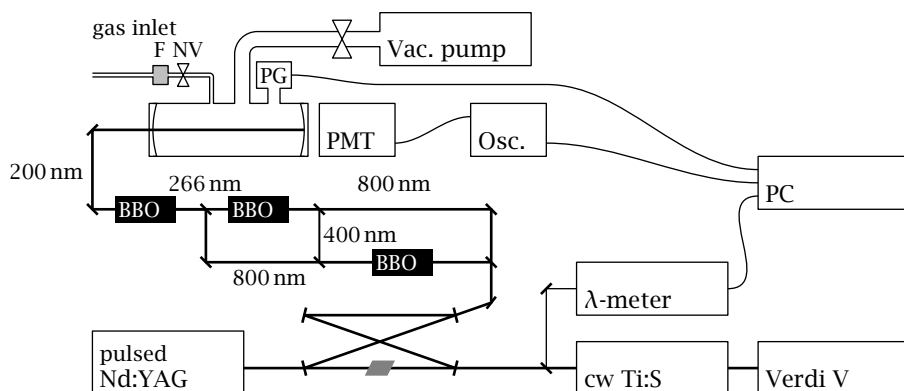


Figure 7.1 Layout of the laser system delivering tunable wavelength Fourier Transform limited pulses in the range 197–204 nm and the CRD-setup. Osc. — digital storage oscilloscope PMT — photomultiplier tube PG — pressure gauge NV — needle valve F — aerosol filter.

The CRD configuration is composed of two highly reflective mirrors (Rocky Mountain Instruments; 1 m radius of curvature) forming a sealed cavity of length 86 cm. The measured ring-down time in an evacuated cavity is 90–100 ns, corresponding to a reflectivity of 97%. The cell can be evacuated by a turbomolecular pump and gas can be inserted via a needle valve, allowing for controlled pressure ramp scans as in previous CRD measurements in the visible domain [36]. The experimental configuration, including the laser setup and the ring-down geometry, is schematically depicted in figure 7.1.

Using a digital oscilloscope (LeCroy WaveRunner LT 342, with a sampling speed of 500 MSamples/s) CRDS decay transients are recorded and transferred to a computer for further analysis. The decay time ($1/e$) of an empty cell is on the order of 100 ns, while in extinction measurements transients as short as 40 ns are allowed by the analysis software. The laser pulse duration of 8 ns might produce a systematic deviation on the estimated decay rate, but calculation of the convolution integral shows that the resulting deviation is less than 1% if decay transients of $4.5 \tau_{\text{cav}}$ are used, as long as the fitting starts after the end of the pulse. The narrow bandwidth of the laser has the advantage that slit function effects causing underestimation of the absolute extinction cross section in CRDS [32, 33] do not play a role in the present investigation, not even when narrow lines are recorded; the line-width of 100 MHz is much lower than the Doppler broadening of 3.3 GHz for O_2 at these short wavelengths. For an interpretation of ring-down transients in terms of a Beer's law exponential extinction one must ensure that the measured transients follow a mono-exponential decay function. For this reason an alignment procedure was applied that optimises the cavity for minimum deviation from a single exponential decay [33].

By use of a pressure-ramp method [36], extinction cross sections of various gases

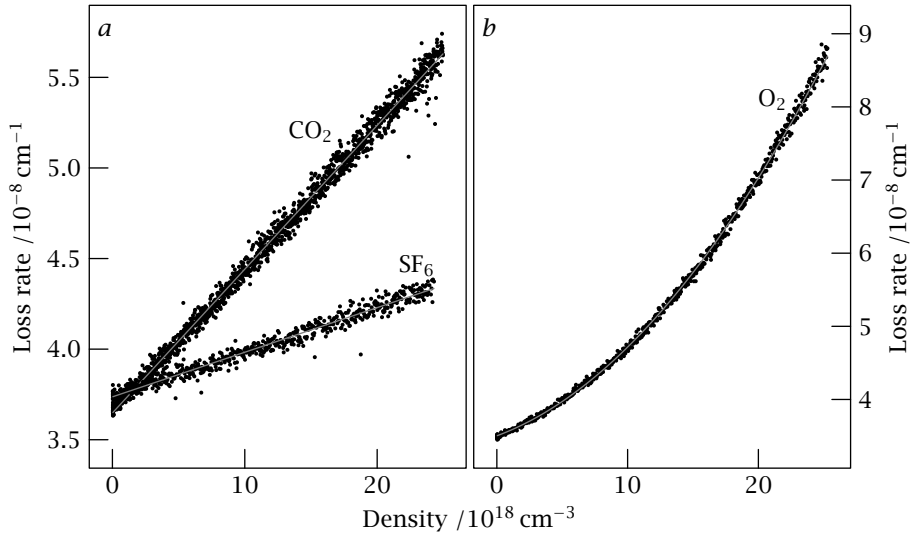


Figure 7.2 Extinction measurements as a function of density. *a* — CO₂ and SF₆ exhibit a linear density dependence at 197.99 nm. *b* — O₂ shows a quadratic pressure dependence, at 197.039 nm (50 751.4 cm⁻¹).

can be determined. To avoid turbulence, the cell is slowly filled to 1 bar over a time span of ~ 15 min and during this time the cavity decay rate is continuously monitored. Three of these pressure scans are displayed in figure 7.2 for various gases. Each data point corresponds to the decay rate of an average over five measured decay transients. Since the loss rate corresponds to $\beta_0 + N\sigma_\lambda$, where β_0 is the empty cavity loss rate; the slope in the pressure curves is proportional to the extinction cross section σ_λ of the gas. Small differences in the intercepts in figure 7.2 may occur, representing small differences in the mirror reflectivity as a result of cleaning of the mirrors and the time-interval over which the cell has been evacuated. From fits to this slope the extinction cross sections are derived, results of which are listed in table 7.1 for CO₂ and SF₆. All measurements are performed at room temperature and the ideal gas law was applied to convert pressure into density N . The indicated errors follow from a weighted average over several pressure scans, with the weights derived from the fit of the decay transient and a subsequent fit on the pressure ramp, and are 1σ estimates.

The observed extinction in carbon dioxide is largest. Previously Ogawa [116] investigated the absorption cross section of CO₂ in the region 172–216 nm and found a weak but complicated band structure, superimposed on an underlying dissociative continuum. Our measurement of an extinction cross section at one specific wavelength ($\lambda = 197.99$ nm) agrees with the lower resolution value; future work employing the narrow bandwidth and the tunability of the deep-UV laser system may help to unravel the onset of band structures in CO₂ at 198 nm [116].

For SF₆ the extinction is expected to be determined by Rayleigh scattering. In SF₆

Table 7.1 The extinction cross sections for SF₆ and CO₂ at 197.99 nm (50 507.96 cm⁻¹). The results are an average over several pressure scans.

Gas	Measured cross section /10 ⁻²⁵ cm ² molecule ⁻¹	Literature value /10 ⁻²⁵ cm ² molecule ⁻¹
CO ₂	86 ± 10	70 ^a
SF ₆	26 ± 4	23.6 ^b

^a From an interpolation between values given in reference 116. ^b Refractive index extrapolated from two points [68]; King factor assumed to be unity [55].

only two measurements of a refractive index exist in the visible and near infrared range [68]. Conversion into a cross section via $\sigma_{\lambda}^R = 8\pi^3(n_{\lambda}^2 - 1)^2 F_K(\lambda) / (3N^2\lambda^4)$, and assuming King factors $F_K(\lambda)$ of this spherical molecule to equal unity, gives good agreement even in extrapolation to the deep UV.

The continuous tunability of the novel deep-UV laser system was employed in the recording of spectra of three Schumann-Runge bands in O₂, parts of which are displayed in figure 7.3. This is, to our knowledge, the first time that the triplet-spin structure in the weakest (0, 0) band is resolved. These measurements allow for an accurate determination of the spin-state dependent effects in the spectra and in the predissociation rates in the B³Σ_u⁻, v' = 0 state, as well as an assessment of the competition between fluorescent decay and predissociation. The combination of the narrow-bandwidth laser and the generation of exact fourth harmonics yields a highly accurate determination of deep-UV resonance frequencies; frequencies of the seed-light were measured with an ATOS LM007 wavelength meter with an accuracy of 0.002 cm⁻¹, which was verified during the measurement campaign by calibration on I₂ hyperfine lines measured in saturation. Line positions of single resolved lines in the (0, 0) Schumann-Runge band could be determined within 0.02 cm⁻¹. From a fit to the rotational structure involving 64 lines accurate values of the fine structure constants were determined. The spin-spin interaction constant λ is determined to be (1.642 ± 0.007) cm⁻¹, the centrifugal distortion of this constant λ_D is (-4.0 ± 1.1) × 10⁻⁴ cm⁻¹ and the spin-rotation constant γ is (-3.11 ± 0.03) × 10⁻² cm⁻¹. Besides the three bands originating in the X³Σ_g⁻, v'' = 0 ground state also the (2, 1) band probing vibrationally excited population was observed at room temperature overlapping the (0, 0) band. Phenomena of predissociation are associated with the line-widths, which can be seen to vary in figure 7.3 for the various v' levels. In future publications more details on the spectroscopy and on vibrational and spin-dependent predissociation rates (including a comparison with calculations of reference 117) will be presented.

In addition to absorption measurements on the Schumann-Runge resonance features, pressure dependent extinction features were investigated in the Herzberg continuum of oxygen around 198 nm. The absorption in the Herzberg continuum in O₂ at wavelengths shorter than 240 nm is strongly modified by collisions, connected to a change in the dipole moment of the molecule, which breaks the symmetry rule that otherwise disallows the transition [87, 88]. This leads to an intensity of

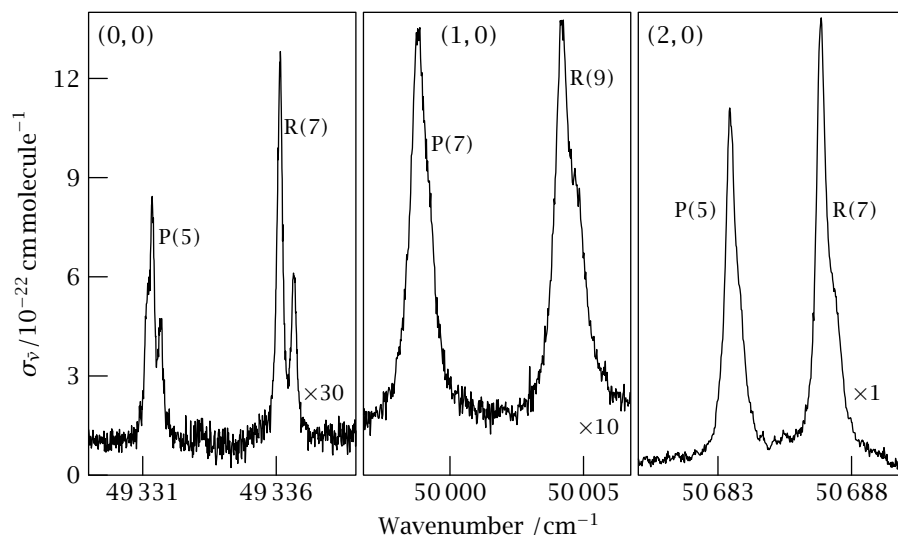


Figure 7.3 Spectral recording of part of the $B^3\Sigma_u^- \leftarrow X^3\Sigma_g^- (v', 0)$ band in molecular oxygen. As the (0,0) and (1,0) bands are the weakest, those signals were multiplied with the indicated factor. All sections of the spectrum span 10 cm^{-1} . The (0,0), (0,1) and (0,2) bands were measured at 290 mbar, 27.4 mbar and 4.3 mbar respectively.

Table 7.2 The extinction cross sections for O_2 in the Herzberg continuum.

Wavelength /nm	Linear contribution / $10^{-24} \text{ cm}^2 \text{ molecule}^{-1}$	Quadratic contribution / $10^{-45} \text{ cm}^5 \text{ molecule}^{-2}$
197.039	6.6 ± 0.8	549 ± 15
197.518	8.4 ± 0.8	580 ± 15
199.743	7.0 ± 0.8	471 ± 15
Results from Coquart <i>et al.</i> [88]		
197.04	8.10 ± 0.14	521 ± 6
197.52 ^a	8.0 ± 0.4	534 ± 20
197.76	8.04 ± 0.27	514 ± 16

^a Interpolated value

the continuum with a quadratic density dependence. The wavelength range 200–240 nm is important in atmospheric physics, as this falls between the absorption by ozone and the strong absorption of the Schumann–Runge bands. One CRD-monitored pressure scan in O_2 is shown in figure 7.2(b) for a measurement at 197.039 nm. A fit to the pressure-dependent loss rate gives both the linear and a quadratic contribution to the extinction. The results for oxygen are listed in table 7.2. Comparison with earlier measurements by Coquart *et al.* [88], shows a

reasonable agreement; Coquart *et al.* have a far lower resolution ($\sim 16 \text{ cm}^{-1}$) and need to subtract the Schumann-Runge bands, whereas our resolution is much higher and resonances could be avoided.

In conclusion the technique of cavity ring-down spectroscopy has been extended below 200 nm in the deep-UV range. The sensitivity is currently limited by the low reflectivity of available mirrors, and could be improved once better mirrors can be produced. The CRD technique is demonstrated in measurements on extinction of various gas phase molecules using a novel deep-UV pulsed laser source with narrow bandwidth.

The Space Research Organization Netherlands (SRON) and the Netherlands Foundation for Fundamental Research of Matter (FOM) are gratefully acknowledged for financial support.

Cavity ring-down spectroscopy of H_2^{18}O in the range $16\,570\text{ cm}^{-1}$ to $17\,120\text{ cm}^{-1}$

The absorption spectrum of water vapour is being comprehensively studied due to the high demand for accurate data for many aspects of science. Taking atmospheric science as an example, water vapour is the most important greenhouse gas and the major absorber of incoming sunlight. Besides the most abundant H_2^{16}O , its second most abundant isotopomer H_2^{18}O also contributes significantly to the absorption of solar radiation. Knowing the precise line positions and strengths of water isotopomers would therefore increase the accuracy of atmospheric modelling of the Earth as a whole. Furthermore, the 5ν region studied here lies in a window used for remote sensing [14]. H_2^{18}O has been much less extensively studied compared to H_2^{16}O and there has been no previous work on this isotopomer in this region.

The first experiment on H_2^{18}O at visible wavelengths was carried out in the early 1980's using the McMath Fourier transform spectrometer by Chevillard and co-workers at the National Solar Observatory in Kitt Peak, Arizona. They recorded long-pathlength spectra with isotopically enriched H_2^{18}O and H_2^{17}O samples over a wide frequency range and a series of papers have analysed these experimental results [118–128]. The data on H_2^{18}O in the HITRAN 2000 database [82] is limited, with the highest frequency listed for H_2^{18}O being $13\,900\text{ cm}^{-1}$, whereas for H_2^{16}O it extends to over $22\,600\text{ cm}^{-1}$. In addition, we found that this database appears to lack the entire 2ν polyad region of H_2^{18}O which Toth has extensively analysed [122].

A recent analysis of the H_2^{18}O spectrum by Tanaka *et al.* [127] extended the frequency range analysed up to $14\,520\text{ cm}^{-1}$, completely covering the $3\nu + \delta$ and 4ν polyad regions. In this study, pulsed cavity ring-down spectroscopy was used to record $16\,570\text{ cm}^{-1}$ – $17\,120\text{ cm}^{-1}$ frequency range which covers the 5ν polyad region. Naus *et al.* [129] studied the same frequency region for natural abundance water. This work concentrated on H_2^{16}O lines but also tentatively identified some transitions due to H_2^{18}O .

8.1 Experimental details

The experimental apparatus used in this experiment is the same as the one used in the earlier measurements on H_2^{16}O [129]. Wavelength tunable laser pulses with a bandwidth of $\sim 0.06\text{ cm}^{-1}$, produced by a Nd:YAG pumped dye laser system (Quanta Ray PDL-3) were used in a generic pulsed cavity ring-down experiment. The ring-down cell was 86.5 cm long and a single mirror set, with reflectivities varying between 99.97% near $16\,500\text{ cm}^{-1}$ and 99.995% near $17\,000\text{ cm}^{-1}$, was used over the entire wavelength range. The radius of curvature of the mirrors is 1 m , and the stable cavity was aligned such that the statistics on the weighted residuals of a

least squares fit were fully explained by contributions from Gaussian noise caused by the electronics and Poisson noise caused by the photon shot noise [33].

Before starting the measurements, the cell was heated to about 60 °C and flushed with dry nitrogen to remove as much of the natural water vapour from the cell as possible, without risk of damage to the mirrors. The liquid isotope enriched water – Euriso-top 96.5% atom ¹⁸O, 0.6% atom ¹⁷O, 2.9% atom ¹⁶O – was injected into the cavity while flushing the opening with a continuous dry nitrogen flow. The cell was then closed and partly evacuated, and several hours were allowed for the pressure to stabilise. In order not to lose isotopically enriched water, part of the dry nitrogen was left in the cell. The temperature in the cell was measured and the partial water vapour density in the cell was calculated assuming saturation density. The partial water vapour pressure at the set temperature corresponds to 24 mbar. To avoid condensation on the mirrors, the mirror-mounts were gently heated.

Data points were taken at a step size of 0.008 cm⁻¹ with averaging of five laser pulses at each laser frequency. The decay transients were detected using a photomultiplier tube, fed into a digital storage oscilloscope and then transferred to a computer where a least squares fitting routine was used to estimate the decay rates. This fitting routine is the same as the one used in aligning the cavity. These decay rates contain both the water vapour absorption spectrum and a background signal caused by the losses of the empty cavity; this smooth background was subtracted from the spectrum before analysing the resonance features. By recording an iodine spectrum simultaneously with the cavity ring-down spectrum a frequency calibration was obtained by comparing and interpolating the iodine spectrum against a reference atlas [34].

The spectra were searched by a computer program for possible locations of resonance features. A Voigt profile was then fitted to each of these candidate locations, yielding the central frequency, line-width and intensity. The entire spectrum was visually inspected to ensure that all fitted features were actual lines. Given the step size, the laser bandwidth and the width of the fitted lines, the one standard deviation error on the central frequency is estimated to be 0.01 cm⁻¹. The integrated line intensities, before correction associated with H₂¹⁶O contamination in the sample, were calculated using the fitted line parameters. Several error contributions can be distinguished in cavity ring-down spectroscopy: statistical effects, on the order of a few % in this experiment, a systematic underestimated absorption cross section on narrow band absorbers [29] and saturation effects related to non-exponential decay in the ring-down transients of the strongest lines. An additional error that is specific for this experiment is the uncertainty in the isotopic content of the ring-down cell. An estimate of the isotope ratio of H₂¹⁶O and H₂¹⁸O is given below, but a few % uncertainty must be added to the error budget. The total error on the line intensities is estimated to be 15%. The complete list of lines containing both the centre frequencies and the integrated line intensities is available in the electronic archive [130].

Despite our best effort to avoid contamination of the isotope enriched sample, several lines of H₂¹⁶O were visible in the measured spectrum. To weed out these H₂¹⁶O lines and identify which lines are H₂¹⁸O lines, we compared our new spec-

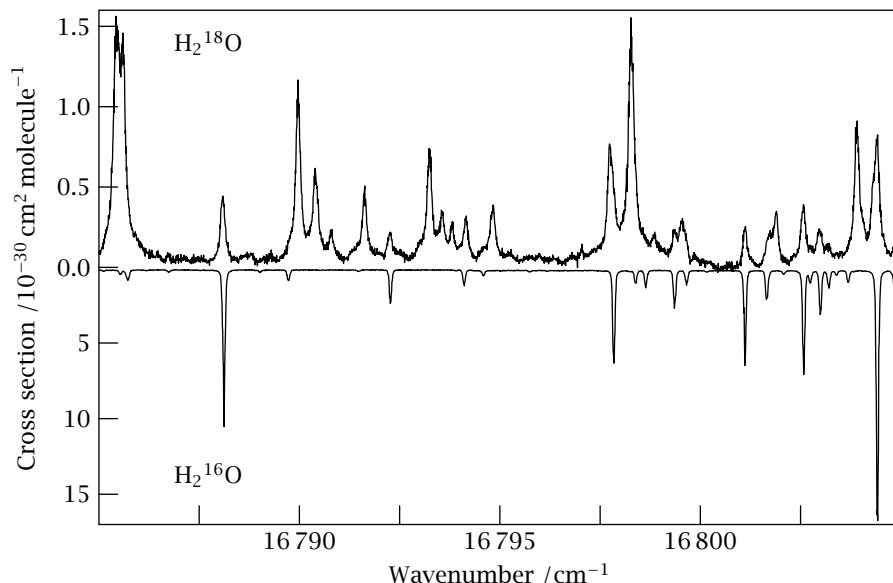


Figure 8.1 A portion of the measured spectrum in H_2^{18}O enriched water (top), compared with the H_2^{16}O spectrum measured previously by Naus et al. [129] (bottom). Lines only present in the top graph are H_2^{18}O lines. The pressure at which the top graph was measured was 24 mbar, while the bottom graph was measured at about 16 mbar. The vertical axis in the top graph is a cross section per molecule H_2^{18}O , the lines of H_2^{16}O in this graph are scaled with the isotope ratio.

trum with the previously measured spectrum, by plotting both in a single graph and manually assign each line to either H_2^{16}O or H_2^{18}O ; see figure 8.1 for a short portion of both spectra. In figure 8.1 the vertical axes are given in terms of a cross section per molecule. From the integrated intensity ratio of the H_2^{16}O lines in both spectra, the isotope ratio in the spectra can be estimated. Using this approach yields a H_2^{16}O contamination of about 10%. The integrated line intensities in the full spectrum are corrected for the isotope ratio in the cell.

The comparison between the measurements on the two isotopes clearly shows that the H_2^{18}O lines are broader than the H_2^{16}O lines, the difference being caused by the pressure conditions during the measurements. The width of the lines is $\sim 0.13 \text{ cm}^{-1}$ after fitting the spectra to a Voigt profile. This broadening beyond the laser line-width of 0.06 cm^{-1} is a result of collision broadening. Doppler broadening and self broadening at 24 mbar of water vapour yields a width of 0.09 cm^{-1} , the remainder of the broadening is attributed to nitrogen left behind in the cell during partial evacuation. The integrated intensities should be unaffected by the collisional broadening, and as the cell was saturated with water vapour, the density of the water vapour is known.

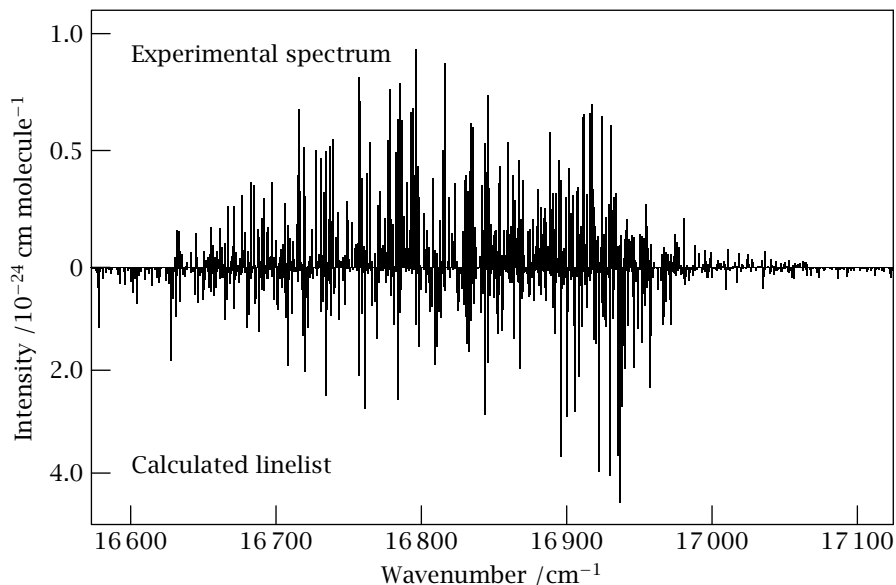


Figure 8.2 Overview of the H_2^{18}O experimental spectrum and the calculated line list in the 5ν polyad region.

8.2 Line Assignments

To help making line assignments, a new line list for H_2^{18}O was generated using the DVR3D program suite [131]. The program requires an external Potential Energy Surface (PES) and a Dipole Moment Surface (DMS) and uses variational techniques to calculate rotation–vibration energy levels of triatomic molecules. A good PES is essential for accurate prediction of energy levels. In this study, we have used the PES developed by Shirin *et al.* [132]. This PES was fitted to an extensive dataset of H_2^{16}O energy levels including those generated from the cavity ring-down spectrum by Naus *et al.* [129].

The following parameters were used to calculate the line list. For vibrational states, Radau coordinates were selected. 34 radial points based on a Morse oscillator-like functions [131] and 40 Gauss (associated) Legendre angular grid points were used to generate 2000 dimension final vibrational Hamiltonians. For rotationally excited states, the lowest 1000 vibrational functions were read for each value of k ($\approx K_a$) and final Hamiltonians of dimension $450 \times (J + 1)$ were diagonalised up to $J = 10$. A temperature of 296 K (room temperature) was used for calculations of transitions. Figure 8.2 compares the measured H_2^{18}O absorption spectrum with our calculated line list.

Initial assignments were made by comparing the experimental lines with the line list, taking both frequency and intensity into consideration. Upper energy levels were then determined and all possible combinations of transitions were generated

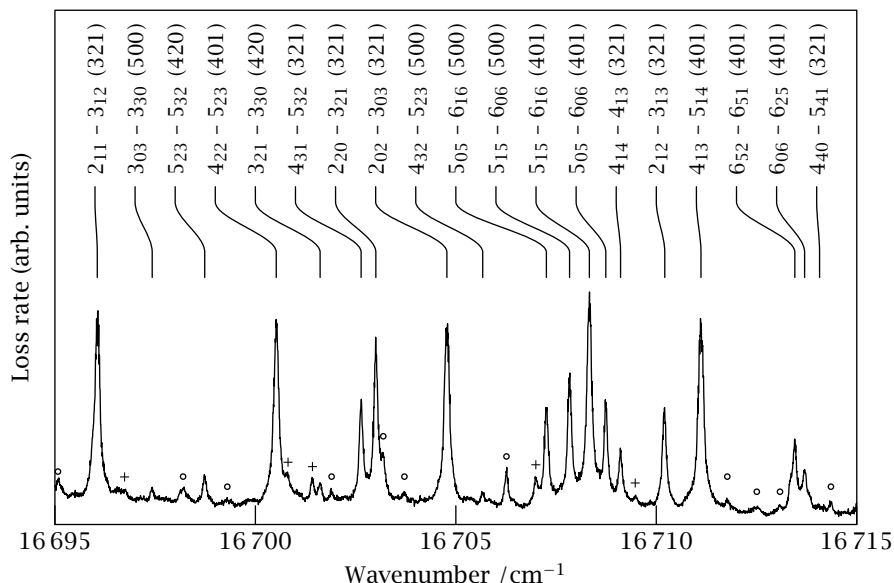


Figure 8.3 Experimental spectrum in the 16695 cm^{-1} to 16715 cm^{-1} range with the assignments. \circ indicates H_2^{16}O lines - taken from reference [129] - and $+$ indicates unassigned H_2^{18}O lines.

to search for further assignments by combination differences. Upper energy levels that were not confirmed by combination differences were re-considered and any necessary changes were made. Figure 8.3 shows a part of spectrum with the assignments. The ratios of new energy levels of H_2^{18}O to known H_2^{16}O levels proved to be extremely helpful for checking the reliability of assignments, as it is known these ratios are approximately constant within a vibrational band [127].

We assigned 375 of the 596 H_2^{18}O lines to 10 different upper vibrational levels. Table 8.1 shows the summary of the result. All transitions originate in the (000) ground vibrational level. Two new vibrational band origins were determined directly by transitions to their 0_{00} states: the (321) transition at 16775.381 cm^{-1} and the (401) transition at 16854.991 cm^{-1} . The band origin for the (500) transition can be estimated at $(16854.84 \pm 0.02)\text{ cm}^{-1}$ using the systematic error in our calculations. This procedure has been shown to work well in the past [133]. Table 8.2 shows the newly determined energy levels labelled with both normal and local mode notations. O - C shows the differences between an experimentally determined and the theoretically predicted energy level. All the assigned transitions and the energy levels can be found in the electronic archive [130].

Table 8.1 *Summary of H₂¹⁸O energy levels determined in this study. Bands are labelled using normal mode (left) and local mode (right) notations. ‘No. of levels’ shows the number of newly determined energy levels. ‘No. of trans.’ shows the number of transitions to the vibrational bands.*

Band	Origin /cm ⁻¹	No. of levels	No. of trans.
(340) or 30 ⁺⁴	—	11	20
(241) or 30 ⁻⁴	—	7	12
(043) or 21 ⁻⁴	—	3	3
(142) or 21 ⁺⁴	—	12	19
(222) or 31 ⁺²	—	9	7
(420) or 40 ⁺²	—	29	39
(321) or 40 ⁻²	16 775.381	42	83
(302) or 41 ⁺⁰	—	1	2
(500) or 50 ⁺⁰	16 854.84	43	80
(401) or 50 ⁻⁰	16 854.991	50	110
Total		207	375

Table 8.2 *H₂¹⁸O energy levels in cm⁻¹ for the (321), (500) and (401) vibrational states. Also given are the number of transitions assigned to each level and the differences O – C between experimentally determined levels and our theoretical predictions.*

<i>J</i>	<i>K_a</i>	<i>K_c</i>	(321) or 40 ⁻²	O – C	(500) or 50 ⁺⁰	O – C	(401) or 50 ⁻⁰	O – C
0	0	0	16 775.381	1	0.431		16 854.991	1 -0.259
1	0	1	16 797.751	2	0.436	16 876.838	1 -0.152	16 877.127 2 -0.165
1	1	1	16 812.558	1	0.176	16 887.674	2 -0.164	16 887.956 1 -0.180
1	1	0	16 818.257	1	0.132	16 892.781	1 -0.145	16 893.063 2 -0.173
2	0	2	16 841.104	2	0.451	16 919.565	1 -0.177	16 919.869 1 -0.202
2	1	2	16 851.770	2	0.410	16 926.727	3 -0.166	16 926.995 3 -0.166
2	1	1	16 868.947	2	0.405	16 941.961	1 -0.187	16 942.284 3 -0.164
2	2	1	16 912.252	1	-0.042	16 975.261	1 -0.297	16 975.532 1 -0.165
2	2	0	16 913.804	2	0.281	16 977.073	1 0.126	16 976.948 3 -0.155
3	0	3	16 903.088	2	0.423	16 979.733	4 -0.070	16 980.198 2 -0.117
3	1	3	16 905.182	2	0.061	16 984.457	2 -0.148	16 984.835 2 -0.120
3	1	2	16 943.465	2	0.392	17 014.705	3 -0.145	17 015.001 2 -0.140
3	2	2	16 979.495	3	0.285	17 041.940	2 -0.114	17 041.964 2 -0.162
3	2	1	16 986.445	2	0.249	17 048.278	2 -0.104	17 048.333 1 -0.171
3	3	1	17 115.166	2	-0.054	17 059.953	2 -0.328	17 061.423 4 0.071
3	3	0	17 115.365	2	-0.085	17 060.270	3 -0.258	17 061.659 1 0.060
4	0	4	16 979.033	2	0.384	17 058.157	1 -0.181	17 058.363 1 -0.147

Table 8.2 (continued)

<i>J</i>	<i>K_a</i>	<i>K_c</i>	(321) or 40 ⁻²	O – C	(500) or 50 ⁺⁰	O – C	(401) or 50 ⁻⁰	O – C			
4	1	4	16983.912	1	-0.020	17060.221	1	-0.196	17060.411	2	-0.163
4	1	3	17040.529	3	0.359	17109.231	2	-0.165	17109.490	3	-0.159
4	2	3	17067.391	1	0.284	17129.480	2	-0.060	17129.345	2	-0.145
4	2	2	17084.209	3	0.275	17145.664	2	-0.104	17145.670	4	-0.131
4	3	2	17206.628	1	-0.292	17150.823	2	-0.125	17151.466	3	-0.026
4	3	1	17208.361	3	-0.065	17152.405	2	0.014	17152.249	3	-0.057
4	4	1				17250.003	1	-0.291	17250.636	1	-0.259
4	4	0	17318.857	2	0.217	17250.447	2	0.112	17250.811	1	-0.060
5	0	5	17076.303	1	0.033	17152.600	3	-0.154	17153.584	3	-0.148
5	1	5	17077.137	1	0.403	17152.692	2	-0.153	17153.671	3	-0.150
5	1	4	17157.904	3	0.310	17223.347	1	-0.232	17223.609	3	-0.146
5	2	4	17175.241	3	0.252	17237.120	1	-0.074	17236.784	4	-0.122
5	2	3	17207.731	4	0.259	17268.684	2	-0.044	17268.425	2	-0.110
5	3	3	17321.491	4	0.146	17263.668	3	-0.052	17264.399	4	-0.077
5	3	2	17326.788	2	-0.012	17269.334	3	-0.062	17268.533	2	-0.401
5	4	2	17435.397	1	0.287	17363.369	1	-0.082	17363.554	2	-0.343
5	4	1	17435.068	2	-0.256	17363.475	3	-0.322	17363.609	2	0.065
5	5	1	17496.634	1	-0.217	17456.692	2	0.020	17456.947	2	-0.004
5	5	0				17456.703	2	0.025	17456.722	1	-0.236
6	0	6							17264.145	2	-0.133
6	1	6				17263.546	2	-0.142	17264.166	2	-0.131
6	1	5	17293.138	3	0.238	17355.452	1	-0.087	17355.477	3	-0.102
6	2	5				17364.686	1	0.047	17363.699	2	0.200
6	2	4							17411.992	3	-0.122
6	3	4	17458.118	3	-0.012	17399.119	2	0.475	17399.527	5	-0.077
6	3	3	17471.645	3	-0.019	17411.699	1	0.388	17409.519	1	-0.152
6	4	3				17499.669	1	0.255	17499.726	2	-0.341
6	4	2	17575.652	1	-0.385				17501.234	2	-0.374
6	5	2							17593.567	2	0.047
6	5	1							17593.561	2	-0.023
6	6	0							17726.192	1	-0.215
7	1	7							17391.441	2	-0.141
7	1	6				17503.917	2	0.237			
7	2	6	17447.102	1	0.159						
7	3	5	17616.343	2	0.097						
7	3	4	17642.801	2		17575.265	3	-0.377			
8	0	8							17535.562	2	-0.128

8.3 Discussion and Conclusion

The reliability of the new line list was first tested by analysing the H₂¹⁸O spectrum in the 12 400 cm⁻¹ to 14 520 cm⁻¹ range. In our previous study 747 of 927 lines were assigned using the line list generated by Partridge and Schwenke [127]. With our new line list, it was possible to make assignments to more than 800 lines. This test was particularly useful for checking the labelling of energy levels. Details will be given elsewhere [134].

Naus *et al.* assigned 6 of their transitions recorded using natural abundance water to H₂¹⁸O. We find one of their lines was previously mis-assigned. The line at 16 761.672 cm⁻¹ was assigned to 3₁₃ – 4₁₄ 401-000 (H₂¹⁸O) but the correct assignment is 5₂₄ – 5₃₃ 142-000 (H₂¹⁶O). The 3₁₃ – 4₁₄ 401-000 (H₂¹⁸O) line lies at 16 761.004 cm⁻¹.

The absorption spectrum of H₂¹⁸O recorded using the cavity ring-down spectroscopy has been analysed. 596 lines were identified as H₂¹⁸O and 375 of which are now assigned using the newly calculated line list. The frequency range analysed in this paper is the highest for H₂¹⁸O to date and the results should be used for atmospheric and other studies.

Acknowledgements

This study is supported by the European Community – Access to Research Infrastructures action of the Improving Human Potential Program (Contract HPRI-CT-1999-00064) and by the Earth Observation program of the Space Research Organization Netherlands (SRON).

Bibliography

For many articles a 'digital object identifier' (DOI) is added. These articles can be found on the internet, through the URI: '<http://dx.doi.org>', and typing the DOI in the box on the website. You will then reach the abstract of the article, and from there the pdf-version of the article, provided your institution has access to the journal.

- [1] J. C. Farman, B. G. Gardiner and J. D. Shanklin, 'Large losses of total ozone in antarctica reveal seasonal ClO_x/NO_x interaction'. *Nature* **315**, 207-210 (1985). Cited on page 2.
- [2] D. W. Fahey, 'Twenty questions and answers about the ozone layer', in 'Scientific assessment of ozone depletion: 2002', (edited by C. A. Ennis *et al.*), Global Ozone Research and Monitoring Project, NOAA, NASA, United Nations Environment Programme, World Meteorological Organization and European Commission (2002), URI: '<http://www.epa.gov/ozone/science/>'. Cited on page 3.
- [3] A. P. M. Baede, E. Ahlonsou, Y. Ding and D. Schimmel, 'The climate system: an overview', in 'Climate Change 2001: The Scientific Basis. Contribution of Working Group I to the Third Assessment Report of the Intergovernmental Panel on Climate Change', (edited by J. T. Houghton, Y. Ding, D. J. Griggs, M. Noguer, P. J. van der Linden, X. Dai, K. Maskell and C. A. Johnson), Cambridge University Press, Cambridge, United Kingdom and New York, NY, USA (2001), ISBN 0521 01495 6, URI: 'http://www.grida.no/climate/ipcc_tar/wg1/index.htm'. Cited on page 2.
- [4] J. L. Sarmiento and N. Gruber, 'Sinks for anthropogenic carbon'. *Physics Today* **55**, 30-36 (2002). Cited on page 4.
- [5] J. R. Petit, J. Jouzel, D. Raynaud, N. I. Barkov, J.-M. Barnola, I. Basile, M. Bender, J. Chappellaz, M. Davis, G. Delaygue, M. Delmotte, V. M. Kotlyakov, M. Legrand, V. Y. Lipenkov, C. Lorius, L. Pépin, C. Ritz, E. Saltzman and M. Stievenard, 'Climate and atmospheric history of the past 420 000 years from the Vostok ice core, Antarctica'. *Nature* **399**, 429-436 (1999), DOI: '10.1038/20859'. Cited on page 3.
- [6] EPICA community members, 'Eight glacial cycles from an Antarctic ice core'. *Nature* **429**, 623-628 (2004), DOI: '10.1038/nature02599'. Cited on page 3.
- [7] J. C. Comiso, 'Warming trends in the arctic from clear sky satellite observations'. *J. Climate* **16**, 3498-3510 (2003). Cited on page 3.
- [8] D. J. Travis, A. M. Carleton and R. G. Lauritsen, 'Contrails reduce daily temperature range'. *Nature* **418**, 601 (2002), DOI: '10.1038/418601a'. Cited on page 3.
- [9] R. Lang, *Spectral sampling techniques for atmospheric modeling: Modeling and retrieval of atmospheric water vapor*, Ph.D. thesis, Vrije Universiteit,

- Amsterdam, De Boelelaan 1105, 1081 HV Amsterdam, The Netherlands (2002). Cited on page 5.
- [10] G. Scarpino, 'About the GOME (Global Ozone Monitoring Experiment)', URI: '<http://earth.esa.int/rootcollection/eeo4.10075/eeo4.10041.html>'. Cited on page 6.
- [11] P. F. Levelt *et al.*, 'Science requirements document for OMI-EOS', *Technical Report RS-OMIE-KNMI-001*, KNMI, De Bilt, The Netherlands (2000). Cited on page 6.
- [12] S. Slijkhuis *et al.*, 'GOME data processor extraction software user's manual', *Technical Report ER-SUM-DLR-GO-0045*, DLR, Oberpfaffenhofen, Germany (1999), URI: 'http://auc.dfd.dlr.de/GOME/docs/gdp01_12_ex.ps'. Cited on page 6.
- [13] J. R. Acarreta and J. F. de Haan, 'Cloud pressure algorithm based on O₂-O₂ absorption', *Technical Report SN-OMIE-KNMI-328*, KNMI, De Bilt, The Netherlands (2001). Cited on pages 6 and 58.
- [14] R. Lang, A. N. Maurellis, W. J. van der Zande, I. Aben, J. Landgraf and W. Ubachs, 'Forward modeling and retrieval of water vapor from GOME: Treatment of narrow band absorption spectra'. *J. Geophys. Res.* **107**, 4300 (2002), DOI: '10.1029/2001JD001453'. Cited on pages 8 and 77.
- [15] A. Kastler, 'Atomes à l'Intérieur d'un Interféromètre Perot-Fabry'. *Appl. Opt.* **1**, 17-24 (1962). Cited on page 9.
- [16] T. Hänsch, A. Schawlow and P. Toschek, 'Ultrasensitive response of a CW dye laser to selective extinction'. *IEEE J. Quantum. Electron.* **8**, 802-804 (1972). Cited on page 9.
- [17] J. M. Herbelin, J. A. McKay, M. A. Kwok, R. H. Ueunten, D. S. Urevig, D. J. Spencer and D. J. Benard, 'Sensitive measurement of photon lifetime and true reflectances in an optical cavity by a phase-shift method'. *Appl. Opt.* **19**, 144-147 (1980). Cited on page 9.
- [18] A. O'Keefe and D. A. G. Deacon, 'Cavity ring-down optical spectrometer for absorption measurements using pulsed laser sources'. *Rev. Sci. Instrum.* **59**, 2544-2551 (1988), DOI: '10.1063/1.1139895'. Cited on pages 9 and 71.
- [19] M. D. Wheeler, S. M. Newman, A. J. Orr-Ewing and M. N. R. Ashfold, 'Cavity ring-down spectroscopy'. *J. Chem. Soc., Faraday Trans.* **94**, 337-351 (1998), DOI: '10.1039/a707686j'. Cited on page 9.
- [20] G. Berden, R. Peeters and G. Meijer, 'Cavity ring-down spectroscopy: Experimental schemes and applications'. *Int. Rev. in Phys. Chem.* **19**, 565-607 (2000), DOI: '10.1080/014423500750040627'. Cited on pages 9 and 71.
- [21] G. Berden, G. Meijer and W. Ubachs, 'Spectroscopic applications using ring-down cavities', in 'Cavity enhanced spectroscopies', (edited by R. van Zee and J. P. Looney), volume 40 of *Experimental methods in physical sciences*, chapter 2, 47-82, Academic Press (2002), ISBN 0124759874. Cited on page 9.
- [22] W. Demtröder, *Laser spectroscopy, basic concepts and instrumentation*, Springer Verlag (1981), ISBN 3 540 10343 0. Cited on pages 9, 11 and 12.
- [23] H. Kogelnik and T. Li, 'Laser beams and resonators'. *Appl. Opt.* **5**, 1550-1567 (1966). Cited on pages 11 and 12.

- [24] G. Meijer, M. G. H. Boogaarts, R. T. Jongma, D. H. Parker and A. M. Wodtke, 'Coherent cavity ring down spectroscopy'. *Chem. Phys. Lett.* **217**, 112-116 (1994), DOI: '10.1016/0009-2614(93)E1361-J'. Cited on pages 12 and 16.
- [25] M. Abramowitz and I. A. Stegun (editors), *Handbook of mathematical functions with formulas, graphs, and mathematical tables*, Dover Publications, Inc., New York (1972). Cited on page 12.
- [26] H. Naus, A. de Lange and W. Ubachs, ' $b^1\Sigma_g^+ \leftarrow X^3\Sigma_g^-(0,0)$ band of oxygen isotopomers in relation to tests of the symmetrization postulate in $^{16}\text{O}_2$ '. *Phys. Rev. A* **56**, 4755-4763 (1997), DOI: '10.1103/PhysRevA.56.4755'. Cited on pages 14 and 15.
- [27] H. Naus, S. J. van der Wiel and W. Ubachs, 'Cavity ring-down spectroscopy on the $b^1\Sigma_g^+ \leftarrow X^3\Sigma_g^-(1,0)$ band of oxygen isotopomers'. *J. Mol. Spectrosc.* **192**, 162-168 (1998), DOI: '10.1006/jmsp.1998.7684'. Cited on page 15.
- [28] H. Naus, K. Navaian and W. Ubachs, 'The γ -band of $^{16}\text{O}_2$, $^{16}\text{O}^{17}\text{O}$, $^{17}\text{O}_2$ and $^{18}\text{O}_2$ '. *Spectrochim. Act. A* **55**, 1255-1262 (1999), DOI: '10.1016/S1386-1425(98)00318-7'. Cited on page 15.
- [29] J. T. Hodges, J. P. Looney and R. D. van Zee, 'Laser bandwidth effects in quantitative cavity ring-down spectroscopy'. *Appl. Opt.* **35**, 4112-4116 (1996). Cited on pages 15 and 78.
- [30] P. Zalicki and R. N. Zare, 'Cavity ring-down spectroscopy for quantitative absorption measurements'. *J. Chem. Phys.* **102**, 2708-2717 (1995), DOI: '10.1063/1.468647'. Cited on page 15.
- [31] R. D. van Zee, J. T. Hodges and J. P. Looney, 'Pulsed, single-mode cavity ringdown spectroscopy'. *Appl. Opt.* **38**, 3951-3960 (1999). Cited on pages 15 and 16.
- [32] R. T. Jongma, M. G. H. Boogaarts, I. Holleman and G. Meijer, 'Trace gas detection with cavity ring down spectroscopy'. *Rev. Sci. Instrum.* **66**, 2821-2828 (1995), DOI: '10.1063/1.1145562'. Cited on pages 15, 71 and 72.
- [33] H. Naus, I. H. M. van Stokkum, W. Hogervorst and W. Ubachs, 'Quantitative analysis of decay transients applied to a multimode pulsed cavity ringdown experiment'. *Appl. Opt.* **40**, 4416-4426 (2001). Cited on pages 15, 16, 18, 51, 52, 72 and 78.
- [34] S. Gerstenkorn and P. Luc, *Atlas du Spectroscopie d'Absorption de la Molécule de l'Iode entre 14 800 - 20 000 cm^{-1}* , Presses du CNRS, Paris (1978). Cited on pages 18 and 78.
- [35] J. W. Strutt (Lord Rayleigh), 'On the transmission of light through an atmosphere containing small particles in suspension, and on the origin of the blue of the sky'. *Philos. Mag.* **47**, 375-384 (1899), reprinted in: Lord Rayleigh, *Scientific papers*, Dover Publications, New York (1964), part IV, page 397. Cited on pages 21, 26 and 28.
- [36] H. Naus and W. Ubachs, 'Experimental verification of Rayleigh scattering cross sections'. *Opt. Lett.* **25**, 347-349 (2000). Cited on pages 21, 32, 33, 36 and 72.
- [37] R. W. Boyd, *Nonlinear optics*, Academic Press, San Diego (1992), ISBN 0 12 121680 2. Cited on pages 22, 28, 29 and 30.

- [38] J. D. Jackson, *Classical electrodynamics*, third edition, John Wiley and Sons, Inc., New York (1999), ISBN 0 471 30932 x. Cited on pages 23 and 24.
- [39] U. Hohm and K. Kerl, 'Interferometric measurements of the dipole polarizability α of molecules between 300 K and 1100 K I. Monochromatic measurements at $\lambda = 632.99$ nm for the noble gases and H₂, N₂, O₂ and CH₄'. *Mol. Phys.* **69**, 803–817 (1990). Cited on page 24.
- [40] A. Bucholtz, 'Rayleigh-scattering calculations for the terrestrial atmosphere'. *Appl. Opt.* **34**, 2765–2773 (1995). Cited on page 24.
- [41] H. C. van de Hulst, *Light scattering by small particles*, Dover Publications (1981), ISBN 0 486 64228 3. Cited on pages 25, 26 and 27.
- [42] R. J. Strutt, 'The light scattered by gases: Its polarisation and intensity'. *Proc. Roy. Soc. London* **95**, 155–176 (1918). Cited on page 26.
- [43] R. J. Strutt, 'A re-examination of the light scattered by gases in respect of polarisation. I. Experiments on the common gases'. *Proc. Roy. Soc. London* **97**, 435–450 (1920). Cited on page 26.
- [44] L. V. King, 'On the complex anisotropic molecule in relation to the dispersion and scattering of light'. *Proc. Roy. Soc. London* **104**, 333–357 (1923). Cited on pages 26, 27 and 28.
- [45] A. T. Young, 'Rayleigh scattering'. *Appl. Opt.* **20**, 533–535 (1981). Cited on page 27.
- [46] R. B. Miles, W. R. Lempert and J. N. Forkey, 'Laser Rayleigh scattering'. *Meas. Sci. Technol.* **12**, R33–R51 (2001), DOI: '10.1088/0957-0233/12/5/201'. Cited on page 27.
- [47] G. R. Alms, A. K. Burnham and W. H. Flygare, 'Measurement of the dispersion in polarizability anisotropies'. *J. Chem. Phys.* **63**, 3321–3326 (1975), DOI: '10.1063/1.431821'. Cited on pages 27, 30, 34, 35, 38 and 39.
- [48] D. R. Bates, 'Rayleigh scattering by air'. *Planet. Space Sci.* **32**, 785–790 (1984), DOI: '10.1016/0032-0633(84)90102-8'. Cited on pages 28, 31, 34, 35, 40, 41 and 52.
- [49] H. Z. Cummins and R. W. Gammon, 'Rayleigh and Brillouin scattering in liquids: The Landau-Placzek ratio'. *J. Chem. Phys.* **44**, 2785–2797 (1966). Cited on page 29.
- [50] G. Verkerk, J. B. Broens, W. Kranendonk, F. J. v.d. Puijl, J. L. Sikkema and C. W. Stam (editors), *Binas*, second edition, Wolters-Noordhoff, Groningen, the Netherlands (1986), ISBN 90 01 89351 1. Cited on page 29.
- [51] C. M. Penney, 'Light scattering in terms of oscillator strengths and refractive indices'. *J. Opt. Soc. Am.* **59**, 34–42 (1969). Cited on page 29.
- [52] W. Knippers, K. van Helvoort and S. Stolte, 'Vibrational overtones of the homonuclear diatoms (N₂, O₂, D₂) observed by the spontaneous Raman effect'. *Chem. Phys. Lett.* **121**, 279–286 (1985), DOI: '10.1016/0009-2614(85)87179-7'. Cited on page 30.
- [53] G. Herzberg, *Molecular spectra and molecular structure I. Diatomic molecules*, second edition, Van Nostrand Reinhold, London (1950), ISBN 0 442 03385 0. Cited on page 30.
- [54] H. Moosmüller, 'Optical absorption in nitrogen due to spontaneous Raman

- scattering'. *J. Opt. Soc. Am. B* **11**, 286–289 (1994). Cited on page 30.
- [55] N. J. Bridge and A. D. Buckingham, 'The polarization of laser light scattered by gases'. *Proc. R. Soc. A* **295**, 334–349 (1966). Cited on pages 30, 34, 39 and 74.
- [56] C. M. Penney, R. L. St. Peters and M. Lapp, 'Absolute rotational Raman cross sections for N₂, O₂ and CO₂'. *J. Opt. Soc. Am.* **64**, 712–715 (1974). Cited on page 30.
- [57] A. L. Ford and J. C. Browne, 'Direct-resolvent-operator computations on the hydrogen-molecule dynamic polarizability, Rayleigh, and Raman scattering'. *Phys. Rev. A* **7**, 418–426 (1973), DOI: '10.1103/PhysRevA.7.418'. Cited on page 30.
- [58] J. Rychlewski, 'An accurate calculation of the polarizability of the hydrogen molecule and its dependence on rotation, vibration and isotopic substitution'. *Mol. Phys.* **41**, 833–842 (1980). Cited on page 30.
- [59] S. R. Langhoff and C. W. Bauschlicher, Jr., 'Theoretical study of the effects of vibrational-rotational interactions on the Raman spectrum of N₂'. *J. Chem. Phys.* **78**, 5287–5292 (1983), DOI: '10.1063/1.445482'. Cited on page 30.
- [60] J. Oddershede and E. N. Svendsen, 'Dynamic polarizabilities and Raman intensities of CO, N₂, HCl and Cl₂'. *Chem. Phys.* **64**, 359–369 (1982), DOI: '10.1016/0301-0104(82)80004-9'. Cited on pages 30, 34 and 39.
- [61] P. L. Smith, M. C. E. Huber and W. H. Parkinson, 'Refractivities of H₂, He, O₂, CO and Kr for 168 ≤ λ ≤ 288 nm'. *Phys. Rev. A* **13**, 1422–1434 (1976), DOI: '10.1103/PhysRevA.13.1422'. Cited on pages 30, 37 and 38.
- [62] E. R. Peck and D. J. Fisher, 'Dispersion of argon'. *J. Opt. Soc. Am.* **54**, 1362–1364 (1964). Cited on pages 33 and 34.
- [63] A. Bideau-Mehu, Y. Guern, R. Abjean and A. Johannin-Gilles, 'Interferometric determination of the refractive index of carbon dioxide in the ultraviolet region'. *Opt. Comm.* **9**, 432–434 (1973), DOI: '10.1016/0030-4018(73)90289-7'. Cited on pages 34 and 35.
- [64] E. R. Peck and B. N. Khanna, 'Dispersion of nitrogen'. *J. Opt. Soc. Am.* **56**, 1059–1063 (1966). Cited on page 34.
- [65] R. Abjean, A. Méhu and A. Johannin-Gilles, 'Mesure interférométrique des indices de réfraction de l'azote et de l'argon dans l'ultraviolet'. *C. R. Acad. Sc. Paris* **271**, 411–414 (1970). Cited on page 34.
- [66] P. M. Teillet, 'Rayleigh optical depth comparisons from various sources'. *Appl. Opt.* **29**, 1897–1900 (1990). Cited on page 36.
- [67] U. Hohm, 'Experimental determination of the dispersion in the mean linear dipole polarizability $\alpha(\omega)$ of small hydrocarbons and evaluation of Cauchy moments between 325 nm and 633 nm'. *Mol. Phys.* **78**, 929–941 (1993). Cited on pages 38 and 39.
- [68] D. Vukovic, G. A. Woolsey and G. B. Scelsi, 'Refractivities of SF₆ and SOF₂ at wavelengths of 632.99 and 1300 nm'. *J. Phys. D* **29**, 634–637 (1996), DOI: '10.1088/0022-3727/29/3/023'. Cited on pages 38, 39 and 74.
- [69] G. D. Greenblatt, J. J. Orlando, J. B. Burkholder and A. R. Ravishankara, 'Absorption measurements of Oxygen between 330 and 1140 nm'. *J. Geophys.*

- Res.* **95**, 18 577–18 582 (1990). Cited on pages 41, 47, 48, 50, 54 and 67.
- [70] D. A. Newnham and J. Ballard, ‘Visible absorption cross sections and integrated absorption intensities of molecular oxygen (O_2 and O_4)’. *J. Geophys. Res.* **103**, 28 801–28 815 (1998), DOI: ‘10.1029/98JD02799’. Cited on pages 41, 48, 50, 54, 66, 67, 68 and 69.
- [71] A. Halkier, S. Coriani and P. Jorgensen, ‘The molecular electric quadrupole moment of N_2 ’. *Chem. Phys. Lett.* **294**, 292–296 (1998), DOI: ‘10.1016/S0009-2614(98)00878-1’. Cited on page 43.
- [72] P. Wormer and A. van der Avoird, ‘(Heisenberg) exchange and electrostatic interactions between O_2 molecules: An *ab initio* study’. *J. Chem. Phys.* **81**, 1929–1939 (1984), DOI: ‘10.1063/1.447867’. Cited on pages 43, 45, 49 and 57.
- [73] S. Yu. Epifanov and A. A. Vigasin, ‘Contribution of bound, metastable and free states of bimolecular complexes to collision-induced intensity of absorption’. *Chem. Phys. Lett.* **225**, 537–541 (1994), DOI: ‘10.1016/0009-2614(94)87124-8’. Cited on pages 43, 47 and 69.
- [74] C. Camy-Peyret and A. A. Vigasin (editors), *Weakly interacting molecular pairs: unconventional absorbers of radiation in the atmosphere*, volume 27 of *NATO Science Series: IV. Earth and Environmental Sciences*, Kluwer Academic Publishers, Dordrecht, Boston, London (2003), ISBN 1 4020 1596 8, proceedings of the NATO Advanced Research Workshop, Fontevraud, France, April 29 – May 3, 2002. Cited on pages 43, 47 and 48.
- [75] J. F. Babb and A. Dalgarno, ‘Radiative association and inverse predissociation of oxygen atoms’. *Phys. Rev. A* **51**, 3021–3026 (1995), DOI: ‘10.1103/PhysRevA.51.3021’. Cited on page 45.
- [76] P. Saxon, Roberta and B. Liu, ‘*Ab initio* configuration interaction study of the valence states of O_2 ’. *J. Chem. Phys.* **67**, 5432–5441 (1977), DOI: ‘10.1063/1.434764’. Cited on page 45.
- [77] R. S. Friedman, ‘Oscillator strengths of the Schumann–Runge bands of isotopic oxygen molecules’. *J. Quant. Spectrosc. Radiat. Transfer* **43**, 225–238 (1990), DOI: ‘10.1016/0022-4073(90)90055-B’. Cited on page 45.
- [78] M. C. G. N. van Vroonhoven and G. C. Groenenboom, ‘Photodissociation of O_2 in the Herzberg continuum. I. *Ab initio* calculation of potential energy curves and properties’. *J. Chem. Phys.* **116**, 1954–1964 (2002), DOI: ‘10.1063/1.1427714’. Cited on page 45.
- [79] G. C. Groenenboom and D. T. Colbert, ‘Combining the discrete variable representation with the S-matrix Kohn method for quantum reactive scattering’. *J. Chem. Phys.* **99**, 9681–9696 (1993), DOI: ‘10.1063/1.465450’. Cited on page 45.
- [80] T. G. Slanger and R. A. Copeland, ‘Energetic oxygen in the upper atmosphere and the laboratory’. *Chem. Rev.* **103**, 4731–4765 (2003), DOI: ‘10.1021/cr0205311’. Cited on page 44.
- [81] B. F. Minaev and H. Ågren, ‘Collision-induced $b^1\Sigma_g^+ - a^1\Delta_g$, $b^1\Sigma_g^+ - X^3\Sigma_g^-$ and $a^1\Delta_g - X^3\Sigma_g^-$ transition probabilities in molecular oxygen’. *J. Chem. Soc., Faraday Trans.* **93**, 2231–2239 (1997), DOI: ‘10.1039/a607263a’. Cited on

- page 44.
- [82] L. S. Rothman, A. Barbe, D. C. Benner, L. R. Brown, C. Camy-Peyret, M. R. Carleer, K. Chance, C. Clerbaux, V. Dana, V. M. Devi, A. Fayt, J.-M. Flaud, R. R. Gamache, A. Goldman, D. Jacquemart, K. W. Jucks, W. J. Lafferty, J. Y. Mandin, S. T. Massie, V. Nemtchinov, D. A. Newnham, A. Perrin, C. P. Rinsland, J. Schroeder, K. M. Smith, M. A. H. Smith, K. Tang, R. A. Toth, J. V. Auwera, P. Varanasi and K. Yoshino, 'The HITRAN molecular spectroscopic database: edition of 2000 including updates through 2001'. *J. Quant. Spectrosc. Radiat. Transfer* **82**, 5–44 (2003), DOI: '10.1016/S0022-4073(03)00146-8'. Cited on pages 44 and 77.
- [83] K. Yoshino, D. E. Freeman, J. R. Esmond and W. H. Parkinson, 'High resolution absorption cross section measurements and band oscillator strengths of the (1,0)–(12,0) Schumann–Runge bands of O₂'. *Planet. Space Sci.* **31**, 339–353 (1983). Cited on page 44.
- [84] A. S.-C. Cheung, D. K.-W. Mok, Y. Sun and D. E. Freeman, 'The potential energy curve for the B³Σ_u⁻ State of oxygen and accurate Franck–Condon factors for the Schumann–Runge bands'. *J. Mol. Spectrosc.* **163**, 9–18 (1994), DOI: '10.1006/jmbsp.1994.1002'. Cited on page 44.
- [85] V. D. Galkin, 'Electronic moment of the b¹Σ_g⁺–X³Σ_g⁻ transition of the oxygen band system'. *Opt. Spectrosc. (USSR)* **47**, 151–153 (1979). Cited on page 45.
- [86] S. Fally, A. C. Vandaele, M. Carleer, C. Hermans, A. Jenouvrier, M.-F. Mérienne, B. Coquart and R. Colin, 'Fourier transform spectroscopy of the O₂ Herzberg bands. III. Absorption cross sections of the collision-induced bands and of the Herzberg continuum'. *J. Mol. Spectrosc.* **204**, 10–20 (2000), DOI: '10.1006/jmbsp.2000.8204'. Cited on pages 46 and 47.
- [87] A. J. Blake and D. G. McCoy, 'The pressure dependence of the Herzberg photoabsorption continuum of oxygen'. *J. Quant. Spectrosc. Radiat. Transfer* **38**, 113–120 (1987), DOI: '10.1016/0022-4073(87)90037-9'. Cited on pages 46 and 74.
- [88] M. Coquart, M.-F. Mérienne and A. Jenouvrier, 'O₂ Herzberg continuum absorption cross-sections in the wavelength region 196–205 nm of the Schumann–Runge bands'. *Planet. Space Sci.* **38**, 287–300 (1990), DOI: '10.1016/0032-0633(90)90093-6'. Cited on pages 46, 74 and 75.
- [89] B. Bussery and P. E. S. Wormer, 'A van der Waals intermolecular potential for (O₂)₂'. *J. Chem. Phys.* **99**, 1230–1239 (1993), DOI: '10.1063/1.46536'. Cited on page 47.
- [90] L. Biennier, D. Romanini, A. Kachanov, A. Campargue, B. Bussery-Honvault and R. Bacis, 'Structure and rovibrational analysis of the [O₂(a¹Δ_g)_{v=0}]₂ ← [O₂(X³Σ_g⁻)_{v=0}]₂ transition of the O₂-dimer'. *J. Chem. Phys.* **112**, 6309–6321 (2000), DOI: '10.1063/1.481192'. Cited on pages 47, 48 and 57.
- [91] H. Salow and W. Steiner, 'Die durch Wechselwirkungskräfte bedingten Absorptionsspektren des Sauerstoffes, 1. Die Absorptionsbanden des (O₂–O₂)-Moleküls'. *Z. Phys.* **99**, 137–158 (1936). Cited on pages 47 and 50.
- [92] H. Naus and W. Ubachs, 'Visible absorption bands of the (O₂)₂ collision complex at pressures below 760 Torr'. *Appl. Opt.* **38**, 3423–3428 (1999). Cited

- on pages 47, 50, 57, 61, 65, 66 and 68.
- [93] M. Snee and W. Ubachs, 'Cavity ring-down measurements of the O₂-O₂ collision-induced absorption resonance at 477 nm at sub-atmospheric pressures'. *J. Quant. Spectrosc. Radiat. Transfer* **78**, 171-178 (2003), DOI: '10.1016/S0022-4073(02)00190-5'. Cited on pages 47, 54 and 65.
- [94] A. A. Vigasin, 'Collision-induced absorption in the region of the O₂ fundamental: Bandshapes and dimeric features'. *J. Mol. Spectrosc.* **202**, 59-66 (2000), DOI: '10.1006/jmsp.2000.8094'. Cited on pages 47 and 69.
- [95] R. P. Blickensderfer and G. E. Ewing, 'Collision-induced absorption spectrum of gaseous oxygen at low temperatures and pressures. II. The simultaneous transitions $^1\Delta_g + ^1\Delta_g \leftarrow ^3\Sigma_g^- + ^3\Sigma_g^-$ and $^1\Delta_g + ^1\Sigma_g^+ \leftarrow ^3\Sigma_g^- + ^3\Sigma_g^-$ '. *J. Chem. Phys.* **51**, 5284-5289 (1969), DOI: '10.1063/1.1671946'. Cited on pages 48, 54, 67 and 69.
- [96] A. McKellar, N. Rich and H. Welsh, 'Collision-induced vibrational and electronic spectra of gaseous oxygen at low temperatures'. *Can. J. Phys.* **50**, 1-9 (1972). Cited on pages 48, 50, 52, 54 and 64.
- [97] G. C. Tabisz, E. J. Allen and H. L. Welsh, 'Interpretation of the visible and near-infrared absorption spectra of compressed oxygen as collision-induced electronic transitions'. *Can. J. Phys.* **47**, 2859-2871 (1969). Cited on pages 48, 52, 54 and 64.
- [98] J. Morville, D. Romanini, A. Campargue and R. Bacis, 'OPO-pulsed CRDS of the visible collision-induced absorption bands of oxygen at low temperature'. *Chem. Phys. Lett.* **363**, 498-504 (2002), DOI: '10.1016/S0009-2614(02)01096-5'. Cited on pages 48, 67, 68 and 69.
- [99] K. Pfeilsticker, H. Bösch, C. Camy-Peyret, R. Fitzenberger, H. Harder and H. Osterkamp, 'First atmospheric profile measurements of UV/visible O₄ absorption band intensities: Implications for the spectroscopy, and the formation enthalpy of the O₂-O₂ dimer'. *Geophys. Res. Lett.* **28**, 4595-4598 (2001), DOI: '10.1029/2001GL013734'. Cited on pages 48 and 50.
- [100] J. Ellis and H. Kneser, 'Kombinationsbeziehungen im Absorptionsspektrum des flüssigen Sauerstoffes'. *Z. Phys.* **86**, 583-591 (1933). Cited on pages 49, 50 and 57.
- [101] C. Long and G. Ewing, 'Spectroscopic investigation of van der Waals molecules. I. The infrared and visible spectra of O₄'. *J. Chem. Phys.* **58**, 4824-4834 (1973), DOI: '10.1063/1.1679066'. Cited on pages 49, 50, 57, 67 and 69.
- [102] V. Aquilanti, D. Ascenzi, M. Bartolomei, D. Cappelletti, S. Cavalli, M. Vitores and F. Pirani, 'Molecular beam scattering of aligned oxygen molecules. The nature of the bond in the O₂-O₂ dimer'. *J. Am. Chem. Soc.* **121**, 10 794-10 802 (1999), DOI: '10.1021/ja9917215'. Cited on page 49.
- [103] A. Campargue, L. Biennier, A. Kachanov, R. Jost, B. Bussery-Honvault, V. Veyret, S. Churrassy and R. Bacis, 'Rotationally resolved absorption spectrum of the O₂ dimer in the visible range'. *Chem. Phys. Lett.* **288**, 734-742 (1998), DOI: '10.1016/S0009-2614(98)00294-2'. Cited on page 49.
- [104] K. Pfeilsticker, F. Erle and U. Platt, 'Absorption of solar radiation by atmospheric O₄'. *J. Atmos. Sci.* **54**, 933-939 (1997). Cited on page 49.

- [105] S. Solomon, R. W. Portmann, R. W. Sanders and J. S. Daniel, 'Absorption of solar radiation by water vapor, oxygen and related collision pairs in the Earth's atmosphere'. *J. Geophys. Res.* **103**, 3847-3858 (1998), DOI: '10.1029/97JD03285'. Cited on page 49.
- [106] F. Erle, K. Pfeilsticker and U. Platt, 'On the influence of tropospheric clouds on zenith-scattered-light measurements of stratospheric species'. *Geophys. Res. Lett.* **22**, 2725-2728 (1995), DOI: '10.1029/95GL02789'. Cited on page 49.
- [107] A. Maurellis, R. Lang, W. van der Zande, I. Aben and W. Ubachs, 'Precipitable water column retrieval from GOME data'. *Geophys. Res. Lett.* **27**, 903-906 (2000), DOI: '10.1029/1999GL010897'. Cited on page 50.
- [108] V. I. Dianov-Klokov, 'Absorption spectrum of oxygen at pressures from 2 to 35 atm. in the region 12 600 to 3600 Å'. *Opt. Spectrosc.* **16**, 224-227 (1964). Cited on page 50.
- [109] A. Watanabe and H. L. Welsh, 'Pressure-Induced infrared absorption of gaseous hydrogen and deuterium at low temperatures II. Analysis of the band profiles for hydrogen'. *Can. J. Phys.* **45**, 2859-2871 (1967). Cited on pages 52 and 64.
- [110] R. P. Blickensderfer and G. E. Ewing, 'Collision-induced absorption spectrum of gaseous oxygen at low temperatures and pressures. I. The $^1\Delta_g \leftarrow ^3\Sigma_g^+$ System'. *J. Chem. Phys.* **51**, 873-883 (1969), DOI: '10.1063/1.1672151'. Cited on pages 52 and 64.
- [111] D. R. Lide *et al.* (editors), *CRC Handbook of chemistry and physics*, 81st edition, CRC Press (2000), ISBN 0849304814. Cited on pages 59 and 60.
- [112] G. A. F. Seber and C. J. Wild, *Nonlinear regression*, John Wiley & Sons (1989), ISBN 0471617601. Cited on page 64.
- [113] A. A. Vigasin, 'On the temperature variations of the integrated absorption intensity in the oxygen fundamental'. *J. Mol. Spectrosc.* **224**, 185-187 (2004), DOI: '10.1016/j.jms.2004.02.003'. Cited on page 67.
- [114] R. Engeln, E. van den Berg, G. Meijer, L. Lin, G. M. H. Knippels and A. F. G. van der Meer, 'Cavity ring down spectroscopy with a free-electron laser'. *Chem. Phys. Lett.* **269**, 293-297 (1997), DOI: '10.1016/S0009-2614(97)00292-3'. Cited on page 71.
- [115] P. Zalicki, Y. Ma, R. N. Zare, E. H. Wahl, J. R. Dadamio, T. G. Owano and C. H. Kruger, 'Methyl radical measurement by cavity ring-down spectroscopy'. *Chem. Phys. Lett.* **234**, 269-274 (1995), DOI: '10.1016/0009-2614(95)00046-7'. Cited on page 71.
- [116] M. Ogawa, 'Absorption cross sections of O₂ and CO₂ continua in the Schumann and Far-UV regions'. *J. Chem. Phys.* **54**, 2550-2556 (1971), DOI: '10.1063/1.1675211'. Cited on pages 73 and 74.
- [117] B. R. Lewis, S. T. Gibson and P. M. Dooley, 'Fine-structure dependence of predissociation linewidth in the Schumann-Runge bands of molecular oxygen'. *J. Chem. Phys.* **100**, 7012-7035 (1994), DOI: '10.1063/1.466902'. Cited on page 74.
- [118] R. A. Toth, 'Water vapor measurements between 590 and 2582 cm⁻¹: line positions and strengths'. *J. Mol. Spectrosc.* **190**, 379-396 (1998), DOI: '10.

- 1006/jmsp.1998.7611'. Cited on page 77.
- [119] R. A. Toth, 'Transition frequencies and absolute strengths of H₂¹⁷O and H₂¹⁸O in the 6.2 μm region'. *J. Opt. Soc. Am. B* **9**, 462–482 (1992). Cited on page 77.
- [120] R. A. Toth, '2ν₂-ν₂ and 2ν₂ bands of H₂¹⁶O, H₂¹⁷O, and H₂¹⁸O: line positions and strengths'. *J. Opt. Soc. Am. B* **10**, 1526–1544 (1993). Cited on page 77.
- [121] R. A. Toth, 'The ν₁ and ν₃ Bands of H₂¹⁷O and H₂¹⁸O: line positions and strengths'. *J. Mol. Spectrosc.* **166**, 184–203 (1994), DOI: '10.1006/jmsp.1994.1184'. Cited on page 77.
- [122] R. A. Toth, 'Transition frequencies and strengths of H₂¹⁷O and H₂¹⁸O: 6600 to 7640 cm⁻¹'. *Appl. Opt.* **33**, 4868–4879 (1994). Cited on page 77.
- [123] J. P. Chevillard, J.-Y. Mandin, J.-M. Flaud and C. Camy-Peyret, 'H₂¹⁸O: The (030), (110), and (011) interacting states. Line positions and intensities for the 3ν₂, ν₁ + ν₂, and ν₂ + ν₃ bands'. *Can. J. Phys.* **63**, 1112–1127 (1985). Cited on page 77.
- [124] J. P. Chevillard, J.-Y. Mandin, C. Camy-Peyret and J.-M. Flaud, 'The first hexad {(040), (120), (021), (200), (101), (002)} of H₂¹⁸O: experimental energy-levels and line intensities'. *Can. J. Phys.* **64**, 746–761 (1986). Cited on page 77.
- [125] J. P. Chevillard, J.-Y. Mandin, J.-M. Flaud and C. Camy-Peyret, 'H₂¹⁸O: line positions and intensities between 9500 and 11 500 cm⁻¹. The (041), (220), (121), (300), (201), (102), and (003) interacting states'. *Can. J. Phys.* **65**, 777–789 (1987). Cited on page 77.
- [126] A. Bykov, O. Naumenko, T. Petrova, A. Scherbakov, L. Sinitsa, J. Y. Mandin, C. Camy-Peyret and J.-M. Flaud, 'The second decade of H₂¹⁸O: line positions and energy levels'. *J. Mol. Spectrosc.* **172**, 243–253 (1995), DOI: '10.1006/jmsp.1995.1172'. Cited on page 77.
- [127] M. Tanaka, J. W. Brault and J. Tennyson, 'Absorption spectrum of H₂¹⁸O in the range 12 400–14 520 cm⁻¹'. *J. Mol. Spectrosc.* **216**, 77–80 (2002), DOI: '10.1006/jmsp.2002.8670'. Cited on pages 77, 81 and 84.
- [128] C. Camy-Peyret, J.-M. Flaud, J.-Y. Mandin, A. Bykov, O. Naumenko, L. Sinista and B. Voronin, 'Fourier-transform absorption spectrum of the H₂¹⁷O molecule in the 9711–11 335 cm⁻¹ spectral region: the first decade of resonating states'. *J. Quant. Spectrosc. Radiat. Transfer* **61**, 795–812 (1999), DOI: '10.1016/S0022-4073(98)00068-5'. Cited on page 77.
- [129] H. Naus, W. Ubachs, P. F. Levelt, O. L. Polyansky, N. F. Zobov and J. Tennyson, 'Cavity ring-down spectroscopy on water vapor in the range 555–604 nm'. *J. Mol. Spectrosc.* **205**, 117–121 (2001), DOI: '10.1006/jmsp.2000.8246'. Cited on pages 77, 79, 80 and 81.
- [130] M. Tanaka, M. Sneep, W. Ubachs and J. Tennyson, 'Cavity ring-down spectroscopy of H₂¹⁸O in the range 16 570–17 120 cm⁻¹'. *J. Mol. Spectrosc.* **226**, 1–6 (2004), DOI: '10.1016/j.jms.2004.03.004'. Cited on pages 78 and 81.
- [131] J. Tennyson, M. A. Kostin, P. Barletta, G. J. H. J. Ramanlal, O. L. Polyansky and N. F. Zobov, 'DVR3D: a program suite for the calculation of rotation-vibration spectra of triatomic molecules'. *Comp. Phys. Comm.* (in press). Cited on page 80.

- [132] S. V. Shirin, O. L. Polyansky, N. F. Zobov, P. Barletta and J. Tennyson, 'Spectroscopically determined potential energy surface of H₂¹⁶O up to 25 000 cm⁻¹'. *J. Chem. Phys.* **118**, 2124-2129 (2003), DOI: '10.1063/1.1532001'. Cited on page 80.
- [133] N. F. Zobov, D. Belmiloud, O. L. Polyansky, J. Tennyson, S. V. Shirin, M. Carleer, A. Jenouvrier, A.-C. Vandaele, P. F. Bernath, M. F. Merienne and R. Colin, 'The near ultraviolet rotation-vibration spectrum of water'. *J. Chem. Phys.* **113**, 1546-1552 (2000), DOI: '10.1063/1.481940'. Cited on page 81.
- [134] M. Tanaka, O. Naumenko, J. W. Brault and J. Tennyson, 'Fourier transform absorption spectrum of H₂¹⁷O in the range 11 335 - 14 520 cm⁻¹' (to be published). Cited on page 84.
- [135] T. Voigt and J. van Minnen (editors), *Impacts of Europe's changing climate*, European Environment Agency (2004), ISBN 92 9167 692 6, URI: 'http://reports.eea.eu.int/climate_report_2_2004/en/'. Cited on pages 99 and 103.

List of publications

M. Sneep and W. Ubachs, 'Cavity Ring-Down Measurements of the O₂-O₂ collision-induced absorption resonance at 477 nm at sub-atmospheric pressures'. *J. Quant. Spectrosc. Radiat. Transfer* **78** (1), 171-178 (2003).

DOI: '10.1016/S0022-4073(02)00190-5'.

This article is reproduced in chapter 5.

M. Sneep, S. Hannemann, E. J. van Duijn and W. Ubachs, 'Deep-ultraviolet cavity ringdown spectroscopy'. *Opt. Lett.* **29**, 1378-1380 (2004).

This article is reproduced in chapter 7.

M. Tanaka, M. Sneep, W. Ubachs and J. Tennyson, 'Cavity ring-down spectroscopy of H₂¹⁸O in the range 16 570-17 120 cm⁻¹'. *J. Mol. Spectr.* **226** (1), 1-6 (2004).

DOI: '10.1016/j.jms.2004.03.004'.

This article is reproduced in chapter 8.

M. Sneep and W. Ubachs, 'Direct measurement of the Rayleigh scattering cross section in various gases'. *Accepted for publication in J. Quant. Spectrosc. Radiat. Transfer*.

This article is a shortened version of chapter 3.

M. Sneep and W. Ubachs, 'Cavity ring-down spectroscopy of O₂-O₂ collisional induced absorption', in 'Weakly Interacting Molecular Pairs: Unconventional Absorbers of Radiation in the Atmosphere', (edited by C. Camy-Peyret and A. A. Vigasin), volume 27 of *NATO Science Series: IV. Earth and Environmental Sciences*, 203-211, Kluwer Academic Publishers, Dordrecht, Boston, London (2003), ISBN 1 4020 1596 8, proceedings of the NATO Advanced Research Workshop, Fontevraud, France, April 29 - May 3, 2002.

Parts of this contribution were used in the chapter 2.

Publications not reproduced here

M. Sneep, M. Tanaka, W. Ubachs and J. Tennyson, 'Cavity ring-down spectroscopy of H₂¹⁷O in the energy range 16 570 - 17 125 cm⁻¹'. *To be published*.

N. Divinis, T. D. Karapantsios, M. Kostoglou, C. S. Panoutsos, V. Bontozoglou, A. C. Michels, M. C. Sneep, R. De Bruijn and H. Lotz, 'Bubbles growing in supersaturated solutions at reduced gravity'. *AIChE J.* **50** (10), 2369-2382 (2004).

List of publications

Other contributions

G. Moortgat, R. Lang, H. Nüss and M. Sneeep, 'Important photochemical processes in the lower atmosphere', pages 60–72 *in* 'Chemical, physical and biogenic processes in the Atmosphere', (edited by G. Moortgat and B. van Scheeren), lecture notes for the third international research school for cooperation on oceanic, atmospheric and climate change studies (COACH), March 5 to 16, 2001, Obernai, France.

J. Vilà-Guerau de Arellano, J. Trentmann, D. Olivie and M. Sneeep, 'Atmospheric boundary layer processes and chemistry', pages 253–261 *in* 'Chemical, physical and biogenic processes in the Atmosphere', (edited by G. Moortgat and B. van Scheeren), lecture notes for the third international research school for cooperation on oceanic, atmospheric and climate change studies (COACH), March 5 to 16, 2001, Obernai, France. Distributed by the Max-Planck-Institut für Chemie (Otto-Hahn-Institut), Atmospheric Chemistry department, Postfach 30 60, 55020 Mainz, Germany (2002).

Samenvatting van “De atmosfeer in het laboratorium: cavity ring-down metingen aan verstrooiing en absorptie”

In dit proefschrift worden absorptiespectroscopie metingen aan atmosferische gassen beschreven. In deze samenvatting wil ik proberen een overzicht te geven van de natuurkunde die in dit proefschrift gebruikt wordt, en wel op een manier die voor geïnteresseerde leken te volgen is. Hiervoor is het noodzakelijk eerst op enkele achtergronden in te gaan.

Uit verschillende waarnemingen blijkt dat het klimaat op aarde aan het veranderen is. Een recent rapport van het Europees milieuoagentschap “Impacts of Europe’s changing climate” (zie referentie 135) laat enkele gevolgen voor Europa zien: droogte en woestijnvorming in Zuid-Europa, overvloedige neerslag in Noord- en Oost-Europa en het verdwijnen van gletsjers in berggebieden. De gevolgen van deze veranderingen voor de fauna zijn nog onduidelijk, maar overstromingen en gevolgen voor de oogsten kunnen verwacht worden, terwijl de diversiteit van de flora al afgenomen is. Uit waarnemingen is eveneens gebleken dat de dikte van de ozonlaag in de atmosfeer vanaf begin jaren tachtig snel afneemt. Voor de ozonlaag is het duidelijk dat de oorzaak van deze verandering gezocht moet worden in menselijk handelen; internationaal politiek optreden heeft verdere productie van de schadelijke stoffen gestopt, al zal een herstel zeker nog een eeuw op zich laten wachten. De veranderingen in het klimaat lijken eveneens veroorzaakt te worden door menselijk handelen, al zijn nog niet alle wetenschappers overtuigd van een dergelijke harde conclusie; meer waarnemingen zijn noodzakelijk om *alle* oorzaken van de waargenomen veranderingen vast te leggen.

Om veranderingen in het klimaat te kunnen waarnemen, zijn metingen op mondiale schaal noodzakelijk. Satellieten zijn hiervoor zeer geschikt; de veranderingen van gletsjers kunnen rechtstreeks uit satellietopnamen bepaald worden. Ook voor het bepalen van de samenstelling van de atmosfeer zijn satellieten bij uitstek geschikt, niet alleen vanwege de mondiale dekking, maar ook omdat over de gehele *hoogte* van de atmosfeer waargenomen kan worden. Hiervoor wordt een spectrum van het zonlicht, dat weerkaatst is door de aarde, opgenomen door een satelliet. Dit licht heeft een grote afstand door de atmosfeer afgelegd, en de absorptieresonanties van de aanwezige gassen en dampen zijn in dit spectrum terug te vinden. Om uit dit waargenomen spectrum de concentratie en hoogteverdeling van bepaalde gassen in de atmosfeer – bijvoorbeeld de hoeveelheid ozon – te kunnen bepalen, moet bekend zijn *hoeveel* licht de verschillende gassen absorberen. De metingen in dit proefschrift vormen een bijdrage aan deze referentie-gegevens.

Alle gassen in de atmosfeer absorberen licht bij specifieke golflengten of kleuren. De golflengten waarbij een molecuul absorbeert – de resonanties – zijn karakteristiek voor het specifieke molecuul, en geven informatie over de interne structuur van de materie.

Naast absorptie zijn er nog andere manieren waarop licht en materie elkaar beïnvloeden: licht met een golflengte die niet samenvalt met een resonantie kan *verstrooid* worden. Bij verstrooiing wordt het licht niet geabsorbeerd, maar via een molecuul in een andere richting doorgestuurd; het molecuul zelf belandt niet in een aangeslagen toestand. Licht is een elektro-magnetische trilling, en de elektronen in een molecuul worden door een passerende golf in trilling gebracht, zoals een kleine boot aan het schommelen wordt gebracht als er een golf langskomt. Deze trillende elektronen gaan vervolgens zelf ook weer licht uitzenden en hierdoor wordt een gedeelte van het invallende licht verstrooid. Om de analogie met een boot voort te zetten: de schommelende boot veroorzaakt zelf ook weer golven. De mate waarin licht verstrooid wordt is afhankelijk van de golflengte van het licht: hoe korter de golflengte, des te efficiënter de verstrooiing.¹ Dit verklaart ook waarom we overdag een blauwe lucht kunnen zien: blauw licht heeft een kortere golflengte dan rood licht, en wordt daarom in grotere mate uit het pad van het licht verstrooid. Hierdoor is het blauwe licht in een zijwaartse richting veel beter zichtbaar dan langere golflengten. Hetzelfde principe is ook verantwoordelijk voor de rode gloed bij zonsondergang, zoals afgebeeld op de omslag. Door de lange weglengte door de atmosfeer, wordt het grootste deel van het blauwe licht uit de bundel verwijderd en blijft het rode deel van het spectrum over. Dit type verstrooiing staat bekend onder de naam 'Rayleigh verstrooiing', naar Lord Rayleigh (1842–1919), een zeer veelzijdig Brits wetenschapper.

Voor zichtbaar licht is de atmosfeer vrijwel volledig transparant; hieruit mag geconcludeerd worden dat de absorptie van zichtbaar licht door atmosferische moleculen gering is. Om deze absorpties desondanks te kunnen meten, is het gebruik van een gevoelige techniek noodzakelijk. Voor deze metingen is de zogenaamde 'cavity ring-down' absorptiespectroscopie techniek gebruikt. Een vertaling van deze term is lastig te geven, maar komt neer op 'leeglopende trilholte' techniek: een korte puls laserlicht wordt opgesloten tussen twee hoogreflecterende spiegels. Dit licht weerkaatst vele duizenden malen tussen de set spiegels, en bij iedere weerkaatsing wordt het grootste gedeelte van het licht weerkaatst naar de andere spiegel; bij de meeste van de metingen in dit proefschrift is die fractie meer dan 99,9%. Een kleine fractie van het licht lekt *door* de spiegels, waardoor de hoeveelheid opgesloten licht afneemt. Omdat de hoeveelheid opgesloten licht afneemt, neemt ook de hoeveelheid uitlekkend licht bij iedere reflectie af. Door de intensiteit van dit uitlekkende licht te meten als functie van de tijd, wordt een karakteristieke tijd voor het leeglopen verkregen. Met een afstand tussen de spiegels van ongeveer één meter en de bovengenoemde reflectiviteit is die karakteristieke tijd ongeveer $50 \mu\text{s}$,² wat overeenkomt met een afstand van ongeveer 15 km. Afhankelijk van de exacte reflectiviteit van de spiegels, kunnen afstanden tot ongeveer 100 km gehaald worden. Als er een gas in de ruimte tussen de spiegels wordt gelaten, dan wordt de karakteristieke leegloop tijd korter; een gedeelte van het licht wordt immers door het gas geabsorbeerd of verstrooid waardoor de hoeveelheid licht tussen de spiegels *sneller* afneemt in vergelijking met een lege trilholte. Uit deze afname van

¹ Hier loopt de analogie met een boot vast. ² 'μs' staat voor microseconde, een miljoenste van een seconde.

de karakteristieke leegloop tijd en de dichtheid van het gas tussen de spiegels kan de mate van absorptie, ook wel de werkzame doorsnede voor absorptie genoemd, bepaald worden. Door de grote afstand die het licht tussen de spiegels aflegt is de meetmethode zeer gevoelig, en kunnen zwakke absorpties gemeten worden. Een ander voordeel tegenover meer conventionele meettechnieken is het feit dat alle informatie uit het tijdsverloop van het signaal wordt verkregen; de meer conventionele technieken gebruiken de intensiteit van het licht nadat het een afstand door het gas heeft afgelegd en hierdoor kunnen gepulste lasers niet goed gebruikt worden, omdat grote verschillen in intensiteit tussen opeenvolgende pulsen de meting verstoren.

Voor de metingen in dit proefschrift is de 'cavity ring-down' techniek toegepast op verschillende gassen en in verschillende golflengtegebieden. In hoofdstuk 3 worden metingen aan Rayleigh verstrooiing van licht gepresenteerd. Het principe achter deze verstrooiing werd al in 1899 beschreven, maar pas recentelijk zijn voldoende gevoelige meettechnieken ontwikkeld om de mate waarin licht door een gas verstrooid wordt ook kwantitatief te meten. Door de metingen te vergelijken met waarden voor de werkzame doorsnede voor verstrooiing berekend uit gemeten brekingsindices, kan de (klassieke) theorie van Lord Rayleigh geverifieerd worden. Beide resultaten stemmen goed overeen, mits een correctie voor de asymmetrie van de moleculen wordt toegepast. Deze correctie was in 1923 al door Louis King gevonden.

In hoofdstuk 8 wordt absorptiespectroscopie beschreven aan een isotopomeer van water: H_2^{18}O . Het meest voorkomende water is H_2^{16}O , water met een zuurstofatoom met massagetal 16. In H_2^{18}O is het zuurstofatoom vervangen door een zuurstofatoom met massagetal 18. Chemisch zijn beide soorten water identiek, maar de absorptiespectra zijn anders. Waterdamp komt in zeer grote hoeveelheden in de atmosfeer voor, en zelfs een relatief zeldzame isotoopvariant komt nog zoveel voor dat kennis van het absorptiespectrum van belang is voor de analyse van satellietmetingen. Bovendien vormt het spectrum van een isotopomeer een referentie voor berekeningen aan de spectra; via deze metingen kan de theorie waarmee het waterspectrum van alle isotopomeren wordt uitgerekend verder verfijnd worden. Naast de gevoeligheid van de meettechniek is het hier van belang dat de opstelling een klein volume heeft omdat isotoopverrijkt water kostbaar is.

In hoofdstuk 7 is een nieuw ontworpen lasersysteem gebruikt om licht te produceren bij extreem korte golflengtes, ver in het ultraviolette gedeelte van het spectrum. Met behulp van deze opstelling is gedemonstreerd dat het mogelijk is om 'cavity ring-down' metingen te verrichten bij golflengtes van 197 nm ,³ tot nu toe de kortste golflengte waarbij metingen met deze techniek zijn verricht. Bij deze golflengtes absorberen de meeste gassen; de demonstratiemetingen zijn verricht aan het verzwakken van de intensiteit van licht als het zich voortplant (de extinctie) in zwavelhexafluoride, kooldioxide en zuurstof. Tevens zijn metingen verricht aan het absorptiespectrum van zuurstof in dit golflengtegebied, de zogenaamd

³ 'nm' staat voor nanometer, een miljardste meter, een eenheid om golflengten aan te geven. Zichtbaar licht heeft een golflengte van 400 nm (diepblauw) tot 700 nm (dieprood).

Schumann–Runge banden. Deze metingen zijn van belang omdat de sterkte van de Schumann–Runge banden en het onderliggende Herzberg continuüm bepalen hoe diep licht met een golflengte van ongeveer 200 nm doordringt in de atmosfeer.

De hoofdstukken 5 en 6 behandelen een laatste klasse van absorpties die door botsingen tussen moleculen mogelijk gemaakt worden, in dit geval in zuurstof. Zuurstof is een bijzonder molecuul. Het heeft een groot aantal mogelijkheden om licht te absorberen bij relatief lange golflengten, maar vanwege de symmetrie-eigenschappen van zuurstof zijn deze absorptieresonanties sterk onderdrukt. Tijdens een botsing van twee zuurstofmoleculen worden de symmetrie-eigenschappen verbroken, en kan een dergelijke overgang wel plaatsvinden. Dit is op zichzelf nog niet zo bijzonder – dergelijke door botsingen versterkte absorpties komen bij meerdere moleculen voor. Wat zuurstof zo bijzonder maakt is dat gedurende een botsing de twee moleculen gezamenlijk een *enkel* foton absorberen, en *beiden* in een aangeslagen toestand de botsing verlaten. Deze combinatie zorgt ervoor dat de botsingsgeïnduceerde absorpties bij golflengtes plaatsvinden waar een enkel zuurstof-molecuul niet absorbeert.

De botsingsgeïnduceerde resonantie in zuurstof bij 477 nm is belangrijk voor het recentelijk gelanceerde OMI (Ozone Monitoring Instrument) instrument. Om de hoeveelheid ozon goed te kunnen bepalen, is het bij de analyse van de spectra van belang te weten of er wolken aanwezig waren, omdat deze de optische eigenschappen van de atmosfeer sterk beïnvloeden. Als er wolken aanwezig zijn, weerkaatsen die het zonlicht op een grotere hoogte dan normaal het geval zou zijn; hierdoor neemt de afstand die het licht door de atmosfeer aflegt af en dit beïnvloedt de spectra. De botsingsgeïnduceerde absorptie door zuurstof wordt als liniaal gebruikt om de effectieve weglengte van het licht door de atmosfeer te bepalen: zuurstof is immers in een concentratie van 20% aanwezig, en deze concentratie is nauwelijks aan verandering onderhevig. Omdat de temperatuur in de atmosfeer afhangt van de hoogte, zijn ook metingen bij een lagere temperatuur verricht, om effecten van de temperatuur op deze botsingsgeïnduceerde absorpties te bepalen.

Summary

In this thesis absorption spectroscopy measurements on atmospheric gases are presented. To place these measurements in a wider context, it is helpful to start with some background.

A multitude of observations have shown that the earth's climate is changing. A recent report from the European Environment Agency "Impacts of Europe's changing climate" (see reference 135) lists some of the consequences in Europe: a decrease in precipitation and desertification in the south of Europe, an increase in precipitation in north- and east-Europe and retreating glaciers in the mountain ranges. The effects on animal life are not entirely clear, but flooding and changes in crop yields are to be expected, while the diversity of plant life has already been reduced. Observations also showed a rapid decrease in the thickness of the ozone layer starting from the early nineteen-eighties. This decrease was clearly caused by anthropogenic emissions; international political agreement led to a ban on the production of the harmful chemicals, but recovery will take at least another century. The climate changes also seem to be caused by anthropogenic emissions, although not all scientists are convinced this can be concluded from the data gathered so far; further measurements are needed to fully determine the causes for the observed changes.

In order to detect changes in the climate, observations on a global scale are needed. Satellites can perform these measurements; changes in glaciers can be readily detected on satellite images. They are also highly suitable for the detection of changes in the atmosphere, not only because of the global coverage, but also because the observation extends over the entire *height* of the atmosphere. To detect the composition of the atmosphere from an orbiting instrument, a spectrum of reflected sunlight is recorded. This light has travelled a significant distance through the earth's atmosphere, and the absorption resonances of the gases that are present in the atmosphere can be found in this spectrum. To determine the concentration of specific gases - for example ozone - from these observed spectra, one needs to know the *amount* of light that is absorbed by the various gases. The measurements in this thesis form a contribution to this set of reference-spectra.

The absorption resonances of a molecule are specific to a particular species, and allow for identification of the molecule. The spectrum itself tells us about the internal structure of the molecule.

Another interaction between light and matter is *scattering*. A resonance in the molecule is not needed for scattering, it occurs when light falls on a molecule and is emitted in a different direction. Light is an electro-magnetic wave, and this wave causes the electrons in a molecule to vibrate, much like a small boat rolls when a wave passes the boat on water. These vibrating electrons become broadcasters according to classical electrodynamics theory, and emit light, causing part of the incoming energy to be scattered. To continue the boat analogy: the rolling boat itself creates a smaller wave on the water. The intensity of the scattered radiation

depends on the wavelength of the incident radiation: shorter wavelengths are scattered more efficiently than longer wavelengths.¹ This also explains why we see a blue sky during the day: the wavelength of blue light is much shorter than that of red light, and is therefore a greater portion of it is scattered from the beam. It dominates all the light that comes from another direction than directly from the sun. The same mechanism is also responsible for the red glow at sunset – as shown on the cover: in the long path through the atmosphere the blue part of the spectrum is scattered out of the beam, leaving only the red part of the spectrum. This type of scattering is known as ‘Rayleigh scattering’, after Lord Rayleigh (1842–1919).

For visible light, the atmosphere is nearly completely transparent: this leads to the conclusion that the absorption-resonances in atmospheric molecules are weak. To detect these resonances despite their weakness, a sensitive measurement technique is required. For the measurements in this thesis, the ‘cavity ring-down’ absorption spectroscopy technique was used. In this technique, a short pulse of laser light is brought between two highly reflective mirrors. This light bounces back and forth between these mirrors several thousand times. At each reflection the largest fraction, typically more than 99.9%, bounces back to the other mirror. A small fraction of the light leaks *through* the mirrors, causing the amount of light enclosed between the mirrors to decrease. Because the enclosed amount of light decreases, the amount of light that leaks out also decreases. By measuring the intensity of this leak out as a function of time, a decay time of the cavity is obtained. With a distance between the mirrors of about one metre and the reflectivity mentioned above, the decay time is about 50 μs , equivalent to a distance of about 15 km. Depending on the exact reflectivity of the mirrors, distances of up to 100 km can be obtained. If a gas is put in the cell between the mirrors, the decay time is shortened; part of the light is absorbed or scattered by the gas, which causes the amount of light to decrease *faster* than if the gas would not have been there. From the decrease in the decay time and the density of the gas in the cell, the absorption cross section can be calculated. Because of the large distance the light travels between the mirrors, this method is very sensitive, and allows for the detection of very weak absorptions. Another advantage of this technique over more conventional absorption spectroscopic techniques is the fact that all information is obtained from the time-evolution of the signal; more conventional techniques use the intensity of the light after it has travelled through the gas. Pulsed lasers cannot easily be used in such techniques, because of the large intensity fluctuations between pulses in such lasers.

For the research in this thesis, the cavity ring-down technique is applied to various gasses in several wavelength ranges. In chapter 3 measurements on Rayleigh scattering of light are presented. The principle behind this type of scattering was published already in 1899, but only recently the measurement techniques have become sensitive enough to quantitatively measure the extinction of light due to scattering in a gas. These measurements can be compared to values for the scattering cross section calculated from measurements of the refractive index

¹ This is where I’ll have to stop using the boat analogy.

to verify the the (classical) theory from Lord Rayleigh. Both results are in close agreement, provided a correction for the asymmetry of the molecules is applied. This correction was already formulated in 1923 by Louis King.

In chapter 8 measurements on an isotopomer of water are shown. The most abundant water is H_2^{16}O , water based on an oxygen atom with mass 16. In these measurements the oxygen is replaced by a heavy variant, to form H_2^{18}O . Chemically both types of water are identical, but the absorption spectra differ. Water vapour is present in the atmosphere in large quantities, and even a relatively rare isotope variant is important for the analysis of satellite measurements. The measurements on an isotopomer also provide an extra reference for calculations on the absorption spectrum of water, not just for H_2^{18}O , but for all of them. In performing these measurement it is not only the sensitivity of the measurement technique that is important, the small cell volume is also plays an important role, because isotope enriched water is rather expensive.

In chapter 7 a newly designed laser system is used to produce light at extremely short wavelengths, far into the ultra-violet part of the spectrum. With this laser system cavity ring-down spectroscopy at wavelengths as short as 197 nm was demonstrated, the shortest wavelength at which cavity ring-down spectroscopy has been used so far. At these wavelengths most gases absorb; some demonstration measurements on the extinction in sulphur hexafluoride, carbon dioxide and oxygen. Further measurements were performed on the absorption spectrum of oxygen in this wavelength range, the so-called Schumann-Runge bands. These measurements are important because the strength of the Schumann-Runge bands and the Herzberg continuum, which lies underneath these bands, determine how far radiation with a wavelength of about 200 nm penetrates the atmosphere.

Chapters 5 and 6 deal with measurements on a final class of absorptions: collision-induced absorptions, in this case in oxygen. Oxygen has many low-lying electronically excited states, but transitions between these states are *all* symmetry forbidden, causing the absorption resonances to be extremely weak. During a collision the symmetry is broken, and the transition is allowed. The truly remarkable situation in oxygen is that the two molecules can absorb a single photon during the collision and that *both* molecules leave the collision in an excited state. These collision-induced absorptions occur in wavelength regions where a single oxygen molecule does not have absorption resonances.

The collision-induced absorption in oxygen near 477 nm is important for the recently launched OMI (Ozone Monitoring Instrument) instrument. In the analysis of the recorded satellite spectra, it is important to know the cloud coverage, as clouds change the path-length of the light through the atmosphere. The collision-induced absorption is used as a ruler to determine the effective path-length through the atmosphere: the atmosphere has 20% oxygen in it, and this value is constant. Because the temperature of the atmosphere changes with altitude, further measurements at low temperature were performed, to determine the effects of temperature on these collision-induced absorptions.

Colophon

The layout of this thesis was made in \LaTeX , the figures were created in MetaPost. The typeface is Lucida Bright, with Lucida Sans as the support font. The layout is created with the aid of the Memoir document-class, using packages (natbib, the NTG classes, hyperref, wrapfig, dcolumn, babel, fnpara) to customise certain parts of it.

The effort put into maintaining and supporting this software by a large group of volunteers is greatly appreciated. Special gratitude goes out to Gerben Wierda for compiling and maintaining \TeX on Mac OS X and Peter Wilson for creating Memoir and its manual.

The photograph on the cover was taken on april 24th, 2004. It shows the sunset as seen from Zandvoort aan Zee, the Netherlands. The nice colours are caused by Rayleigh scattering; the blue part of the spectrum is scattered out of the beam, leaving just the red light. Chapter 3 explains the (classical) theory of Rayleigh scattering in full detail.

Printed by PrintPartners Ipskamp B.V.

Licence Information

This work is licenced under the Creative Commons “Attribution, Share Alike” Licence. To view a copy of this licence, visit <http://creativecommons.org/licenses/by-sa/1.0/nl/> or send a letter to Creative Commons, 559 Nathan Abbott Way, Stanford, California 94305, USA.

